UNIVERSITY OF THE
WITWATERSRAND,
JOHANNESBURG

Carbon nanotubes application for lithium-ion battery anodes

by

Nqobile Mhlanga

Submitted to

A dissertation submitted to the Faculty of Engineering and the Built Environment, University of the Witwatersrand, Johannesburg, in fulfilment of the requirements for the degree in Master of Science in Engineering

Supervisor: Professor Vusumuzi Sibanda
Co-Supervisor: Dr Mpfunzeni Raphulu

Johannesburg, May 2024

DECLARATION

I, Nqobile Mhlanga, thus attest that I worked alone on this dissertation. It is being submitted to the University of the Witwatersrand for the Master of Science in Engineering degree. It was not previously submitted to any other university for a degree or exam.

SIGNATURE:  DATE:27 May 2024

DEDICATION

To my greatest teachers in life, my children

Letsatsi and Manqoba

ACKNOWLEDGEMENTS

I want to express my gratitude to my Lord and Savior Jesus Christ, who made this all possible. I will forever be grateful to Mintek for funding me for every bit of this study. The journey walked in this study would not have been possible without the selfless efforts and contributions of the following people:

- My family has been there for me through prayer and encouragement throughout this journey. An exclusive appreciation goes to my children, for their sacrifices during this challenging period.
- My supervisors Professor Vusumuzi Sibanda and Dr Mpfunzeni Raphulu, for trusting me with this subject and their invaluable guidance throughout the entire research process.
- Dr Elmar Muller, my manager at Mintek, for his understanding, and support and for making sure that all required paperwork concerning this study is attended to timeously.
- Mr Ruphat Morena and Ms Romola Issari from Metrohm for allowing me to use their potentiostat for the electrochemical test work of this study.
- Dr James Aluha for all the unplanned crash courses he gave me at any time I came to his office with a question.
- Mr Paul den Hoed for all the interesting technical and non-technical discussions we had every time we met.
- Dr Gebhu Ndlovu for his advice throughout this journey.
- All my Mintek colleagues who contributed to this study.

RESEARCH OUTPUTS

Publications

1. B. Xakalashe, E. Muller, X. Goso, S. Nkosi, S. Tsebe, U. Hall, E. Matinde, S.Mokoena, R. Hassanalizadeh, P. Doubra, F. Jantjies, **N. Mhlanga**, C. Mokwana, M. Raphulu, M. Gericke and R.F. Sandenberg. *Batterry materials research conducted at Mintek towards energy storage and resource efficiency*. SAIMM Battery Materials Conference (2022) 105-118.
2. *Multi-walled carbon nanotubes synthesis and characterisation for lithium-ion batteries* (In preparation).

Conferences

1. **N. Mhlanga**, M. Raphulu, T. Khumalo and V. Sibanda. *Synthesis and characterisation of multi-walled carbon nanotubes for lithium-ion batteries*. Chem4Energy Annual Conference, South Africa 20- 24 March 2024.
2. **N. Mhlanga**, M. Raphulu, and V. Sibanda. *Multi-walled carbon nanotubes synthesis and characterisation for lithium-ion batteries*. African Sustainable Energy Solutions Symposium 2024, South Africa 25- 28 August 2024 (to submit a poster).

ABSTRACT

The most commonly used anode material for lithium-ion batteries (LIBs) is graphite, however it has some shortcomings such as having a low reversible capacity and low diffusion rate which produce low-power density batteries. Thus, the purpose of this study was to examine the application of carbon nanotubes (CNTs) as an alternative LIB anode material.

A bimetallic iron-cobalt catalyst supported on calcium carbonate (Fe-Co/$CaCO_{3)}$ was used for the synthesis of CNTs and it was prepared using the wet impregnation method. X-ray diffraction (XRD) analysis of the catalyst showed that it was highly crystalline. The specific surface area (SSA) which was determined using Brunauer-Emmett-Teller (BET) was found to be 11.3 m^2/g. CNTs were prepared using the chemical vapour deposition (CVD) method at various test parameters i.e. temperature (650°C,700°C,750°C and 800°C), hydrocarbon flow rate (90 mL/min and 120 mL/min) and carbon source (acetylene and ethylene). High-resolution transmission electron microscopy (HRTEM) results for samples synthesised at 650°C and 700°C using acetylene at a flow rate of 90 mL/min (650°C-A90 and 700°C-A90) showed that CNTs which were multiwalled carbon nanotubes (MWCNTs) in nature were produced. The formation of what appeared to be non-tubular carbon and carbon nanofibers was observed when the synthesis temperature was increased from 700°C to 800°C. The average outer diameter (OD) of the tubes ranged from 20 to 89 nm. At a higher acetylene flowrate (120 mL/min), the quality of CNTs seemed to deteriorate for synthesis temperatures above 650°C. The formation of non-tubular carbon-like nanofibers was observed at synthesis temperatures above 650°C. The average OD of the tubes ranged from 22 to 81 nm. XRD analysis of all samples synthesised using acetylene showed a similar pattern with the most intense peak being that of carbon and minor peaks being of iron. The samples also contained some broad peaks which suggested that the samples contained amorphous carbon. The calculated crystallite size ranged from 3.4 to 6.4 nm for samples synthesised using acetylene at a flowrate of 90 mL/min. For samples synthesised using acetylene at a flowrate of 120 mL/min, the crystallite size ranged from 3.1 to 4.4 nm. Raman spectroscopy confirmed the successful synthesis of MWCNTs; however, the intensity ratio (I_D/I_G) was found to be above 0.7 for a majority of the samples which confirmed the presence of impurities in the samples. SSA studies revealed that an inversely proportional relationship existed between the SSA and the synthesis temperature.

HRTEM results for samples synthesised at 650°C and 700°C using ethylene at a flow rate of 90 mL/min (650°C-E90 and 700°C-E90) revealed that CNTs which were MWCNTs in nature were formed. As the synthesis temperature increased from 700°C to 800°C, the formation of what appeared to be non-tubular carbon and carbon nanofibers was observed. The average OD of the tubes ranged from 21 to 84 nm. At a higher ethylene flowrate (120 mL/min), the quality of CNTs seemed to deteriorate for synthesis temperatures above 700°C. The formation of non-tubular carbon-like nanofibers was observed at synthesis temperatures above 700°C. The average OD of the tubes ranged from 11 to 79 nm. XRD analysis of all samples synthesised using ethylene showed a similar pattern with the most intense peak being that of carbon and minor peaks being of iron. However, the depicted minor peaks were broad which suggested that the samples contained amorphous carbon. The calculated crystallite size ranged from 3.7 to 5.7 nm for samples synthesised using ethylene at a flowrate of 90 mL/min. For samples synthesised using ethylene at a flowrate of 120 mL/min, the crystallite size ranged from 3.6 to 6.5 nm. Raman spectroscopy confirmed the successful synthesis of MWCNTs. SSA studies revealed that the SSA decreased with an increase in the synthesis temperature.

Furthermore, to evaluate the electrochemical performance of the synthesised material, electrodes of selected samples were fabricated. Commercial graphite electrodes were also fabricated to compare the performance with the samples synthesised in this study. Cyclic voltammetry (CV) and electrochemical impedance spectroscopy (EIS) were used for the electrochemical measurements. The CV tests were conducted at scan rates of 5 mV/s and 10 mV/s, An increase in the CV curve area was observed as the scan rate was increased. The calculated specific capacity of the samples compared well with that of the electrode fabricated with commercial graphite which reported an average of ~197 mAh/g after four cycles at a scan rate of 5 mV/s. The average specific capacity of the electrode fabricated with CNTs sample synthesised at 650°C using ethylene at a flowrate of 120 mL/min (650°C-E120) reported the highest value of 214 mAh/g after four cycles at a scan rate of 5 mV/s. Overall the variation between the samples of the EIS data was marginal. These EIS results also compared well with that of the electrode fabricated with commercial graphite. The findings of this work suggest that MWCNT electrodes have a good application potential and with doping, they may provide better electrochemical performance than graphite as a viable anode material for LIBs.

TABLE OF CONTENTS

LIST OF FIGURES

LIST OF TABLES

LIST OF ABBREVIATIONS

BET	Brunauer-Emmett-Teller
CE	Counter Electrode
CNT	Carbon nanotubes
CPE	Constant Phase Element
CV	Cyclic Voltammetry
CVD	Chemical Vapor Deposition
DMC	Dimethyl Carbonate
EC	Ethylene Carbonate
EDS	Energy-Dispersive
EIS	Electrolytic Impedance Spectroscopy
FESEM	Field Emission Scanning Electron Microscopy
FWHM	Full Width Half Maximum
HRTEM	High-Resolution Transmission Electron Microscopy
LIB	Lithium-ion Battery
MWCNTs	Multi-walled Carbon Nanotubes
NMP	N-methyl-2-pyrrolidone
PVDF	Polyvinylidene Difluoride
RE	Reference Electrode
SPCE	Screen Printed Carbon Electrode
SSA	Specific Surface Area
SWCNTs	Singel Walled Carbon Nanotubes
WE	Working Electrode
XRD	X-ray Diffraction

CHAPTER 1

1. INTRODUCTION

The growing reliance on fossil fuels to generate energy raises atmospheric concentrations of carbon dioxide gas, which has a greenhouse effect and contributes significantly to global warming (Kim *et al.*, 2014). This rise in fossil fuel consumption amongst others is a result of the growth in the global economy which is accompanied by an increase in energy demand (B. Liu *et al.*, 2021). The negative effects of greenhouse gases have subsequently shifted the focus of attention to power produced by utilising green and sustainable energy sources, including wind, solar, and biofuels (B. Liu *et al.*, 2021). The availability of suitable technologies is necessary for the generation, transmission, storage, and conservation of renewable energy (Choubey *et al.*, 2016). Batteries have emerged as potential power sources for both stationary and mobile applications. Good batteries must have exceptional volumetric and gravimetric energy density, an extended cycle life and calendar life, and be sufficiently safe (Kim *et al.*, 2020). In this regard, rechargeable lithium-ion batteries (LIBs) are among the most promising battery storage technologies. Currently, around 37% of rechargeable batteries sold worldwide are LIBs, and demand for them is rising (Swain, 2017).

The primary attributes of LIBs are their long cycle life and high power density, high gravimetric and volumetric energy, and low self-discharge properties. In addition, for portable electrochemical energy storage, LIBs are the primary source hence lowering their cost and enhancing their functionality can significantly broaden their applications and make it possible for new energy-dependent technologies to be developed (Nitta *et al.*, 2015). However, more research is still being done to enhance the characteristics of LIBs, particularly concerning their capability, propensity to deteriorate with time and safety issues (Kim *et al.*, 2020)

A typical LIB has four components: anode, cathode, separator, and electrolyte as shown in Figure 1. The performance of LIBs is dependent on the battery's electrochemical properties, and these are mostly affected by the electrode materials. Electrode materials also determine the cost of preparing the LIBs (Lu *et al.*, 2021). The next generation of lithium battery storage requires the development of highly efficient electrodes. Graphite is the most often utilised anode material in LIBs. It however has its shortcomings such as having a low reversible capacity and low diffusion rate which leads

to low power density batteries. Therefore, there is a need for anode material improvement which may require the replacement of graphite anodes with materials with higher energy capacity, and power density coupled with good life cycle and lower safety risk (Kim *et al.*, 2020). In view of this, nano-sizing the anode materials could potentially improve these important properties hence, carbon nanotubes (CNTs) present an opportunity for anode material improvement that has great promise and a bright perspective (De Las Casas and Li, 2012) (Wu *et al.*, 2014)(Goriparti *et al.*, 2014).

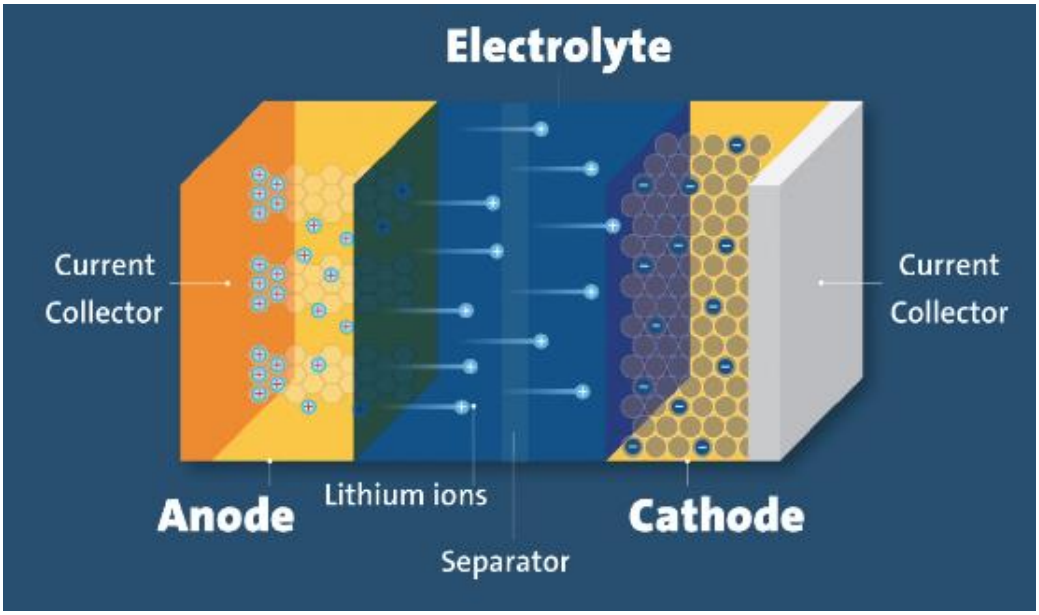

Figure 1: An illustration of the components of a LIB (UL Research Institutes, 2021)

Significant research efforts have recently been made to develop unique, high-capacity nano-architectures and extend the life of lithium-ion technology (De Las Casas and Li, 2012). Due to the unique properties and structures of CNTs, their application in lithium batteries could result in improved battery capacity compared to that obtained with graphite anodes. Therefore, the unique properties of CNTs make them ideal as a suitable constituent of a novel anode material for improved lithium storage. Hence this study focuses on the improvement of the performance of LIBs through the application of CNTs as anode materials and optimisation of the electrochemical performance to create an ideal energy storage technology.

1.1. Problem statement

The lack of adequate electricity generation and infrastructure particularly in South Africa and an increasingly louder global call to transition to green energy makes the development and implementation of renewable energy storage technology necessary. In terms of emerging technologies, LIBs are thought to be the most promising energy storage technology. Nonetheless, enhancing the anode materials' cycle life and capacity remains a major design challenge for LIBs (Xiong *et al.*, 2013). Graphite has historically been a widely utilised anode material; however, its shortcomings make LIBs not to be able to fulfil the stringent requirements for rate capability, cycling stability, and safety.

1.2. Research objectives

The main objective of this study is to investigate the application of CNTs as anode material for LIBs and their performance against standard LIB anode materials. The following specific objectives needed to be accomplished to do this:

a) Synthesising of CNTs at different parameters such as temperature, hydrocarbon flow rate and carbon source.
b) Fabrication of the CNT-Li anode using the synthesised CNTs.
c) Determination of the electrochemical capability of the synthesised CNTs using the cyclic voltammetry (CV) and electrochemical impedance spectroscopy (EIS) methods.

1.3. Hypothesis

The structure and morphologies of CNTs, when used as anode materials for LIBs, influence the electrochemical performance of LIBs.

1.4. Research approach

The study was divided into three parts. The first part involved the use of the chemical vapor deposition (CVD) method for the synthesis of CNTs at various parameters. The second part involved the characterisation of the CNTs specimens produced. The characterisation used included the following methods:

- High-resolution transmission electron microscopy (HRTEM)
- Field emission scanning electron microscopy (FESEM)
- X-ray diffraction (XRD)
- Raman spectroscopy and

- Brunauer-Emmett-Teller (BET)

The last part of the study involved electrode fabrication and electrochemical testing of selected carbon nanomaterial specimens produced.

1.5. Structure of dissertation

This dissertation is divided into 5 sections. A brief description of each chapter is given below:

- **Chapter 1 (Introduction):** This section outlines the background of the study and the main objectives of the whole research. It further gives an outline of the whole dissertation.

- **Chapter 2 (Literature review):** This section begins by giving a background on LIBs in which the working principle of LIBs, market size, and LIBs applications are discussed. The chapter further gives a review of carbon nanotubes and briefly discusses their properties, synthesis methods, and purification methods. The chapter concludes by discussing the electrochemical principles where cyclic voltammetry and electrochemical impedance spectroscopy are described.

- **Chapter 3 (Experimental procedures):** This section narrates the experimental procedures followed for this study. The chapter includes the catalyst preparation, CNTs synthesis, and characterisation, CNT/Li electrode fabrication, and the electrochemical testing of the electrodes fabricated with CNTs.

- **Chapter 4 (Results and discussion):** This chapter shows and discusses the results of the test work conducted in this study.

- **Chapter 5 (Conclusions and recommendations):** presents conclusions and recommendations from this study.

CHAPTER 2

2. LITERATURE REVIEW

This chapter begins by giving a brief background on LIBs. It further covers the market size of LIBs which also includes its applications. A brief background on CNTs including the most commonly used synthesis methods and the purification methods is reported. This chapter concludes by describing the fabrication process used for commercial LIBs as well as the two electrochemical characterisation methods (CV and EIS) that will be used for this study.

2.1. Lithium-ion batteries background

2.1.1. Working principle of LIBs

A battery is a device that converts chemical energy into electric energy using an electrochemical oxidation-reduction (redox) mechanism (Roselin *et al.*, 2019). A "cell" is the fundamental electrochemical unit that produces such an energy change. A battery is made up of a collection of a number of linked cells. Each cell contains four basic components: an anode (negative electrode), a cathode (positive electrode), an electrolyte and a separator. Cathodes and anodes are the charge carriers that aid in the storage and release of energy. The separator physically separates the electrodes to prevent internal short circuits while enabling Li^+ passage. Li^+ and other ions are carried by the electrolyte. Common cathode materials include lithium cobalt oxide, lithium manganese oxide, lithium nickel cobalt manganese oxide, and lithium iron phosphate. (Vinayak *et al.*, 2023). The most used anode material is graphite. Commercially, carbonate electrolytes based on $LiPF_6$ are used in LIBs (Vinayak *et al.*, 2023).

A typical working principle of a LIB is illustrated in Figure 2. Li^+ ions deintercalate from the cathode layer and migrate through an electrolyte and a separator to the anode during charging, where they intercalate between the layers of the graphite (Xiong *et al.*, 2013). Discharging involves the opposite procedure, and the linked system is powered by the transfer of electrons through the external circuit. As an example, the following reactions occur during the charging of a $LiCoO_2$/graphite cell: (Vinayak *et al.*, 2023):

Cathode: $LiCoO_2 \leftrightharpoons CoO_2 + Li^+ + e^-$ (2.1)

Anode: $C_6 + Li^+ + e^- \leftrightharpoons LiC_6$ (2.2)

Overall reaction: $LiCoO_2 + C_6 \leftrightharpoons LiC_6 + CoO_2$ (2.3)

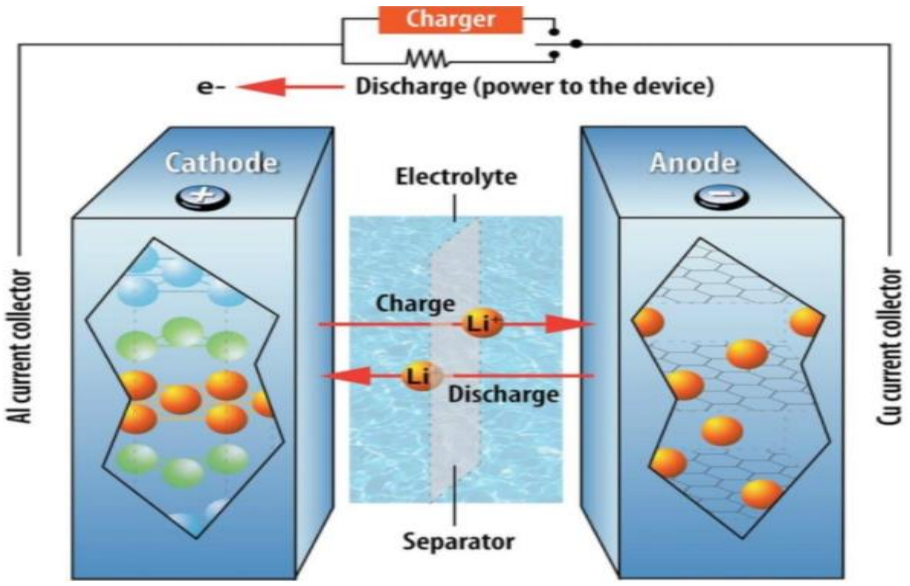

Figure 2: An illustration of the working principle of a LIB (Osiak *et al.*, 2014)

2.1.2. LIBs market size

The need to combat climate change through a more comprehensive energy transition that includes the use of electric vehicles is driving an increase in battery demand worldwide. A forecast by McKinsey showed that over the next ten years, the demand for LIBs is anticipated to skyrocket, with the required amount of GWh rising from about 700 GWh in 2022 to approximately 4.7 TWh by 2030 (see Figure 3) (Fleischmann *et al.*, 2023). The forecast further revealed that the majority of demand in 2030 will be met by batteries for use in mobility applications, like electric vehicles (EVs) roughly requiring 4,300 GWh (Fleischmann *et al.*, 2023).

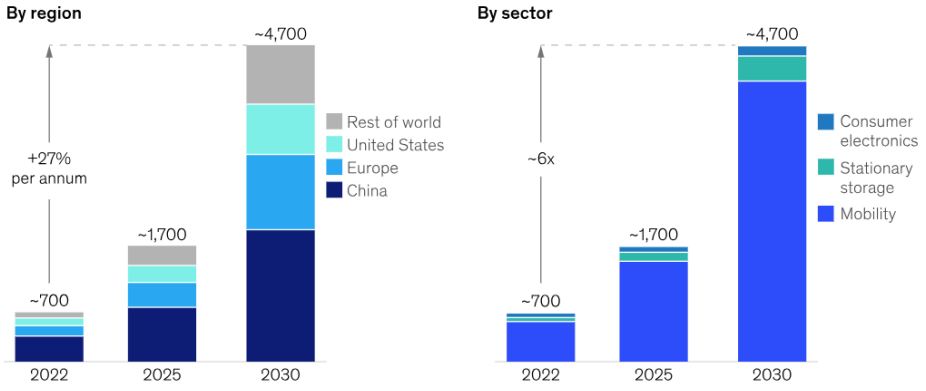

Figure 3: Global LIB cell demand, GWh, Base case (Fleischmann et al., 2023)

Furthermore, a forecast by Sphere Insights showed that by 2030 the market for LIBs is anticipated to reach USD 273.8 billion (Figure 4), growing at a CAGR of 19.3% from 2021 to 2030 (*Lightweight Materials Market Size, Share | Forecast 2030*, no date). The article also cited the growth of nuclear power plants and solar installations which is happening at the back of results of a greater understanding of the value of environmental preservation. Wind energy projects are also fostering the rapid development of LIBs for energy storage. Additionally, the market is also growing as a result of the growing use of lithium-ion battery systems in the medical sector (*Lightweight Materials Market Size, Share | Forecast 2030*, no date).

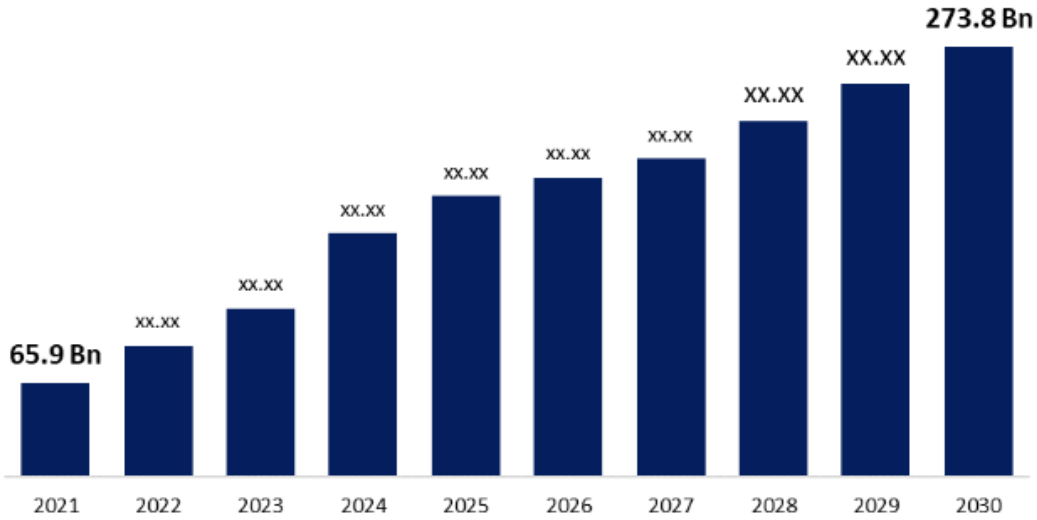

Figure 4: Global LIB market (Lightweight Materials Market Size, Share | Forecast 2030, no date)

2.1.3. LIBs applications

Currently Lithium is the most in-demand material for modern living and a crucial component of the modern electric vehicle revolution. The properties which make lithium a high sort after commodity include its high redox potential, electrochemical activity and that it has the highest specific heat capacity of any solid element (Goriparti *et al.*, 2014). Primary LIBs are frequently employed to power high-end devices because of their advantageous properties, although secondary LIBs predominate in the cellular phone and laptop computer markets. These consumer goods are rapidly increasing in number. Currently, lithium and LIBs account for around 37% of the global market for rechargeable batteries, and their use continues to grow (Swain, 2017). Figure 5 shows the estimated global end-user market size of Li for various sectors. The US Geological Survey revealed that LIBs were the highest Li consumers (U.S. Geological Survey, 2018).

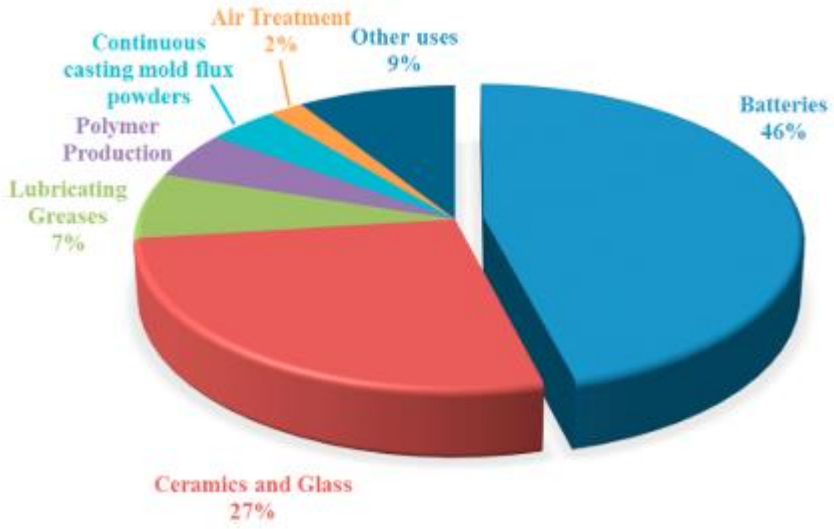

Figure 5: Global lithium end-use market share (U.S. Geological Survey, 2018)

2.2. Carbon nanotubes

2.2.1. Structure and properties

Allotropes of carbon include CNTs. CNTs are also known as tubular fullerenes (Lim and Lin, 2011). They are carbon structures with cylindrical shapes that are well structured (Carrara, 2010). In other terms, they resemble graphenes that have been folded into sheets with one or more layers as shown in Figure 6. Most of the different physical characteristics of CNTs come from the foundation material (graphene) (Jagadeesan *et al.*, 2020). Such graphene is made of carbon atoms densely packed in a regular sp^2 pattern and bound to an atomic size structure based on a honeycomb (Jagadeesan *et al.*, 2020).

Based on their arrangement, degree of graphitization, and structure, CNTs are categorized in several ways (Roselin *et al.*, 2019). They can either be classified as graphitic or amorphous depending on the graphitization degree (Roselin *et al.*, 2019). They can further be classified into two types i.e. single-walled CNTs (SWCNTs) and multi-walled CNTs (MWCNTs) depending on their physical structure. While their diameters are on the nanoscale, their lengths are on the microscale (Carrara, 2010). CNTs can be considered as 1D structures because of their large aspect ratio.

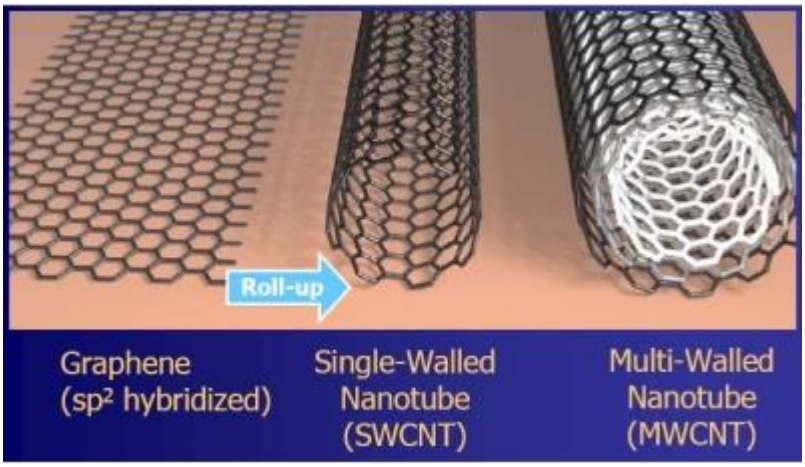

Figure 6: Schematic model describing SWCNT and MWCNT obtained from single graphene sheets (Carrara, 2010)

Armchair, zigzag, and chiral crystallographic configurations are the three categories used to categorize SWCNTs based on their configuration. (Shah and Tali, 2016) (Roselin *et al.*, 2019). This orientation depends on how the graphene sheet is wrapped and hence the final nanotube can be represented as a vector. Figure 7 shows the three classes of SWCNTs. Carbon-carbon bonds are perpendicular to the axis in the armchair conformation. Two opposite carbon-carbon bonds from each hexagon are parallel to the tube axis in the zigzag conformation and all other configurations, the opposing carbon-carbon bonds are at an angle to the tube axis, resulting in a chiral nanotube (Shah and Tali, 2016).

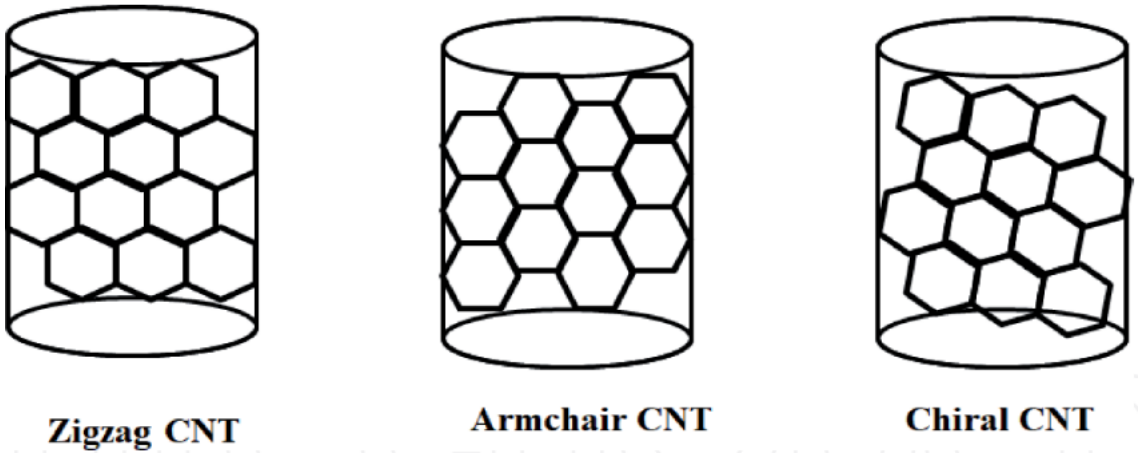

Figure 7: Types of SWCNTs structures (Jagadeesan *et al.*, 2020)

The properties of CNTs are highly based on their structure; for example, one-third of zigzag nanotubes and all armchair SWCNTs are metallic for typical dimensions; the remaining nanotubes

are semiconducting (Hamada *et al.*, 1992). Numerous electrode materials are low-conductive oxides (Wu *et al.*, 2014). The effectiveness of these electrode materials is largely dependent on the proper inclusion of chemicals that conduct carbon (Wu *et al.*, 2014).

CNTs have a large surface area relative to weight, outstanding mechanical, electrical, thermal, and optical properties (Shah and Tali, 2016)(Jagadeesan *et al.*, 2020). These properties point to CNTs as a unique option for enhancing the electrochemical characteristics of both anodes and cathodes (Wu *et al.*, 2014).

2.2.2. Synthesis methods of CNTs

There are three most commonly used methods for the production of CNTs namely: chemical vapor deposition, laser vaporization, and electric arc discharge (Jagadeesan *et al.*, 2020) (Wang *et al.*, 2019)(Lim and Lin, 2011). Among the three methods, for large-scale production, CVD is the most preferred method because of its lower cost and simple operation (Wang *et al.*, 2019).

Electric arc discharge

The electric arc discharge is the oldest method used for the production of CNTs (Szabó *et al.*, 2010). This method is also known as the plasma arcing method (Jagadeesan *et al.*, 2020). With this technique, a voltage of 20–25 V is delivered between pure graphite electrodes spaced 1 mm apart, and the quartz chamber's internal helium gas pressure is kept constant at 500 torr. (Jagadeesan *et al.*, 2020). Under these circumstances, an electric arc is created when the electrodes collide with one another. The arc's energy is transported to the anode, where it ionizes the carbon atoms in the anode's pure graphite to create C^+ ions and plasma. As the C^+ charged ions approach the cathode, they are reduced, deposited, and developed into CNTs. A schematic representation of the electric arc discharge method is shown in Figure 8. Despite producing high-quality CNTs, the electric arc discharge method is discontinuous, unstable and unable to create a vast quantity of CNTs with high quality (Lim and Lin, 2011).

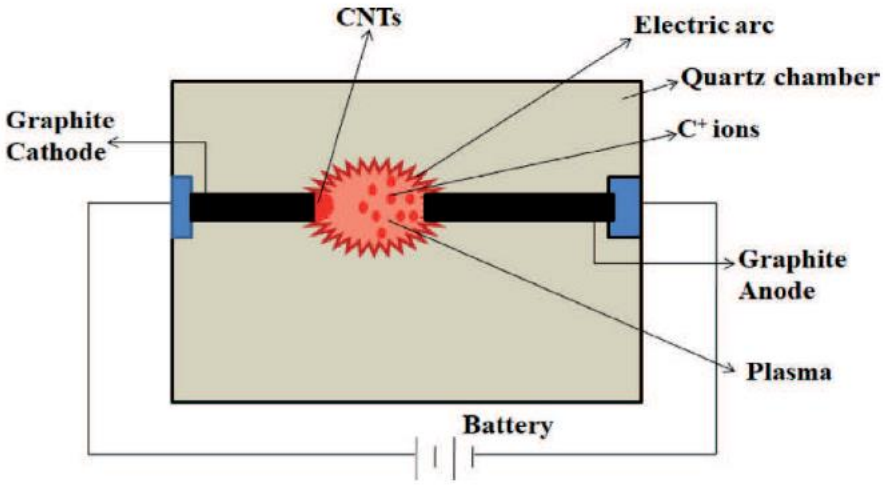

Figure 8: Schematic diagram of an electric arc discharge setup (Jagadeesan *et al.*, 2020)

Laser ablation method

The laser ablation technique is a physical vapor deposition process wherein a laser source evaporates a graphite target (Jagadeesan *et al.*, 2020). Using this technique, a piece of graphite target is positioned in the middle of a quartz chamber and is then heated to a high temperature in an inert atmosphere using a laser. The reaction temperature has been discovered to affect the quality and yield of these CNT products (Lim and Lin, 2011). A reaction temperature of 1200°C has been found to be the optimum for the production of quality CNTs (Lim and Lin, 2011). Lower temperatures cause the CNTs' structural quality to deteriorate and their number of defects to increase (Lim and Lin, 2011). Continuous or pulse laser sources are the two types of sources that can be used to evaporate the graphite target (Jagadeesan *et al.*, 2020). The flow of an inert gas vaporises the target atoms (carbon), which are subsequently swept into a cooled copper collector. On the cooled copper collector, carbon atoms are deposited and grow into CNTs (Jagadeesan *et al.*, 2020). A schematic representation of the laser ablation method is shown in Figure 9.

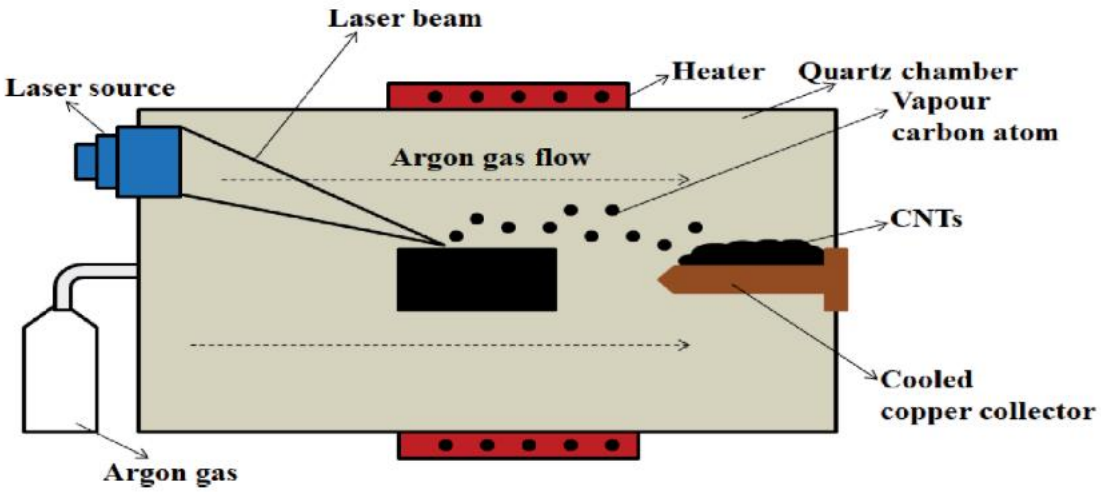

Figure 9: Schematic illustration of laser ablation method (Jagadeesan *et al.*, 2020)

Chemical vapor deposition method

CVD is one of the most widely used thin film deposition techniques (Lim and Lin, 2011). It is also considered a medium temperature (typically 500°C – 900°C) and long reaction technique when compared to electric arc discharge and laser ablation techniques (Lim and Lin, 2011). In this method, CNTs are synthesised using a mixture of a hydrocarbon gas (acetylene, ethylene, methane etc.) and an inert gas (nitrogen, argon). Regardless of its basic form whether solid or liquid, the precursor must be in gaseous form when it reaches the catalyst's surface (Shudin *et al.*, 2021). The most commonly used hydrocarbons are ethylene, acetylene, and methane (Tran *et al.*, 2007).

An illustration of a CVD setup is shown in Figure 10. CNT growth is accomplished in a temperature-controlled furnace. A quartz tube with a quartz boat containing the substrate coated with catalyst nanoparticles in the middle is placed inside the furnace. The most commonly used catalysts in the CVD method are Fe, Ni and Co (Lim and Lin, 2011) (Ismail *et al.*, 2008). A mixture of the gases is purged into the quartz tube for a specific reaction time. At appropriate temperatures (500°C – 900°C) the carbon atoms dissolve in the metal particles and subsequently become saturated and form CNTs (Lim and Lin, 2011).

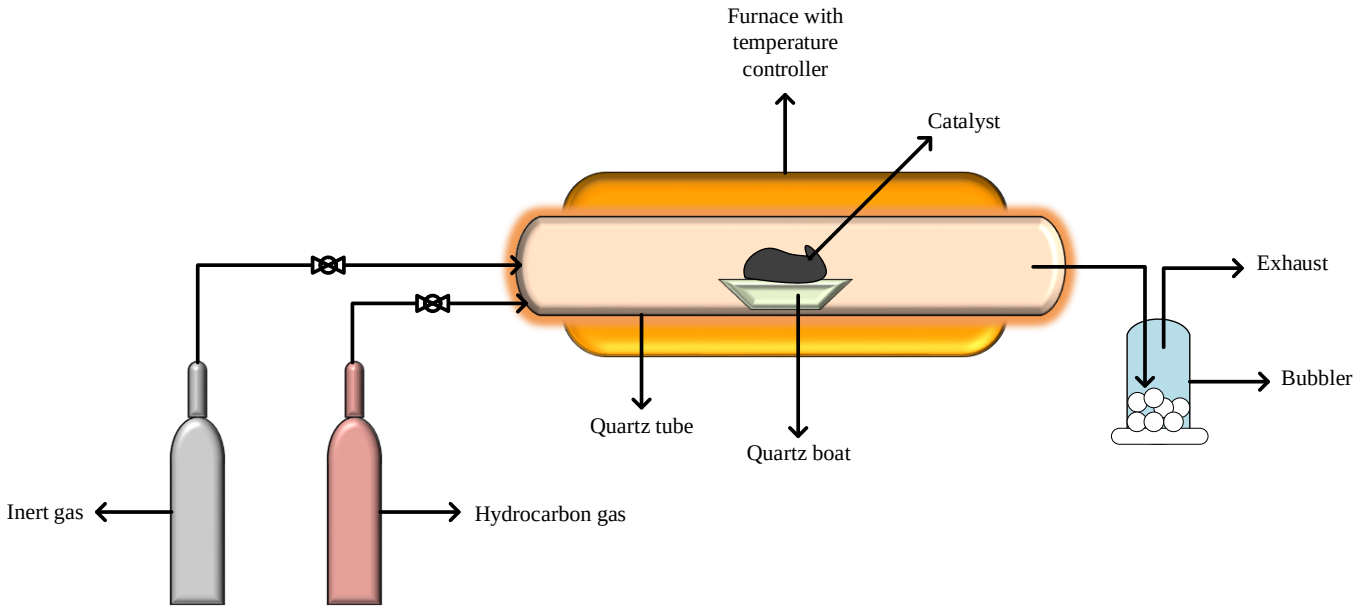

Figure 10: Schematic diagram of a CVD setup

The two widely accepted growth mechanisms of CNTs using the CVD method are tip growth and base/root (Wang *et al.*, 2019) (Shudin *et al.*, 2021). With the tip growth model, because of the inadequate catalyst-to-substrate contact, the carbon species that precipitate from the metal nanoparticles would rise to the surface as the catalyst particle is lifted (Chen and Zhu, 2015). In contrary the base/root growth model involves a strong interaction of the catalyst with the substrate, and the carbon species cannot push the catalyst upward to create tubular networks (Chen and Zhu, 2015). As a result, precipitation occurs at the catalyst's tip, where the catalyst nanoparticle stays pinned on the substrate and the carbon species diffuses upward (Chen and Zhu, 2015). These two growth mechanisms are illustrated in Figure 11.

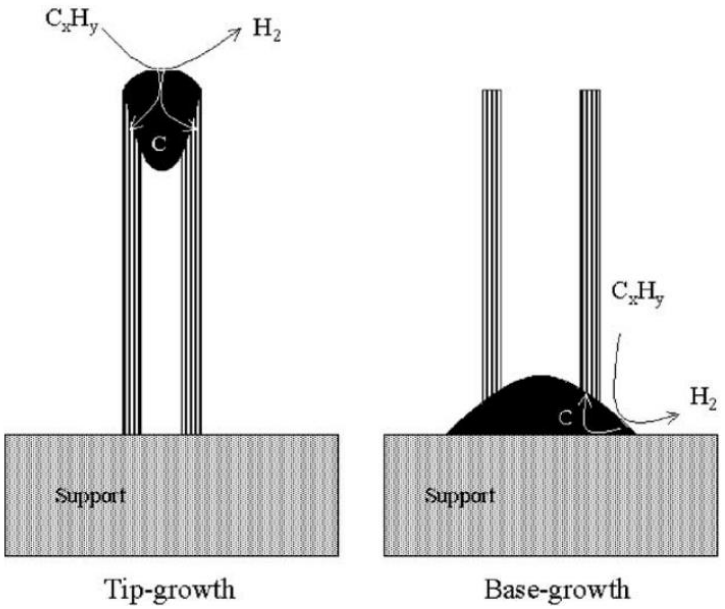

Figure 11: Schematic diagram of CNTs growth mechanisms (Dupuis, 2005)

Summary of the three most commonly used synthesis methods

Presented in Table 1 is a comparison summary of the three most commonly used synthesis methods for CNTs and Figure 12 is a graphical representation of the general processes in CNT research.

Table 1: Comparison of the major CNTs synthesis methods (Rathinavel *et al.*, 2021)

Process	**Electric Arc discharge**	**Laser Ablation**	**CVD method**
Yield	Moderate (70%)	High (80-85%)	High (95-99%)
Temperature, °C	1700	1200	700 - 900
Diameter, nm	40 - 30	10 - 20	20 - 25
Purity	High	High	High
Production rate	Low	Low	Low
Cost	High	High	Low
Process control	Difficult	Difficult	Easy
Energy requirement	High	High	Moderate
Advantages	Uncomplicated, Low cost, High-quality CNTs	Superior purity, Synthesis at ambient temperature	Uncomplicated, Superior purity, Large scale production
Disadvantages	Elevated temperature, Unpurified, Tangled CNTs	Restricted to laboratory scale	Imperfections in MWCNTs

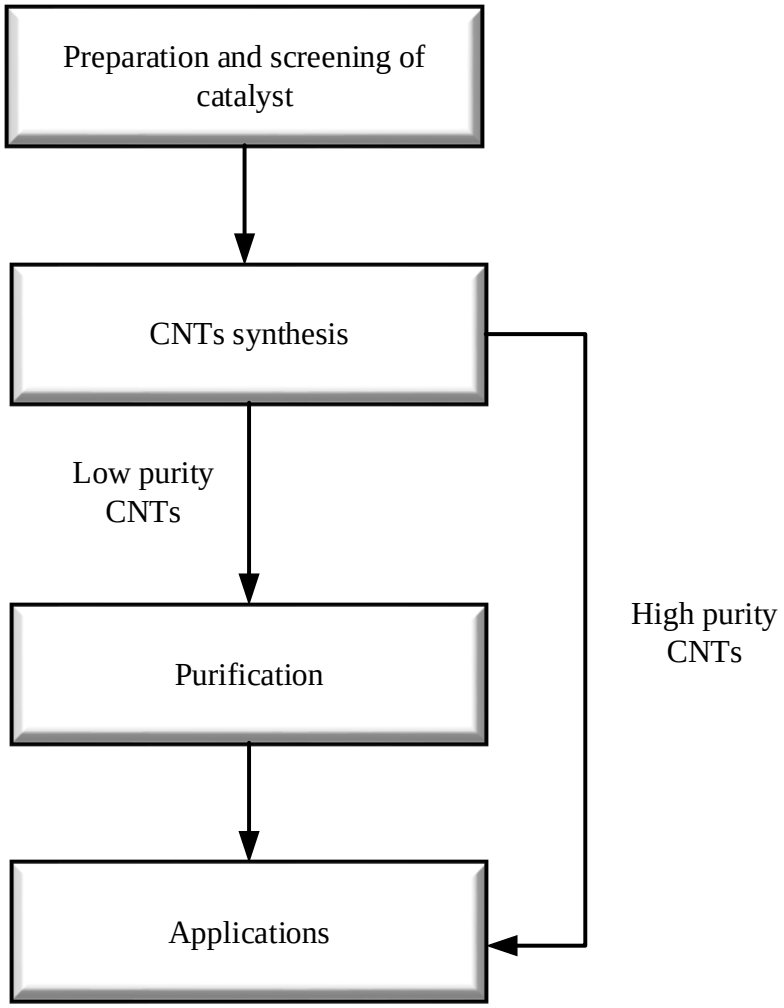

Figure 12: Typical procedures in CNTs research (Ismail et al., 2008)

2.2.3. Purification

CNTs synthesised using the methods discussed in Section 2.2.2 unavoidably include metal catalyst particles and carbonaceous impurities (Saifuddin *et al.*, 2013). These unpurified CNTs contaminants significantly lower their mechanical and electrical properties (Saifuddin *et al.*, 2013). Literature studies have shown that up to this far, all known CNTs synthesis methods generate CNTs with impurities (Saifuddin *et al.*, 2013). Purification following synthesis is therefore an essential step required in the manufacturing of CNTs (Tran *et al.*, 2007). This process entails removing amorphous particles, support material, residual catalyst particles and other graphitic impurities from the CNTs (Tran *et al.*, 2007) (Rathinavel *et al.*, 2021).

CNTs can be purified using three different methods namely; chemical, physical and multi-step methods (Ismail *et al.*, 2008). A graphical view of the purification methods is shown in Figure 13. Chemical purification entails the oxidation of synthesised CNTs in both wet and dry conditions (Ismail *et al.*, 2008). Concentrated acid solutions or strong oxidants are used under what is referred to as wet conditions (liquid phase), while air, oxygen, or other gases heated to a specific temperature are used under what is referred to as dry conditions (gas phase) (Ismail *et al.*, 2008). Chemical methods are the most commonly used methods for the purification of CNTs (Ismail *et al.*, 2008). The main concept in the chemical purification method is a selective oxidative etching procedure, which is predicated on the premise that amorphous carbon and carbon particles can be removed more readily than CNTs because of their higher rate of oxidation reaction (Ismail *et al.*, 2008) (Lim and Lin, 2011).

Physical purification is a method used when the aim is to lessen the damage that direct oxidation causes (Ismail *et al.*, 2008). These methods use mild conditions to separate impurities from CNTs. Filtration, ultra-sonication and chromatography are some of the physical purification methods used to purify CNTs (Ismail *et al.*, 2008). However, physical purification methods have proven not to be as effective as chemical methods in the purification of CNTs (Jagadeesan *et al.*, 2020). In the multi-step purification method, a combination of both chemical and physical methods is used. This technique is especially applied when it is not possible to eliminate all of the contaminants present in the CNTs at once with a single treatment (Ismail *et al.*, 2008).

The structural surface of the tubes is altered by these purification methods, which could lead to sudden variations in the mechanical response and electronic transport (Lim and Lin, 2011). Consequently, future efforts should focus on single-step methods of creating clean nanotubes to prevent chemical alterations and treatments from changing the intriguing characteristics of CNTs (Lim and Lin, 2011).

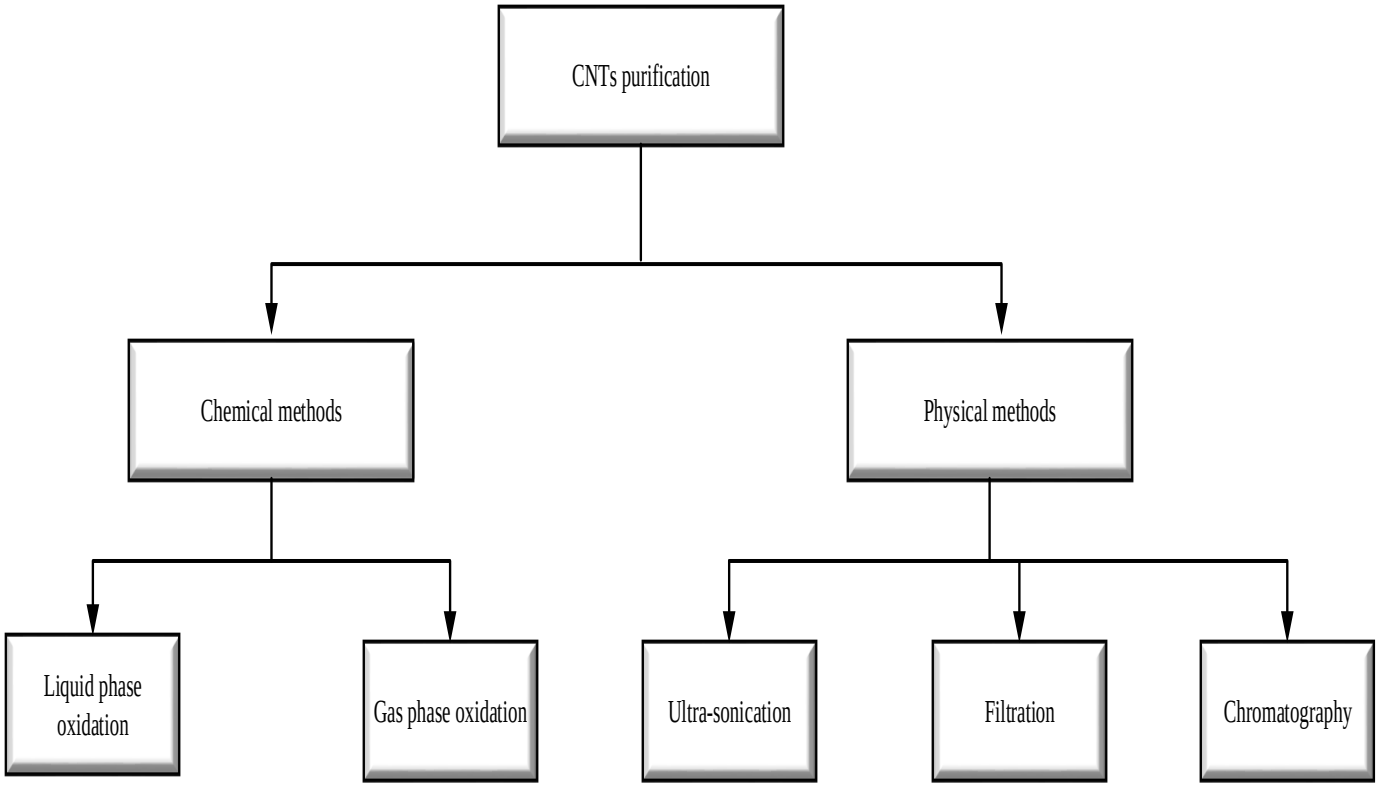

Figure 13: CNTs purification methods (Ismail et al., 2008)

2.2.4. Carbon nanotubes vs graphite as anode material

Unlike graphitic crystallites, which have a structural opening from the edge direction, a perfect CNT has a closed graphene sheet (Wu *et al.*, 2014). Only structural defects in the CNT can promote the diffusion of lithium ions. Unlike other carbonaceous materials like graphite, where the intercalation process is typical, the structural defects and capacitive surface adsorption in CNTs are responsible for lithium storage (Wu *et al.*, 2014). Furthermore, CNTs are not prone to pulverisation and therefore provide a way to greatly increase the capacity of the LIBs (De Las Casas and Li, 2012). The morphology and properties of CNTs as discussed in Section 2.2.1 make them a promising alternative anode material which may take the role of graphite and be used as anode material LIBs (De Las Casas and Li, 2012).

In addition to having a greater capacity than graphite, CNTs can also be employed as a support matrix to create innovative CNTs and metal composites that can benefit from the higher capacity of the metals (De Las Casas and Li, 2012). Nanoparticles of metals such as antimony (Sb) and tin (Sn) can be deposited on the surfaces of CNTs (De Las Casas and Li, 2012). Subsequently, these

particles can combine with lithium to produce an alloy without preventing the lithium from being intercalated into the CNTs (De Las Casas and Li, 2012). This eliminates the pulverization issue and allows the anode to benefit from the elevated lithium capacity exhibited by metals (De Las Casas and Li, 2012). The LIB storage capacity in the anode can further be improved through doping and or functionalisation of CNTs using heteroatoms (N, S, P or Si) (Lee *et al.*, 2010).

Graphite is best described as a stack of carbon sheets joined hexagonally and kept together by van der Waals forces (De Las Casas and Li, 2012). A pair of carbons in the same sheet exerts far greater forces on each other than the forces exerted by any two concurrent sheets (De Las Casas and Li, 2012). This difference in forces is the reason that lithium ions manage to be inserted in between the graphite planes (De Las Casas and Li, 2012). Due to its comparatively low expansion level after lithium insertion, graphite is the anode material of choice for LIBs. The low expansion level is a result of graphite being able to maintain charge capacity after several charge-discharge cycles (De Las Casas and Li, 2012). However, as an anode material in LIBs, it has a poor storage capacity (Xiong *et al.*, 2013). The reason for this is that during intercalation, every second carbon hexagon can only combine with one lithium-ion (refer to Figure 14) thus blocking other lithium ions from combining directly with adjacent interstitial sites (Xiong *et al.*, 2013). This leads to a limited theoretical specific capacity of 372 $mAhg^{-1}$ which has the potential of benefiting lithium-ion cells if increased. Hence graphite's common use in the market is because of cycle over cycle efficiency (De Las Casas and Li, 2012).

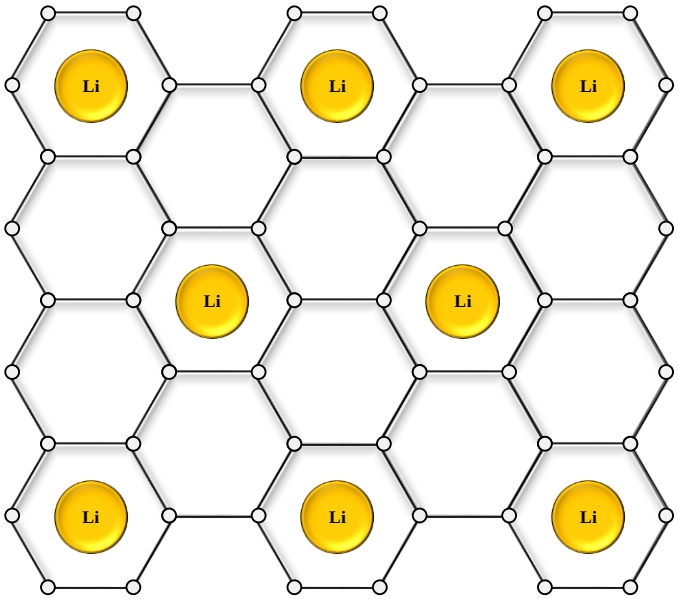

Figure 14: An illustration of Li intercalation in graphite (De Las Casas and Li, 2012)

2.3. Electrochemical principles

2.3.1. Fabrication of commercial LIBs

The electrode fabrication process involves the mixing of electrode constituents which include active material, binder and conductive particles in a solvent (Hawley and Li, 2019). These components support the electrode's mechanical integrity, energy and capacity, and electrical conductivity (Hawley and Li, 2019). Therefore, the selected mass ratios of the components must be such that the ideal blend of quantities is obtained (Zheng *et al.*, 2012). Furthermore, the choice of solvent determines which binders work best and whether other additives are needed (Hawley and Li, 2019).

Manufacturing of electrodes, cell assembly, forming, and inspection are all part of the fabrication process for commercial LIBs (H. Liu *et al.*, 2021). A schematic overview of the processes involved in the fabrication of commercial LIBs is shown in Figure 15. Slurry mixing, coating, drying, and calendering are methods that can be used to obtain the electrodes. The cell is subsequently put together by winding, filling the electrolyte, slicing the electrode and separator, and packaging (Hawley and Li, 2019) (H. Liu *et al.*, 2021). Quality control and cell development are the last two phases (Hawley and Li, 2019).

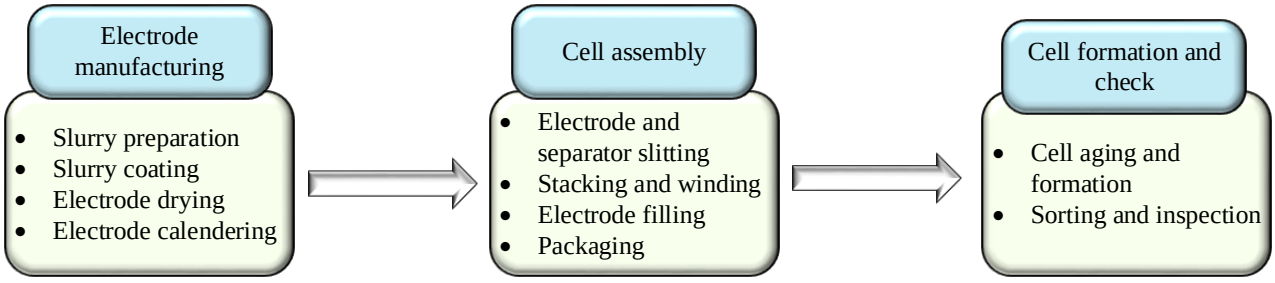

Figure 15: The fabrication process of commercial LIBs (H. Liu *et al.*, 2021)

2.3.2. Electrochemistry basic principles

The chemical processes connected to charge separation are collectively called electrochemistry (Brett *et al.*, 1994). Charge transfer is frequently the result of this charge separation and can happen either heterogeneously on electrode surfaces or uniformly in solution (Brett *et al.*, 1994). Electrochemical reactions at the electrodes produce the electronic current, which is the flow of

electrons in the external circuit (Pinkwart and Tübke, 2011). The movement of charge between the positive and negative electrodes within the electrolyte is carried out by ions, as opposed to the electric current in the external system (Pinkwart and Tübke, 2011).

Since electrode reactions are heterogeneous, the electrode can only move electrons to or from species in solution by acting as a source (for reduction) or a sink (for oxidation) (Brett *et al.*, 1994) according to the following equation:

$$O + n^{e-} \rightarrow R \tag{2.4}$$

Where O and R represent the oxidized and reduced species respectively. It may also participate in the electrode reaction, for example, in the dissolution of a metal M (Brett *et al.*, 1994):

$$M \rightarrow M^{n+} + ne^{-} \tag{2.5}$$

For electron transfer to happen, the energies of the electron orbitals in the donor and acceptor must match for the transfer to occur (Brett *et al.*, 1994). The working electrode (WE), counter electrode (CE), and reference electrode (RE) are the three electrodes that make up a standard electrochemical cell. They are all submerged in a charged electrolyte solution. The two most common types of three-electrode electrochemical cells are shown in Figure 16 and Figure 17.

Each of the three electrodes plays an important role in the electron transfer processes. The working electrode is the electrode where most of the electrochemical reactions take place. It is made up of redox-inert materials which are within the potential range of interest (Elgrishi *et al.*, 2018). The reference electrode is used as a reference point for measuring the potential of other electrodes. The main role of the counter electrode is the completion of the electric circuit when current flows after a potential is applied on the WE (Elgrishi *et al.*, 2018).

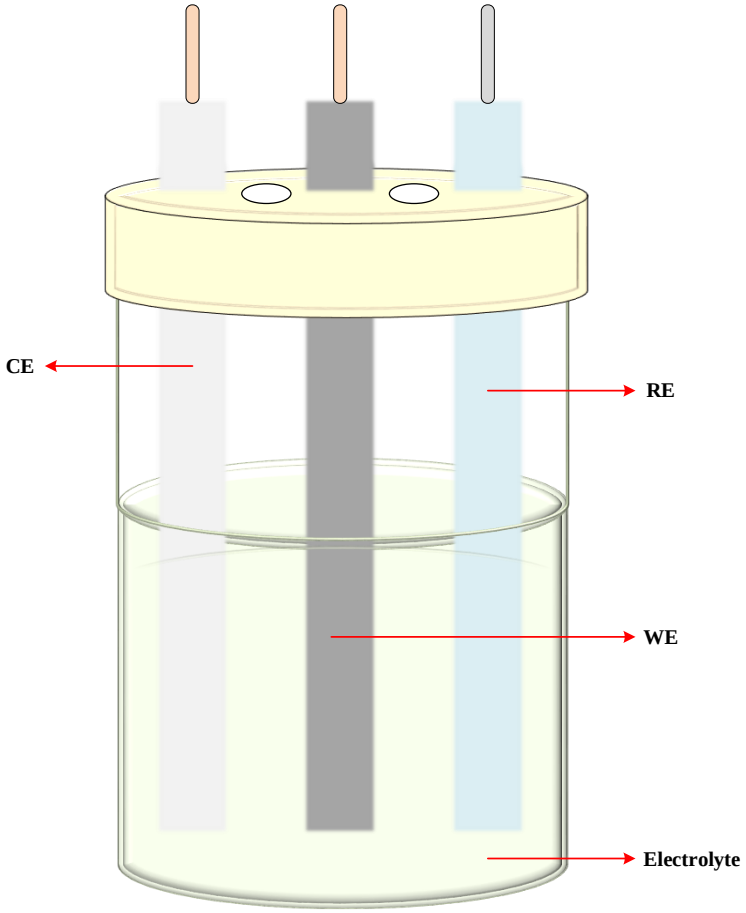

Figure 16: Schematic representation of a conventional three-electrode electrochemical cell

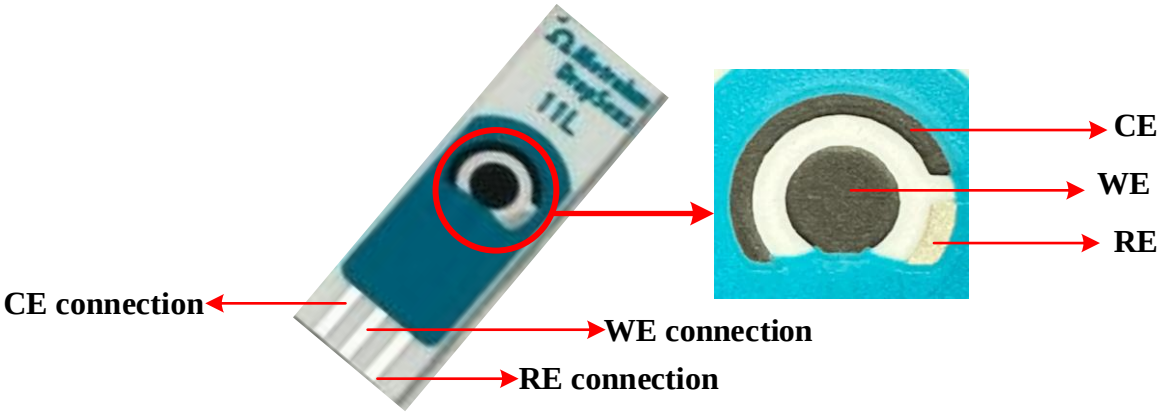

Figure 17: Screen-printed carbon electrode (SPCE)

2.3.3. Electrochemical characterisation

As part of the procedures typically followed for the research on CNTs (refer to Figure 12), when it comes to "Application", electrochemical characterisation plays a major role. The results determined via electrochemical characterisation provide details on the performance of anode materials in LIBs. Galvanostatic charge-discharge, electrochemical impedance spectroscopy, and cyclic voltammetry (CV) are some of the different kinds of electrochemical characterisation techniques. Only CV and EIS were investigated in this study and hence the next section will briefly discuss these two electrochemical characterisation methods.

Cyclic Voltammetry

CV is one of the most commonly used electrochemical techniques for the studying of reduction and oxidation processes of molecular species (Elgrishi *et al.*, 2018). As such, it plays a major role in determining the potential window for the electrochemical cycling of the anode materials. The three-electrode electrochemical cell is used for the CV experiment.

The working principle of the CV technique involves the measurement of current (I) as a result of sweeping the potential (E) at a predetermined scan rate (v). A potentiostat is used for the measurement of the open circuit potential. In a typical CV experiment, the initial potential (E_1) at the beginning of the time (t_0) is applied to the working electrode and is ramped linearly (refer to Figure 18) up to the switching potential (E_2) at a constant scan rate. The direction of the sweep is subsequently reversed, and the potential is swept from E_2 to E_1 for the completion of one cycle. This ramping can be repeated for as much as needed even at various scan rates. Charge moves from the WE to the CE during the experiment. The resulting plot termed a cyclic voltammogram is recorded on a computer as a graph of current versus potential (Gamry Instruments, 2017). An example of a generic cyclic voltammogram is shown in Figure 19, where i_{pa} and i_{pc} represent the anodic peak current and cathodic peak current respectively.

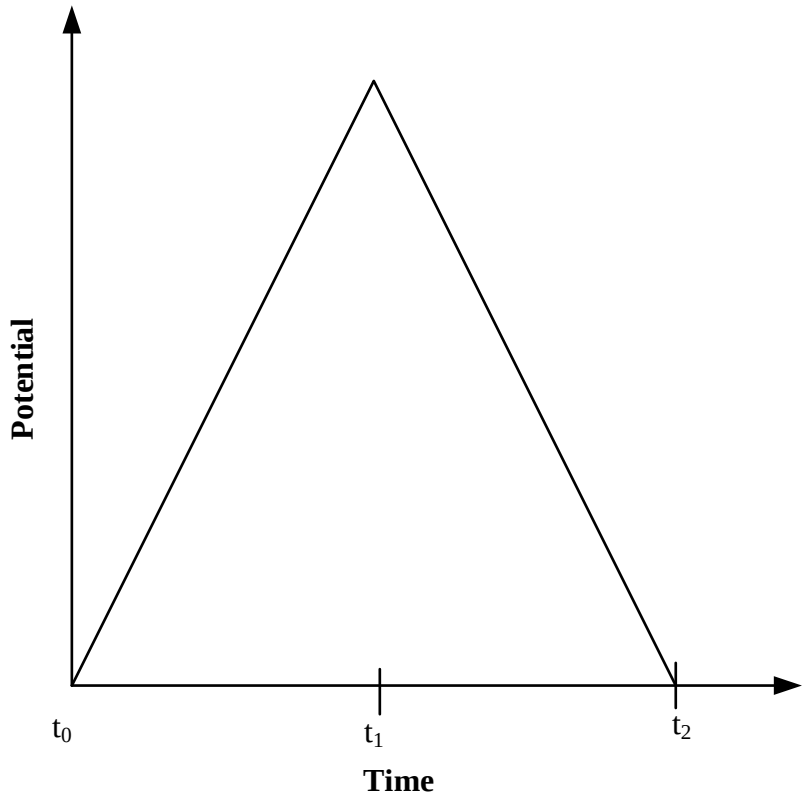

Figure 18: A potential profile of one CV scan

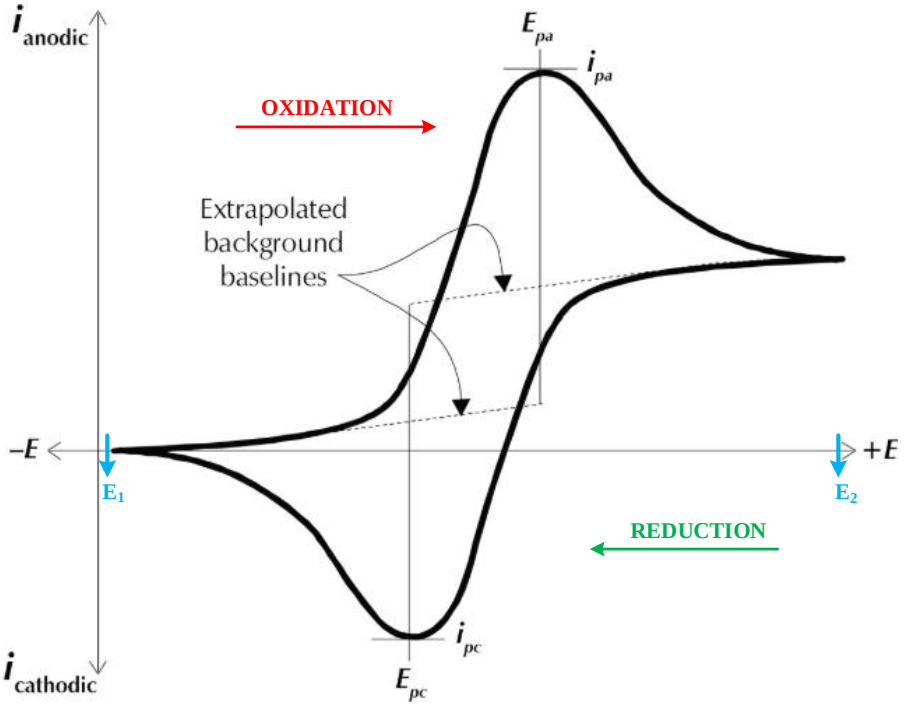

Figure 19: A generic cyclic voltammogram, modified from (Gamry Instruments, 2017)

Electrochemical Impedance Spectroscopy (EIS)

EIS is a commonly used non-destructive technique for characterising LIBs (Meddings *et al.*, 2020). It is a technique that is frequently employed to investigate the processes of interfacial charge transfer (Baranski, 1991). A battery's internal impedance is a crucial feature that influences its practical capacity as well as its rate capability, efficiency, and operating voltage (Meddings *et al.*, 2020). The deterioration of the electrolyte, electrode materials, and electrical connections within the cell causes impedance to generally increase with cell age (Meddings *et al.*, 2020). This method allows for the simultaneous measurement of the full electrochemical response including the diffusion coefficient of the redox species in solution, and double-layer capacitance all in a single experiment (Baranski, 1991).

An electrochemical cell, a potentiostat or galvanostat, plus a frequency response analyzer (FRA) make up a standard electrochemical impedance experiment setup (Metrohm Autolab, 2019a). To ascertain the system's impedance, the FRA applies a sine wave and evaluates the system's response (Metrohm Autolab, 2019a). This process is performed at several frequencies, usually between kHz and mHz, to produce a distinctive impedance spectrum (Meddings *et al.*, 2020). With resistance (R), according to Ohm's law, voltage (V) and current (I) are not time dependant and sinusoidal functions (DC theory i.e. frequency equals 0Hz)) (Princeton Applied Research, no date) and can be expressed as:

$$R = \frac{V}{I} \tag{2.6}$$

However, with impedance (Z) where the frequency is not equal to zero because of it being V and I being time dependant and sinusoidal functions (Princeton Applied Research, no date), Equation 2.6 is expressed as:

$$Z = \frac{V(t)}{I(t)} \tag{2.7}$$

After the application of the frequency potential at the specified amplitude (V_o) and radial frequency (ω), V(t) is subsequently expressed as:

$$V(t) = V_o \sin(\omega t) \tag{2.8}$$

EIS is normally expressed in terms of linear frequency, f, having the units of Hz and ω is expressed as (Gamry Instruments, 2017):

$$\omega = 2\pi f \tag{2.9}$$

The current response I(t) after the frequency application is shifted in phase φ to a different amplitude I_0 is expressed as:

$$I(t) = I_o \sin(\omega t + \varphi) \tag{2.10}$$

The impedance of the system from equation 2.4 is subsequently expressed as:

$$Z = \frac{V_o + \sin(\omega t)}{I_o \sin(\omega t + \varphi)} = Z_o \frac{\sin(\omega t)}{\sin(\omega t + \varphi)} \tag{2.11}$$

Thus, using the Eulers relationship, the impedance is defined in terms of a magnitude, Zo, and a phase shift, φ (Gamry Instruments, 2017):

$$\exp(j\varphi) = cos\varphi + jsin\varphi \tag{2.12}$$

The impedance is thereafter expressed as a complex function:

$$\begin{aligned} Z(\omega) &= Z_0 \exp(j\varphi t) \\ &= Z_0[\cos(\omega t) + jsin(\omega t)] \end{aligned} \tag{2.13}$$

The sum of the impedance is therefore composed of the real part and imaginary part of the impedance hence simplified and expressed as:

$$Z = Z' + jZ'' \tag{2.14}$$

The imaginary part (Z'') of the impedance is subsequently plotted on the y-axis and the real part (Z') on the x-axis resulting in what is termed the "Nyquist plot". A typical Nyquist plot for LIBs is shown in Figure 20. As shown in Figure 20, a Nyquist plot normally consists of several semi-circles or a single semicircle or two half semicircles and a ~45° angle straight line known as the Warburg (W) at low frequencies and provides details on the species' (Li^+) diffusion coefficient

(Metrohm Autolab, 2019b). The form of a Nyquist plot is determined by the composition of the working electrode and the electrochemical reactions that take place in the bulk solution or at the electrode surface. (Magar *et al.*, 2021). In the high-frequency range, the electrolyte resistance (Rs) is typically correlated with the intercepts of the semicircle and horizontal coordinate (Gao *et al.*, 2024). The radius of the semicircle is a representation of the electrode charge transfer resistance (Rct). (Gao *et al.*, 2024).

Using the Nyquist plot has the benefit of providing a concise summary of the data, allowing for qualitative interpretations to be made (Metrohm, 2023). Moreover, the shape of the spectra determines the difference in the impedance of the materials to be seen (Westerhoff *et al.*, 2016). From data of the Nyquist plot, the spectra can be fitted using an equivalent circuit model (ECM) (Westerhoff *et al.*, 2016).

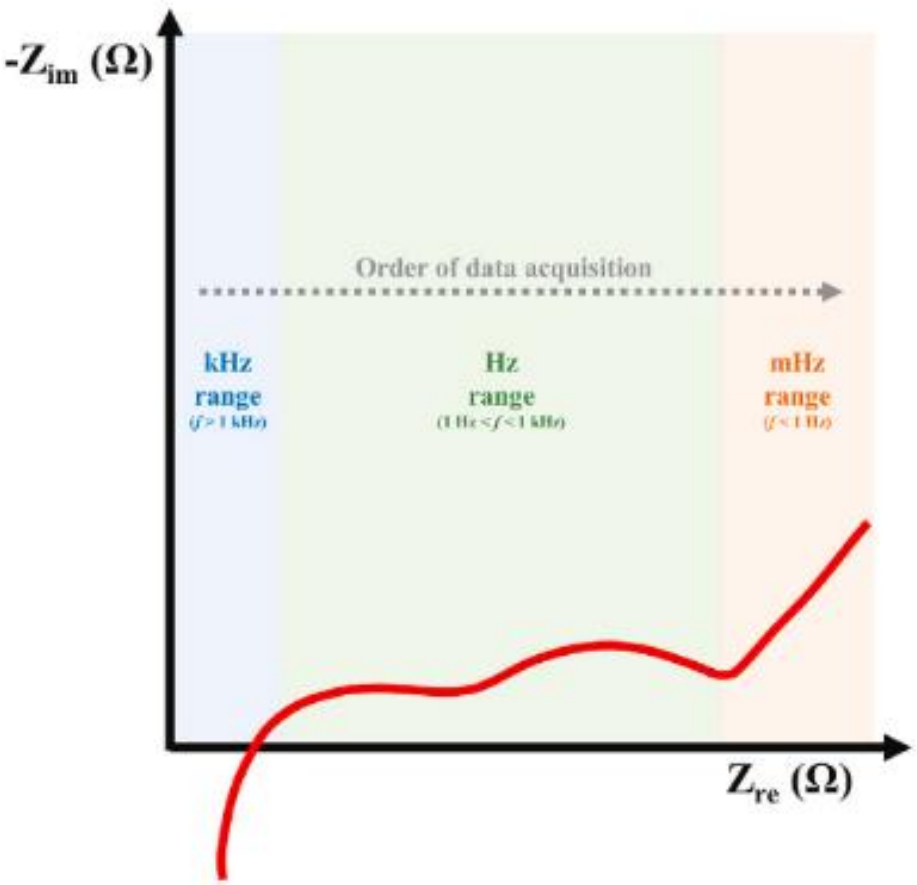

Figure 20: A typical Nyquist plot of a LIB (Meddings *et al.*, 2020)

One of the most basic electrical circuits for describing an electrochemical system is the Randles circuit (Westerhoff *et al.*, 2016). The Randles circuit typically consists of the following electric compounds:

- Solution resistor (R_s)
- Polarisation resistor (R_p)
- Charge transfer resistor (R_{ct})
- Double layer capacitor (Cdl) or constant phase element (CPE)
- Warburg (Z_w)

The standard circuit elements used in the ECM using the Nova Software are presented in Table 2. The Randles circuit, which is frequently employed at the start of data fitting, is depicted in Figure 21.

Table 2: Equivalent circuit elements in the NOVA software

Circuit element	**Name**	**Symbol**
	Resistor	R
	Capacitor	C
	Inductor	L
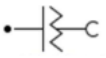	Constant Phase Element	Q or CPE
	Warburg	W
	Warburg-short circuit terminus	O
	Warburg-open circuit terminus	T
	Gerischer	G

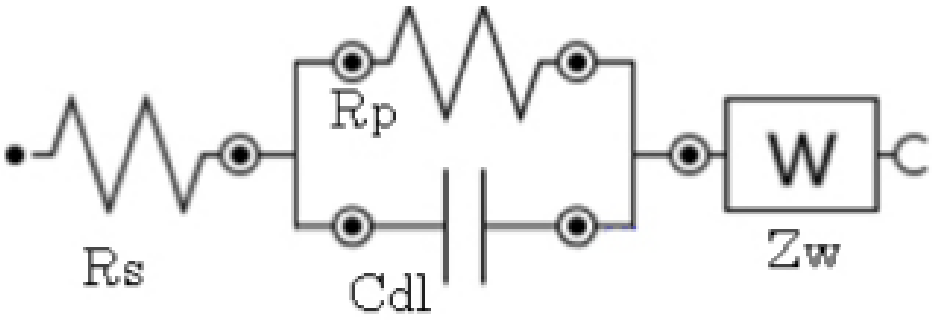

Figure 21: A typical Randles's circuit (Habekost, 2021)

An illustration of a Nyquist plot with the equivalent circuit is shown in Figure 22.

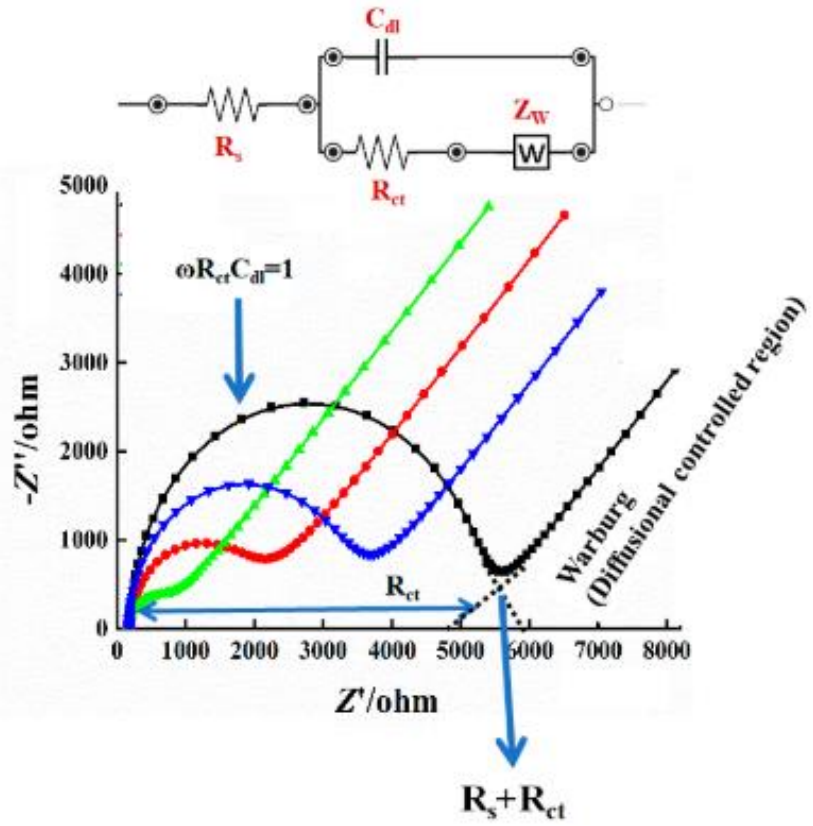

Figure 22: Nyquist diagram with the equivalent circuit (insert) (Magar *et al.*, 2021)

CHAPTER 3

3. EXPERIMENTAL PROCEDURES

The section describes how the catalyst used for the synthesis of the nanotubes in this study was prepared using the wet impregnation method. Details of how MWCNTs and SWCNTs were synthesised at various parameters (temperature, hydrocarbon precursor, and hydrocarbon flowrate) using the CVD method are also described. The CNTs were characterised using HRTEM, FESEM, XRD, BET, and Raman spectroscopy. Furthermore, this section details the fabrication of CNT/Li electrodes to be used as the working electrodes on the 3-electrode system in the electrochemical tests. Lastly, electrochemical testing of the working electrodes is described.

3.1. Catalyst preparation

Literature studies have shown that the growth and morphology of the nanotubes can be impacted by the metallic catalyst selected. Cobalt, iron, and nickel are the most commonly used transitional metals for the successful growth of CNTs (Szabó *et al.*, 2010)(Dupuis, 2005). A study by Kathyayini et al. 2004, observed that although iron is more active than cobalt, the resulting CNTs' quality in terms of graphitization and structure is lower when iron is used. Furthermore, studies have shown that the mixture of two transitional metals improves the catalyst performance in terms of quality (Dupuis, 2005). Therefore, a bi-metallic catalyst (Fe-Co) on a $CaCO_3$ support was subsequently selected for this study. The selection of the support was based on studies conducted by (Kathyayini *et al.*, 2004) and (Mhlanga *et al.*, 2009) which showed that $CaCO_3$ was a good support for the production of CNTs via CVD due to its easy removal using mild acids.

The catalyst was prepared using the wet impregnation method. $Fe(NO_3)_3.9H_2O$ and $Co(NO_3)_2.6H_2O$ were used as the Fe and Co sources. A Fe-Co precursor solution was prepared by dissolving appropriate amounts of Fe and Co in deionized water. Following the addition of the solution to the $CaCO_3$ support, the mixture was allowed to agitate for 30 minutes. Thereafter, it was filtered, and the residue was dried for 16 hours at 120°C in an oven. The dried residue was ground and calcined at 400°C for 20 hours. After calcination, the calcine was pulverized with a mortar and pestel before being screened to $P_{100} \leq 150\mu m$. The powdered catalyst was submitted for HRTEM, FESEM, XRD, and BET for characterisation. Figure 23 illustrates the schematic diagram of the catalyst preparation.

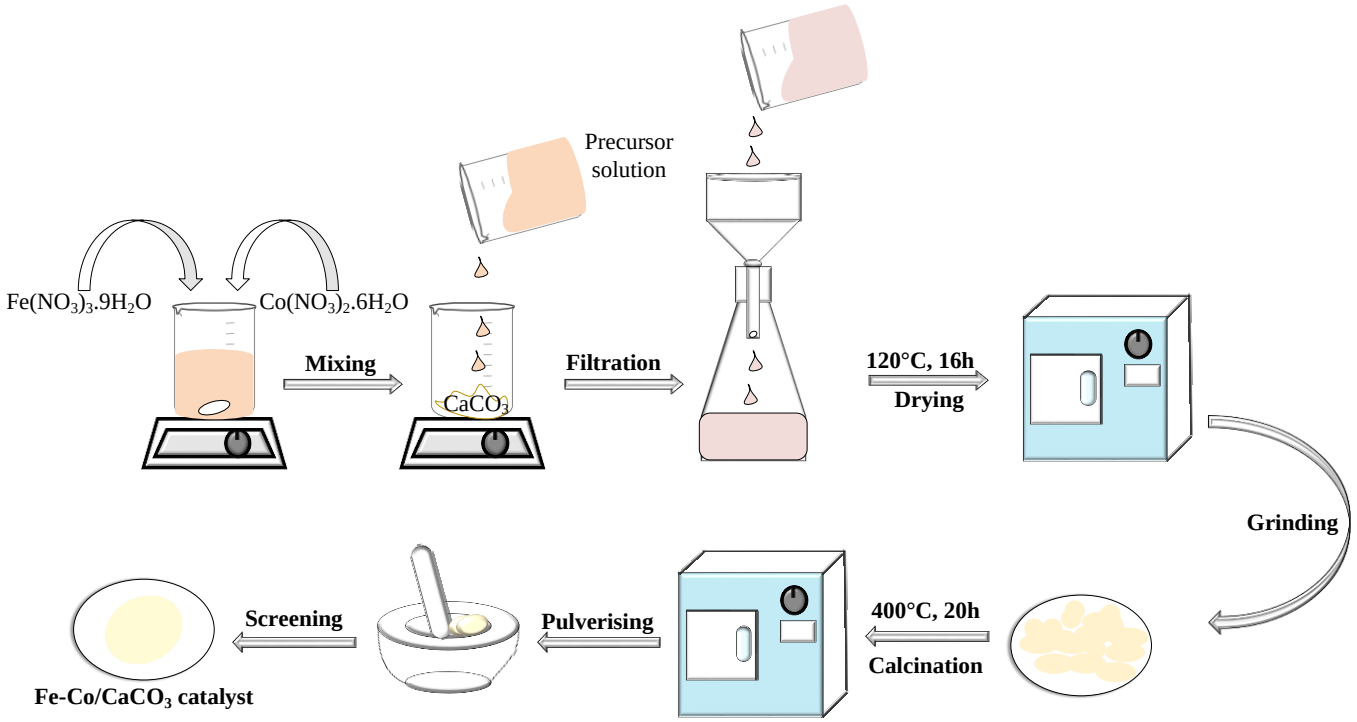

Figure 23: Schematic diagram of the catalyst preparation

3.2. CNTs synthesis

There are several methods used for the synthesis of CNTs, however, studies as discussed in Section 2.2.2 show that CVD is the commonly used technique due to its inexpensive and continuous mass production nature (Coquay *et al.*, 2002) (Szabó *et al.*, 2010). This study also used CVD for the synthesis of CNTs. The following parameters were varied:

- Temperature
- Precursor flowrate
- Type of hydrocarbon

3.2.1. MWCNTs synthesis

The test work matrix for the synthesis of MWCNTs is presented in Table 3. The samples synthesised using acetylene at flowrates 90 and 120 mL/min were labelled starting with the target synthesis temperature followed by A90 and A120 respectively. The samples synthesised using ethylene at a flowrates 90 and 120 mL/min were labelled starting with the target synthesis temperature followed by E90 and E120 respectively.

Table 3: Test work matrix for MWCNTs synthesis

Sample	Hydrocarbon	Synthesis temperature, °C	Carrier gas flowrate (N_2), mL/min	Hydrocarbon flowrate, mL/min
650°C-A90	acetylene	650	240	90
700°C-A90		700		
750°C-A90		750		
800°C-A90		800		
650°C-E90	ethylene	650	240	90
700°C-E90		700		
750°C-E90		750		
800°C-E90		800		
650°C-A120	acetylene	650	240	120
700°C-A120		700		
750°C-A120		750		
800°C-A120		800		
650°C-E120	ethylene	650	240	120
700°C-E120		700		
750°C-E120		750		
800°C-E120		800		

For the MWCNT, acetylene (C_2H_2) and ethylene (C_2H_4) were used as the carbon precursors, with nitrogen as carrier gas. The reaction was conducted at four different temperatures (650°C, 700°C, 750°C and 800°C) to evaluate the effect of temperature on the nature and quality of the nanotubes formed. The Fe-Co/$CaCO_3$ catalyst (1g) was placed in a quartz boat and thinly spread throughout before being inserted in the middle of a quartz tube. The tube was subsequently placed inside an electronically controlled horizontal furnace shown in Figure 24. The temperature of the furnace was ramped at 10°C min^{-1} with nitrogen flowing at 50 mL min^{-1} until the target temperature was reached. The flow of nitrogen was thereafter increased to 240 mL min^{-1}, and the hydrocarbon was introduced at the desired flowrate. Once the reaction time (60 min) was reached, the furnace was switched off and the flow of the hydrocarbon was stopped. The furnace was allowed to cool down to room temperature with nitrogen gas continuously flowing at a flowrate of 50 mL min^{-1}. The CNTs formed were collected from the quartz boat and the walls of the quartz tube and subsequently weighed. To remove any residual catalyst and support, the CNTs were washed in diluted nitric acid at ambient temperature for about 30 minutes. After the acid treatment, the contents were filtered and washed with excess de-ionised water and subsequently dried in an oven at 60°C for 8

hours. The dried CNTs were thereafter characterised by HRTEM, FESEM, XRD, BET, and Raman spectroscopy. Figure 25 illustrates the schematic diagram of the MWCNTs synthesis process.

Figure 24: Horizontal CVD furnace

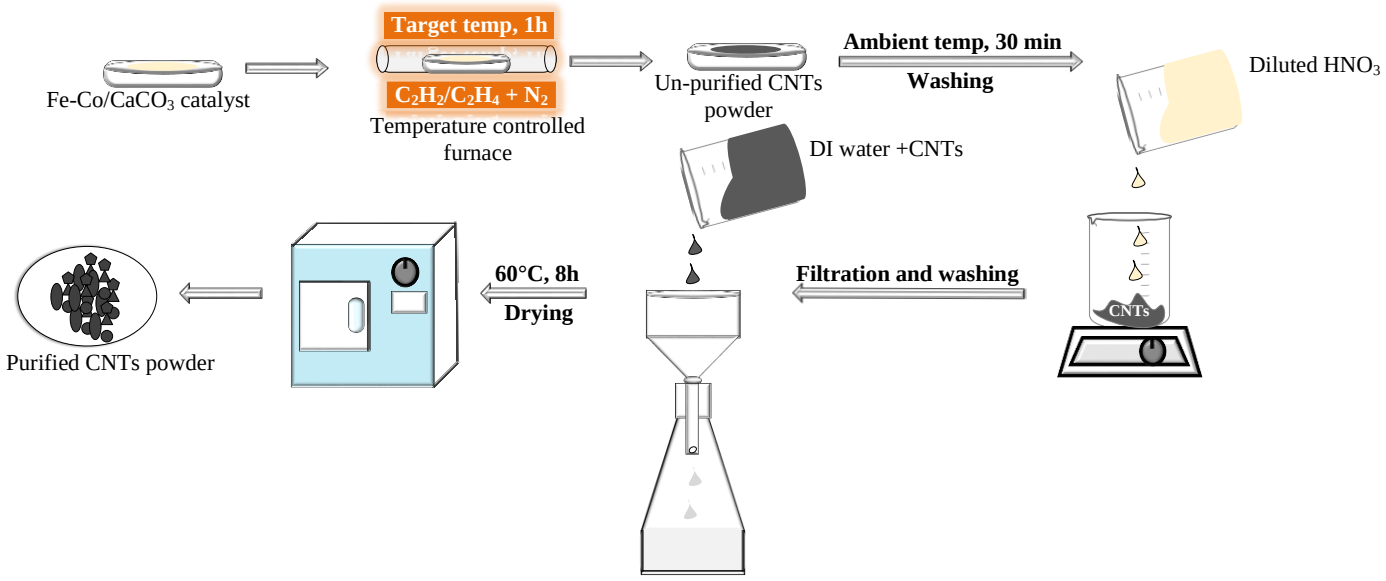

Figure 25: Schematic diagram of the MWCNTs synthesis process

3.2.2. SWCNTs synthesis

The test work matrix for the synthesis of SWCNTs is presented in Table 4. The samples synthesised using methane at flowrates 100 and 150 mL/min were labelled starting with the target synthesis temperature followed by M100 and M150 respectively.

Table 4: Test work matrix for SWCNTs synthesis

Sample	**Hydrocarbon**	**Synthesis temperature, °C**	**Carrier gas flowrate (Ar), mL/min**	**Reaction gas flowrate (H_2), mL/min**	**Hydrocarbon flowrate, mL/min**
700°C-M100	methane	700	50	100	100
800°C-M100		800			
900°C-M100		900			
700°C-M150	methane	700	50	100	150
800°C-M150		800			
900°C-M150		900			

Methane was used as the carbon precursor and a mixture of hydrogen and argon was used as the carrier gas. Methane is the most commonly used carbon precursor for SWCNTs growth according to studies conducted previously (Lim and Lin, 2011). Methane is further known for producing high-purity and high quality SWCNTs (Su *et al.*, 2000). The study further identified hydrogen to be the suitable reaction gas to be used with methane for the growth of SWCNTs. The role of hydrogen was to reduce the metal oxides in the Fe-Co/$CaCO_3$ catalyst to metallic form. The role of the argon was to keep an inert atmosphere during the synthesis process. Hence for this study, the combination of methane and hydrogen was selected for the growth of SWCNTs. The reaction was conducted at three different temperatures (700°C, 800°C, and 900°C) to evaluate the effect of temperature on the formation of CNTs. The Fe-Co/$CaCO_3$ catalyst (1g) was placed in a quartz boat and thinly spread throughout before being inserted in the middle of a quartz tube. The tube was subsequently placed inside an electronically controlled horizontal furnace (Figure 24). The temperature of the furnace was ramped at 10°C.min^{-1} under the flow of argon (50 mL min^{-1}) until the target temperature was reached. The flow of argon was thereafter stopped, and hydrogen and methane were introduced individually at desired flowrates. Once the reaction time (60 min) was reached, the furnace was switched off and the flow of methane and hydrogen was stopped. While argon gas was continually flowing into the furnace at a rate of 50 mL min^{-1}, the furnace was

allowed to cool to room temperature. The CNTs formed were collected from the quartz boat and the walls of the quartz tube and subsequently weighed. The same purification method used for the MWCNTs (Section 3.2.1) was applied to these CNTs. The dried CNTs were thereafter submitted for characterisation. The schematic diagram for the SWCNTs synthesis process is the same as the one for MWCNTs (refer to Figure 25) except for the hydrocarbon gas, carrier gas and reaction gas that was used.

3.3. CNT characterisation

To determine the effect of the various parameters on the morphology of CNTs the materials were characterised using different techniques. The structure and morphology of the prepared CNTs were inspected by HRTEM (TEM JEM-2100, JEOL Ltd., Tokyo Japan) operated at an accelerated voltage of 200 kV. For the HRTEM observation, the prepared CNTs were sonicated in ethanol for 30 minutes and thereafter dispersed on a holey carbon-coated copper grid.

To further study the morphology and structure of the prepared CNTs, imaging using a Zeiss Supra55 VP FESEM (Supra 55VP, Carl Zeiss, Germany) equipped with an Oxford Inca (Oxford Instruments, United Kingdom) microsystem was conducted. Secondary electron images were taken of a field representative of the general appearance of the sample at 2000x, 5000x, 10000x, 15000x, 20000x, and 25000x. The FESEM was equipped with energy dispersive X-ray spectrometry (EDX) attachment which measured the general semi-quantitative composition of each sample.

XRD was used for the determination of the crystal structure of the samples. A back loading preparation method was utilised for the preparation of the XRD samples. A Malvern Panalytical Aeris diffractometer (Malvern Panalytical Ltd., Netherlands) with a PIXcel detector and fixed slits filled with Fe-filtered Co-Kα light was used to obtain the diffractograms. The diffractograms were examined and processed using X'Pert Highscore Plus software.

To confirm the growth and determine the structural purity of the prepared CNTs, Raman spectroscopy was used. The Raman spectrum was determined by a WITec Alpha300R Confal Raman (WiTech GmbH, Germany) micro spectrometer with a laser excitation wavelength of 532 nm.

The surface area and pore volume of the prepared CNTs were determined using a BET analyser (Quantachrome Instruments, Anton Paar, USA).

3.4. Fabrication of CNT/Li electrode

It should be noted that not all the synthesised CNTs underwent electrochemical testing. CNTs which reported the highest surface area (i.e. samples synthesised at 650 and 700°C) were selected for electrochemical testing. Furthermore, commercial graphite was also used for electrochemical testing and the fabrication of these electrodes was the same as the one employed for the CNTs samples.

The working electrode (WE) was composed of CNTs (85 wt%), polyvinylidene difluoride (PVDF, 10 wt%) binder and acetylene black (5 wt%). The powders were dispersed in N-methyl-2-pyrrolidone (NMP) by sonication in a water bath for 30 minutes. Screen-printed carbon electrodes (SPCEs) from Metrohm Drop Sens model DRP-11L: 3.4×1.0×0.05 cm were used for all the electrochemical investigations. The WE was made of glassy carbon, the counter electrode (CE) was made of carbon and the reference electrode (RE) was made of Ag/AgCl as shown in Figure 26 (also refer to Figure 17). The geometric area of the WE was 0.11 cm^2. The prepared suspension (~3µL) was drop casted using a micropipette on the WE surface of the SPCE and left to dry in an oven at 50°C for 30 minutes. An illustration of the steps used for the fabrication of the CNT/Li electrodes is shown in Figure 26. It should be noted that as a quality measure, three CNT/Li electrodes were prepared for each sample.

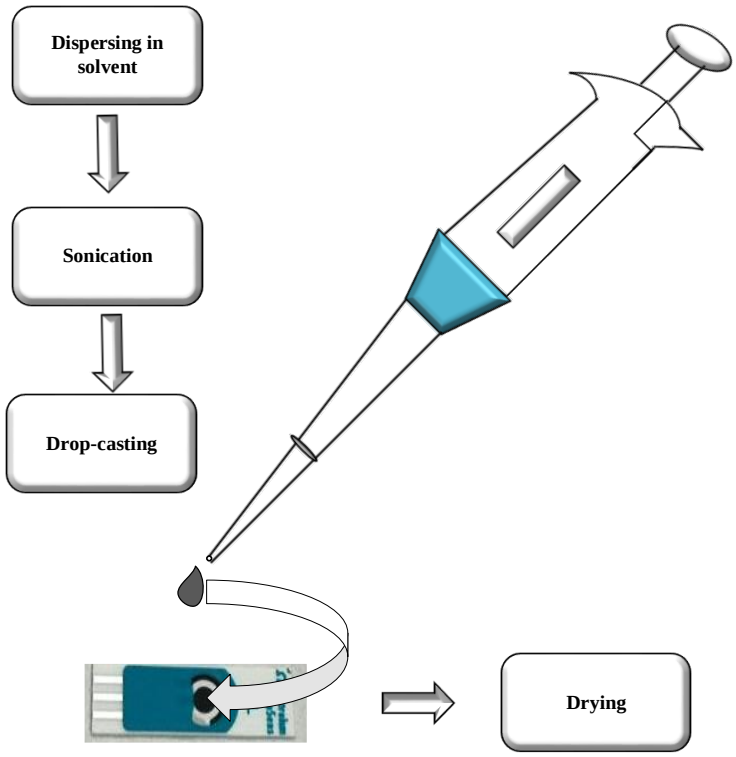

Figure 26: The steps involved in the fabrication of the electrodes

3.5. Electrochemical measurements

The CNT/Li electrodes as prepared in Section 3.4 were subjected to CV and EIS testing. The main aim of these electrochemical techniques was to investigate the electrochemical performance of the synthesised materials.

The electrochemical measurements were performed with a Metrohm Autolab PGSTAT302N electrochemical workstation shown in Figure 27. All tests were performed at room temperature. The WEs were fabricated as described in Section 3.4. A mixture of 1:1 (volume) of ethylene carbonate (EC) and dimethyl carbonate (DMC) in a solution of 1M LiPF6 was used as an electrolyte. The CV tests were conducted at scanning rates of 5 mVs^{-1} and 10 mVs^{-1} at a potential window of 0.02 to 0.8V for 4 cycles. Potentiostatic EIS measurements were performed at an AC voltage of 5 mV from 10 kHz to 0.01 Hz frequency range. The impedance spectra were fitted to the equivalent circuit using the fitting and simulation on Nova 2.1.

Figure 27: Electrochemical measurement setup

CHAPTER 4

4. RESULTS AND DISCUSSION

4.1. Catalyst characterisation

The specific surface area (SSA) of our Fe-Co/$CaCO_3$ catalyst was found to be ~11.3 m^2/g in agreement with that (~10.8 m^2/g) reported by Mhlanga and co-workers (Mhlanga *et al.*, 2009). The pore size and pore volume of the catalyst reported ~ 2.0 nm and ~0.3 cm^3/g respectively. This pore size fell within the range (2 - 50 nm) of mesopores. This low pore size diameter may be beneficial during the CVD process in assisting with gas adsorption as it may mean an increase in the SSA of the catalyst (Birch *et al.*, 2013). A study by Mhlanga *et al.*, 2009 confirmed the increase in the SSA (almost double) of the catalyst after heating in the absence of a carbon source.

To study the morphology of the catalyst, HRTEM was employed. The HRTEM micrograph of the catalyst is depicted in Figure 28(a). It reveals the presence of small dark particles on the support ($CaCO_3$) which are presumed to be Fe-Co (indicated by red arrows). The morphology of the catalyst was further explored using FESEM coupled with EDS. The micrograph and EDS spectrum are presented in Figure 28(c) and (d) respectively. The FESEM image reveals the presence of a clustered solid catalyst. The corresponding EDS spectrum showed Ca as the prominent peak with small peaks of C, O, and Fe also observed. Details of the EDS spectrum is presented in Table 5.

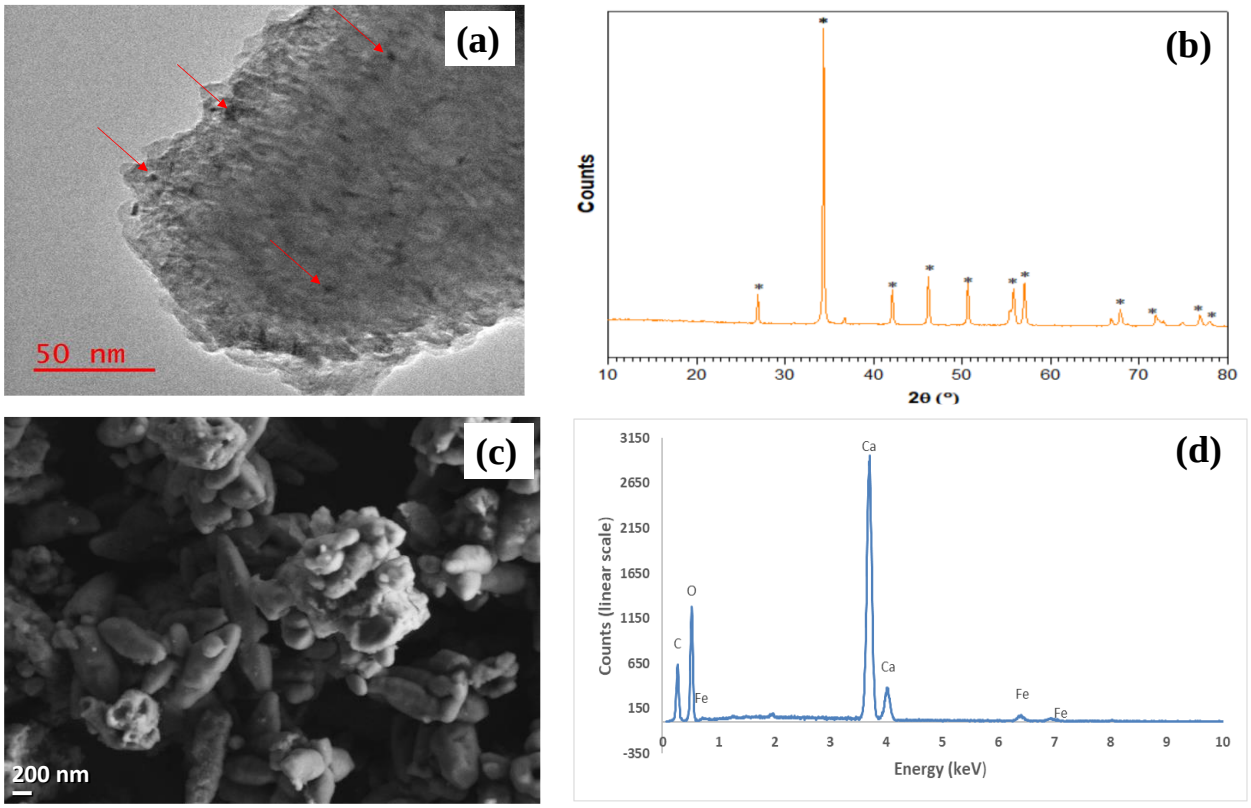

Figure 28: (a) HRTEM image, (b) XRD spectrum, (c) FESEM image, and (d) EDS spectrum of the Fe-Co/$CaCO_3$ catalyst

Table 5: Semi-quantitative composition of the catalyst determined by EDS microanalysis (wt. %)

Sample	C*	O	Ca	Fe	Co	Cu	Total
Fe-Co/$CaCO_3$	12.6	49.3	35.2	1.6	0.9	0.4	100.0

*carbon composition determined by difference

To investigate the crystal structure and phase identification of the catalyst, XRD analysis was performed. The XRD spectrum in Figure 28 (b) shows the most intense peak at a 2θ value of 34.31° and less intense peaks throughout the spectrum. The peaks marked by an asterisk (*) are ascribed to calcite (PDF-00-047-1733). Overall no broad peaks were observed in the spectrum and that suggested that the catalyst was highly crystalline (LibreTexts, 2022).

4.2. Characterisation of carbon nanotubes

The preparation of SWNCTs in this study could not successfully produce the intended SWNCTs but yielded MWCNTs. Literature studies have revealed that the tube structure of SWCNTs has a significant impact on their electrical characteristics and hence controlling the distribution of

nanotube diameters and chiralities in the final product is a primary objective in the production of SWCNTs (Bachilo *et al.*, 2003) (Ding *et al.*, 2009) (Liu *et al.*, 2012). However, studies have shown that the production of SWCNTs with predefined chirality has proven to be a considerable challenge for some time in the nanotube field (Liu *et al.*, 2012). For this study, commercial SWCNTs sample was acquired. However, after characterisation of the purchased SWCNTs, the results revealed that they were also MWCNTs. The characterisation results of supplier and those produced in this study are available in the Appendix (Section 7.1 and 7.2 respectively). Therefore, a decision was made to proceed with the work using only the MWCNTs produced in this study.

4.2.1. HRTEM study

The effect of acetylene flowrate (90 mL/min) at various synthesis temperatures

Representative HRTEM micrographs from the various temperatures are presented in Figure 29. The micrographs of samples 650°C-A90 and 700°C-A90 in Figure 29 (a) and (b) revealed that at these synthesis temperatures, the CNTs were MWCNTs in nature. However, the MWCNTs formed at both these temperatures were a mixture of bamboo-like CNTs and curled-spaghetti-like CNTs. These CNTs however also contained some residual catalyst particles which were identified by the dark spots in the tube cavities. Due to the position in which the residual catalyst particles were located, an assumption could be made that the tubes were formed via the base-growth mechanism (Chen and Zhu, 2015) described in Section 2.2.2. Measurement of the outer diameter of the CNTs using the Image J software as shown in Figure 30 are averages of 20 nm and 25 nm for samples of 650°C-A90 and 700°C-A90 respectively. The outer diameter (25 nm) for 700°C-A90 was within the range (15 nm to 30 nm) reported in a study by Mhlanga et al. where similar test conditions were employed (Mhlanga *et al.*, 2009).

As the synthesis temperature was increased from 700°C to 800°C, the formation of what appeared to be non-tubular carbon and carbon nanofibers was observed for 750°C-A90 and 800°C-A90 respectively as shown in Figure 29(c) and (d). Studies by other researchers showed that elevated temperatures could lead to the sintering of the metal particles, and the formation of pyrolytic amorphous carbon (Danafar *et al.*, 2009). Another explanation for the formation of the non-tubular CNTs may be the increase in the number of walls as the synthesis temperature increases. This assumption was supported by the increase in the outer diameter of 750°C-A90 and 800°C-A90.

The outer diameters (see Figure 30) for 750°C-A90 and 800°C-A90 reported averages of 60 nm and 89 nm respectively.

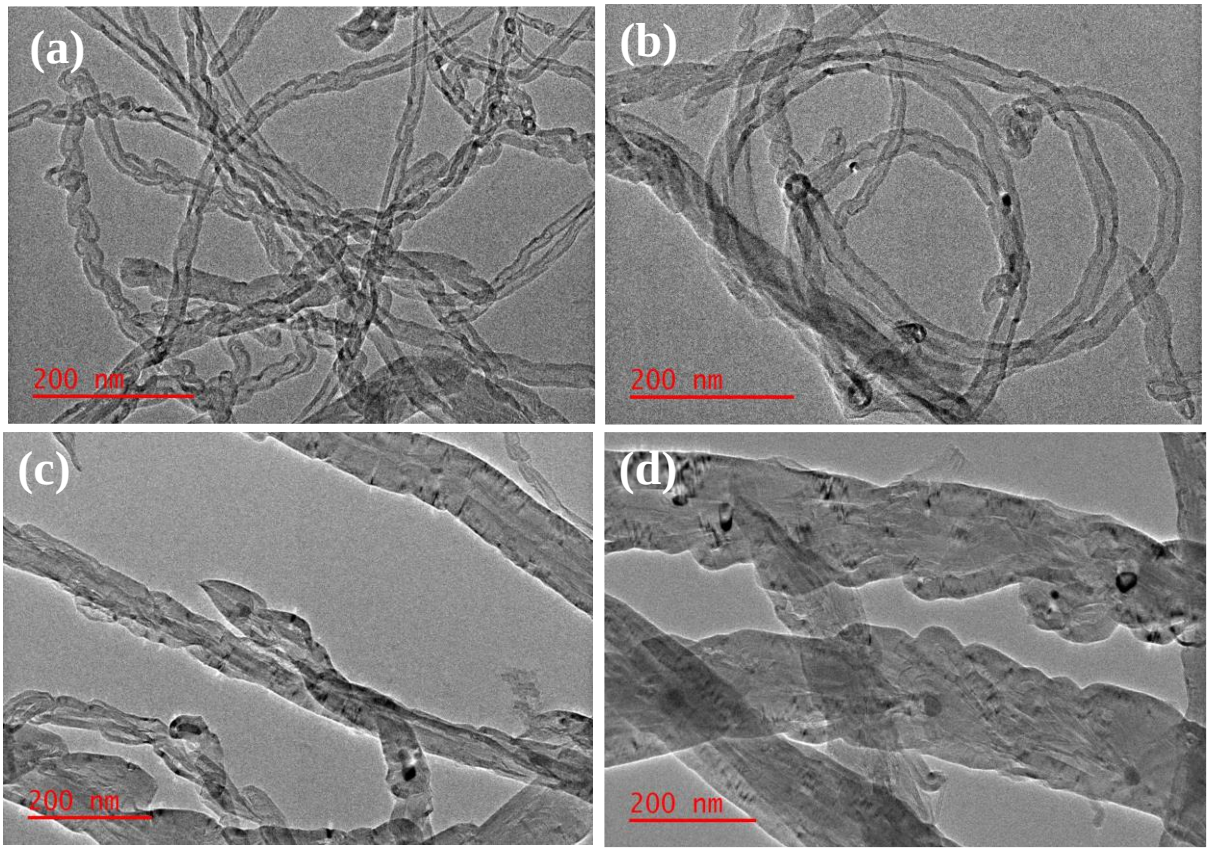

Figure 29: HRTEM images of (a) 650°C-A90, (b) 700°C-A90, (c) 750°C-A90, and (d) 800°C-A90

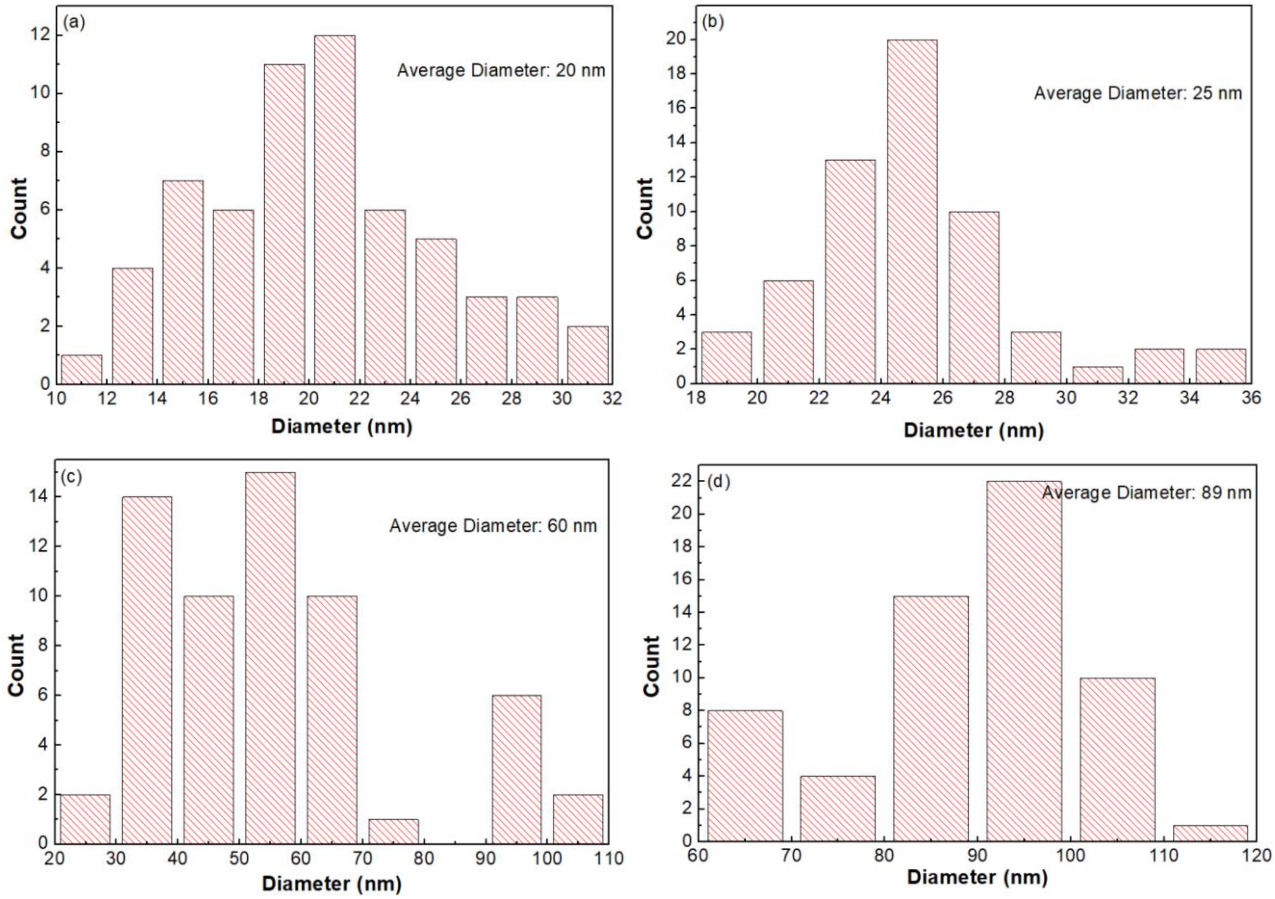

Figure 30: The diameter distribution of (a) 650°C-A90, (b) 700°C-A90, (c) 750°C-A90, and (d) 800°C-A90

The effect of ethylene flowrate (90 mL/min) at various synthesis temperatures

The effect of ethylene flowrate (90 mL/min) at various synthesis temperatures was examined using HRTEM: representative HRTEM images from the various temperatures are shown in Figure 31. A mixture of bamboo-like CNTs and spaghetti-like MWCNTs was observed in 650°C-E90 and 700°C-E90. These CNTs appeared to be structurally imperfect and contained some residual catalyst particles which were identified by the dark spots in the tube surface. Similar to what was observed in 650°C-A90 and 700°C-A90, the position in which the residual catalyst particles were located made it reasonable to assume that the tubes were formed via the base-growth mechanism as discussed in the literature review section earlier (Section 2.2.2). As the synthesis temperature was increased from 700°C to 800°C, the formation of non-tubular carbon-like nanofibers was observed as shown by 750°C-E90 in Figure 31(c), and became more pronounced in 800°C-E90 in Figure 31(d). The majority of the CNTs appeared structurally imperfect. This same trend was also

observed in samples 750°C-A90 and 800°C-A90. This further confirmed the studies by Danafar et al., (2009) about the effect of higher temperatures on the morphology of CNTs.

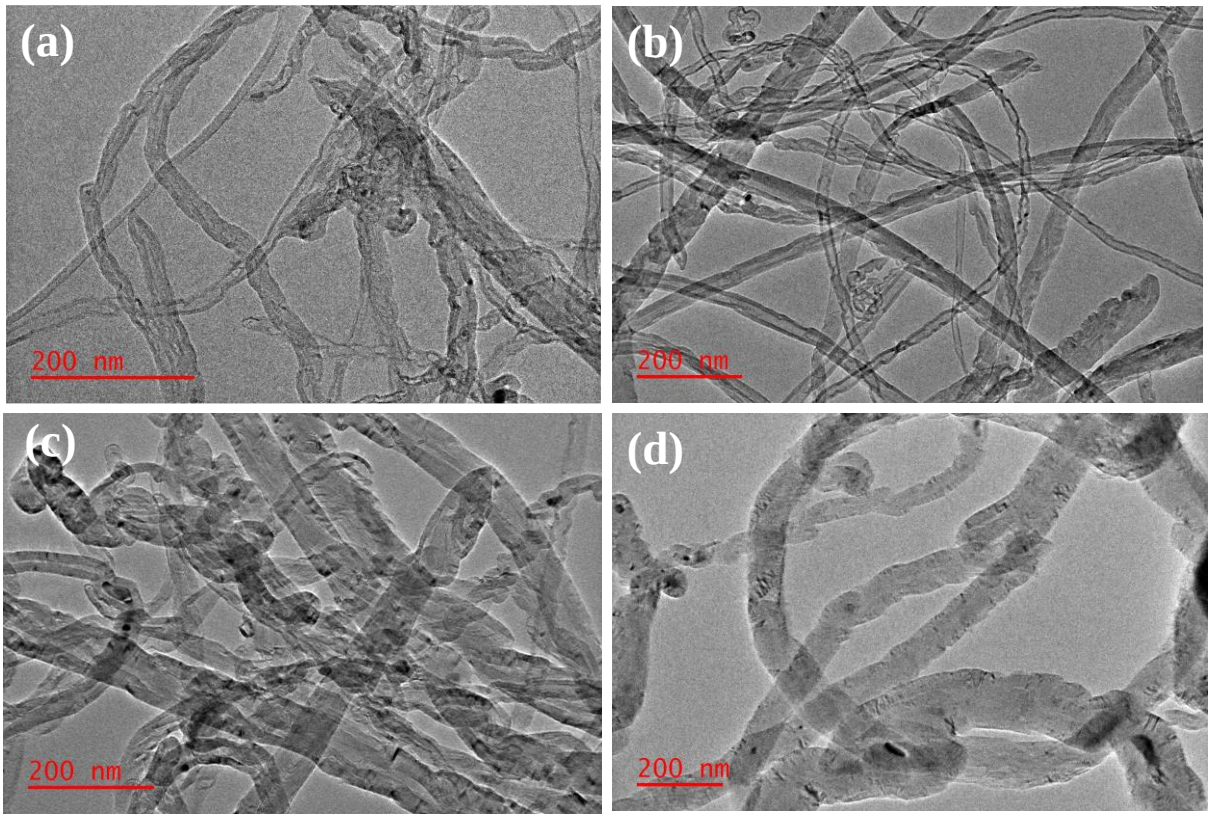

Figure 31: HRTEM images of (a) 650°C-E90, (b) 700°C-E90, (c) 750°C-E90, and (d) 800°C-E90

As shown in Figure 31, the HRTEM micrographs show a wide diameter distribution of the CNTs. Measurements of the outer diameters were done using the Image J software. The estimated average outer diameters are presented in Figure 32. The average outer diameter of the CNTs was 21 nm, 24 nm, 55 nm, and 84 nm for 650°C-E90, 700°C-E90, 750°C-E90, and 800°C-A90 respectively. A correlation between the synthesis temperature and the average outer diameter of the CNT was observed, the diameter increased with an increase in the growth temperature.

Overall, the average outer diameters of the CNTs produced from the set of tests where the ethylene was used as a hydrocarbon at a flowrate of 90 mL/min were slightly lower as compared to the tests where acetylene was used. However, for both hydrocarbons, the majority of the diameters were found to be within the nanoscale level (≤100 nm).

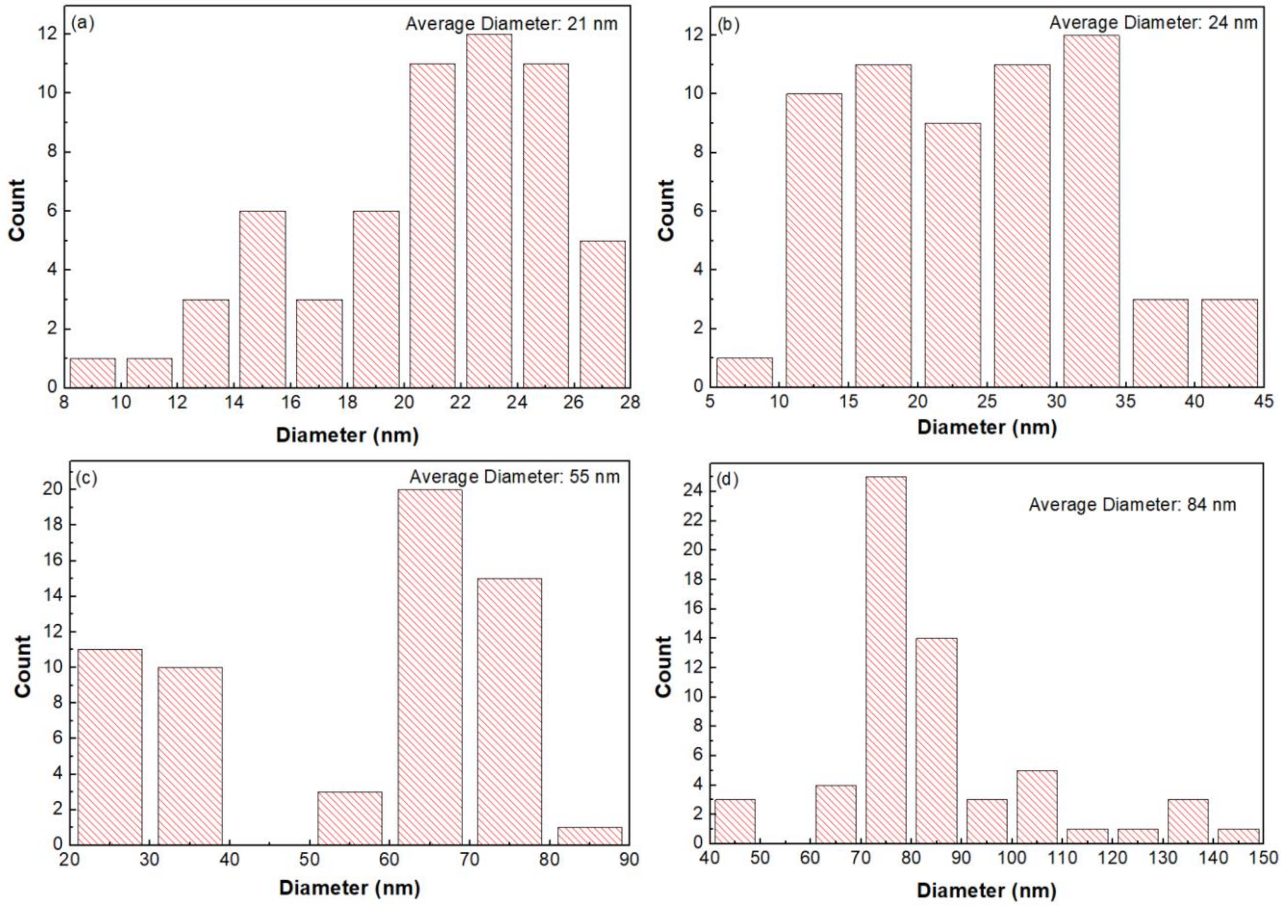

Figure 32: The diameter distribution of (a) 650°C-E90, (b) 700°C-E90, (c) 750°C-E90, and (d) 800°C-E90

The effect of acetylene flowrate (120 mL/min) at various synthesis temperatures

HRTEM was used to examine the effects of a higher acetylene flowrate (120 mL/min) on the morphology of 650°C-A120, 700°C-A120, 750°C-120A, and 800°C-A120. Representative images of these samples are presented in Figure 33. Narrow MWCNTs of varying sizes were observed on 650°C-A120 (Figure 33(a)). An increase in synthesis temperature had a major effect on the morphology of the CNTs as can be seen from Figure 33(b) to (d). The quality of the CNTs produced at temperatures above 650°C seemed to deteriorate as the formation of non-tubular carbon-like nanofibers was formed. The deterioration could be attributed to the sintering of the catalyst during synthesis as was observed by the friable lumps produced after the experiment. From the micrographs, it was observed that the walls of the tubes grew thicker as the synthesis temperature increased. In addition, dark spots which may be attributed to minor residual catalyst particles, were also observed in all the images. The position of the residual catalyst particles suggested the occurrence of the base-growth mechanism discussed in Section 2.2.2.

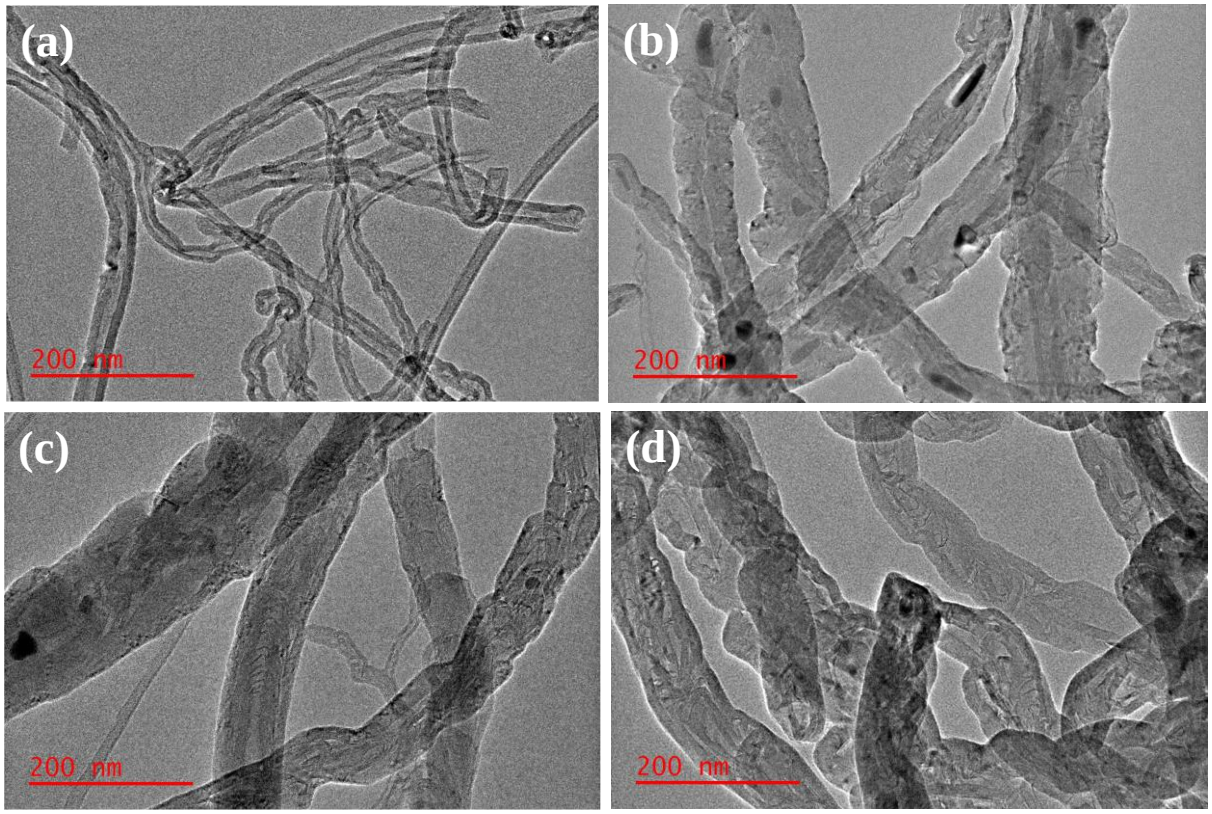

Figure 33: HRTEM images of (a) 650°C-A120, (b) 700°C-A120, (c) 750°C-A120, and (d) 800°C-A120

As depicted in Figure 34 the estimated average diameter size of the tubes of 650°C-A120, 700°C-A120, 750°C-A120, and 800°C-A120 was found to be 22 nm, 41 nm, 81 nm, and 76 nm respectively. A correlation seemed to exist between the hydrocarbon flowrate and the outer diameter of the CNTs. When the results of the samples of low acetylene flowrate (90 mL/min) were compared with the high flowrate (120 mL/min) samples, it was observed that the outer diameter was directly proportional to the acetylene flowrate for the majority of the samples. In addition, a relationship was observed between acetylene flowrate and the quality of the CNTs, the quality of the CNTs seemed to deteriorate with an increase in acetylene flowrate.

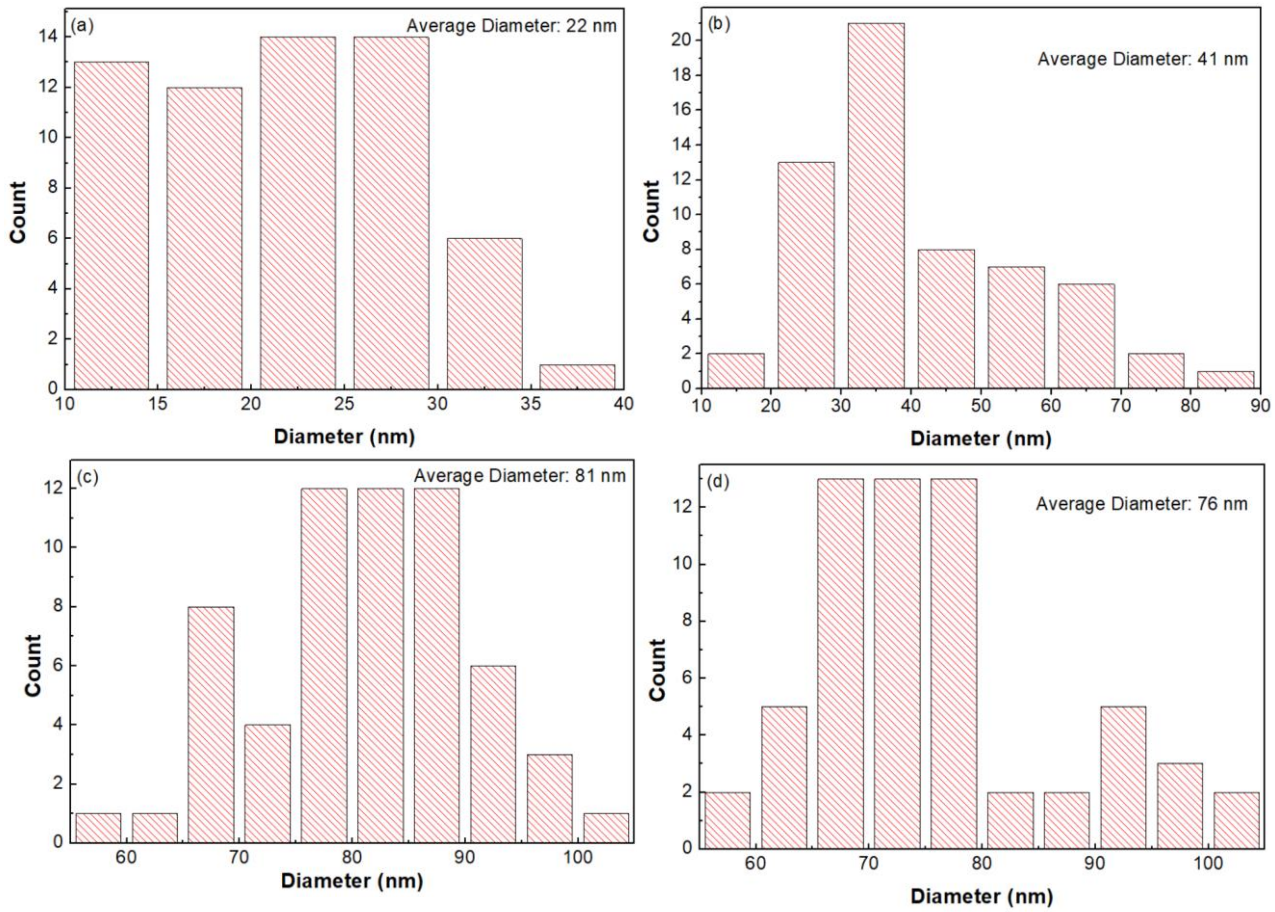

Figure 34: The diameter distribution of (a) 650°C-A120, (b) 700°C-A120, (c) 750°C-A120, and (d) 800°C-A120

The effect of ethylene flowrate (120 mL/min) at various synthesis temperatures

Figure 35 presents the HRTEM micrographs of 650°C-E120, 700°C-E120, 750°C-E120, and 800°C-E120. For 650°C-E120 and 700°C-E120, MWCNTs which were a mixture of bamboo-like and spaghetti-like nanotubes were observed. It was also observed that the quality of the CNTs deteriorated as the synthesis temperature was increased. This was confirmed by the formation of non-tubular carbon-like nanofibers which were initially observed in 700°C-E120 and became even more pronounced on 750°C-E120 and 800°C-E120 samples. The positions of the dark spots in all the HRTEM images, presumed to be residual catalyst particles, suggested the occurrence of the base-growth mechanism.

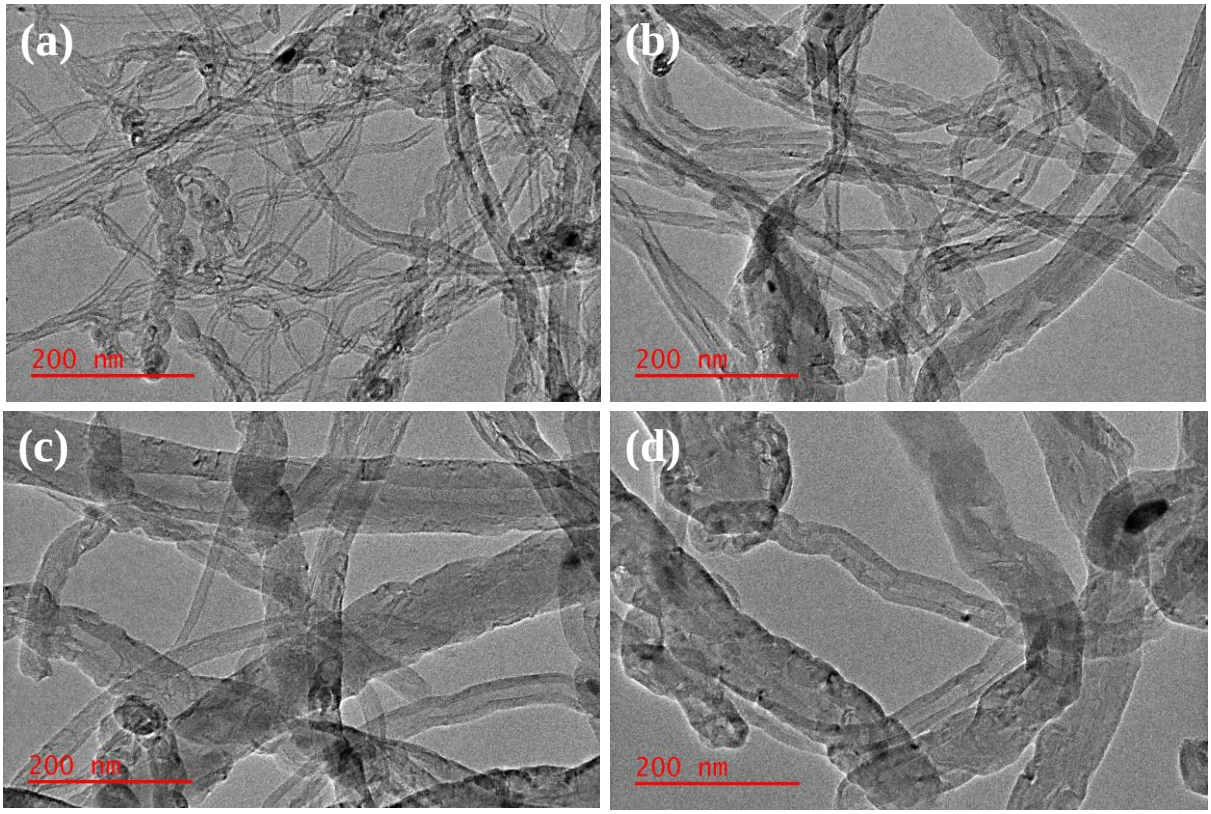

Figure 35: HRTEM images of (a) 650°C-E120, (b) 700°C-E120, (c) 750°C-E120, and (d) 800°C-E120

The outer diameter distribution histograms of the CNTs at the various growth temperatures are illustrated in Figure 36. The estimated average diameter size for 650°C-E120, 700°C-E120, 750°C-E120 and 800°C-E120 was found to be 11 nm, 20 nm, 45 nm, and 79 nm respectively. As expected, a correlation between the diameter size and the synthesis temperature was observed, the diameter size consistently increased with an increase in synthesis temperature. In addition, there seemed to be an inversely proportional relationship between the ethylene flowrate and the diameter of the MWCNTs. This relationship was noticed with the low diameter sizes (11 to 79 nm) of the samples conducted using a higher (120 mL/min) ethylene flowrate when compared to the lower (90 mL/min) ethylene flowrate samples where the average diameter ranged between 20 and 89 nm.

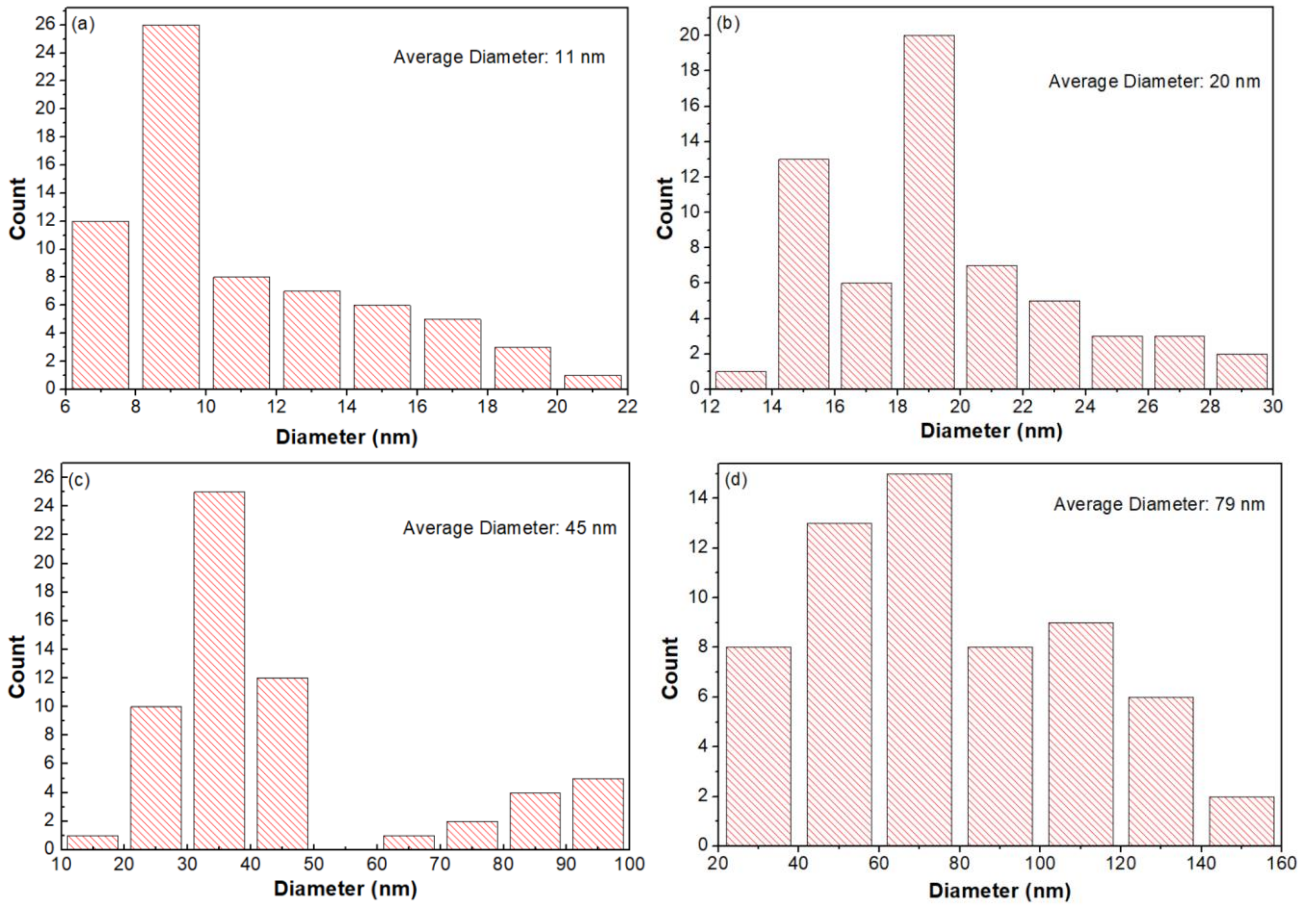

Figure 36: The diameter distribution of (a) 650°C-E120, (b) 700°C-E120, (c) 750°C-E120, and (d) 800°C-E120

4.2.2. Field emission scanning electron microscopy study

The effect of acetylene flowrate (90 mL/min) at various synthesis temperatures

FESEM was performed to further investigate the morphology of the synthesised carbon nanomaterials. Figure 37 shows the FESEM images and the corresponding EDS spectra of the various samples. The FESEM image of 650°C-A90 (Figure 37 (a)) showed bundled curled nanotubes which were heterogeneously distributed with non-uniform sizes. The size of the CNTs in the FESEM micrograph shows increasing growth as the synthesis temperature increases which is consistent with the observations made in the HRTEM images. However, the FESEM micrograph shows a disordered array of nanotubes, this could have been due to the presence of impurities such as Fe, Ca, and Co as seen from the EDS spectra. The EDS spectra showed carbon as the most prominent peak. Details of the EDS spectra at the four synthesis temperatures are presented in Table 6.

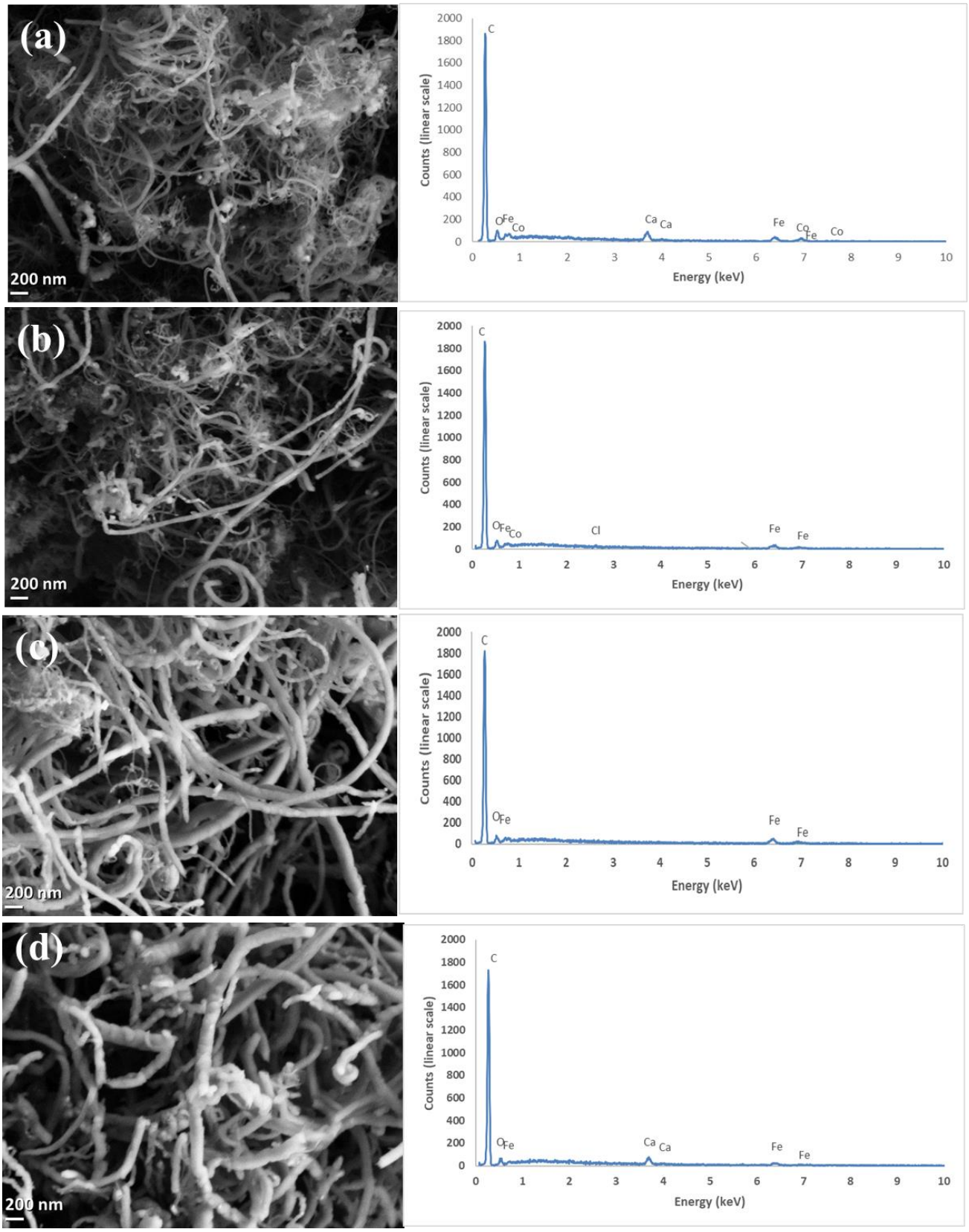

Figure 37: FESEM images and corresponding EDS spectra of (a) 650°C-A90, (b) 700°C-A90, (c) 750°C-A90 and (d) 800°C-A90

Table 6: Semi-quantitative composition of samples synthesised using acetylene (90ml/min) determined by EDS microanalysis (wt. %)

Sample	C*	O	Cl	Ca	Fe	Co	Total
650°C-A90	91.7	5.0	-	1.0	1.3	1.1	100.0
700°C-A90	95.0	3.3	0.1	-	1.1	0.5	100.0
750°C-A90	94.9	2.8	-	-	1.6	0.7	100.0
800°C-A90	96.4	2.2	-	0.7	0.7	-	100.0

*carbon composition determined by difference

The morphology of 700°C-A90 was similar to the one observed for 650°C-A90 where bundled curled nanotubes were observed. A non-uniform size distribution of CNTs was also observed. The corresponding EDS spectra also showed peaks of the residual catalyst composition (Co, O, and Fe). The carbon peak was the most prominent at this temperature. The size of the CNTs seemed to increase with an increase in synthesis temperature. This was observed on 750°C-A90 and 800°C-A90 in Figure 37 (c) and (d) respectively. The FESEM results were in agreement with the HRTEM results which showed an increase in the tubes diameter as the synthesis temperature was increased. The tubes diameter for the FESEM micrographs reported averages of 56 nm, 58 nm, 81 nm and 110 nm for 650°C-A90, 700°C-A90, 750°C-A90 and 800°C-A90 respectively. It should however be noted that FESEM is mostly interested with the surface morphology unlike HRTEM which has superior resolution and hence provides detailed images at the atomic scale, therefore for this study only the HRTEM measurements were considered for the CNTs diameters.

<u>The effect of ethylene flowrate (90 mL/min) at various synthesis temperatures</u>

The effect of ethylene at a flowrate of 90 mL/min at various synthesis temperatures was further examined by FESEM. Figure 38 shows the FESEM micrographs and their corresponding EDS spectra of the nanomaterial grown at various temperatures. From 650°C-E90, it was observed that the tubes had a tangled-curly network of CNTs. From 700°C-E90, curled-bundled CNTs with varying diameter sizes were also observed. Highly disordered CNTs were observed on 750°C-E90 (Figure 38 (c)) with some of the tubes observed to be cut or not continuous. For 800°C-E90, bundled disordered carbon nanomaterial was also observed. The tubes diameter increased as the

synthesis temperature increased, as indicated by the HRTEM results, which were consistent with the FESEM data. The tubes diameter for the FESEM micrographs reported averages of 57 nm, 75 nm, 69 nm, and 87 nm for 650℃-E90, 700℃-E90, 750℃-E90 and 800℃-E90 respectively. Overall, disordered carbon nanomaterial was observed at various synthesis temperatures which may amongst other reasons be due to the presence of impurities (Saifuddin *et al.*, 2013) such as Fe, O, and Co which were seen from the corresponding EDS spectra. As expected, the EDS spectra showed carbon as the most prominent peak. Details of the EDS spectra of the four samples are presented in Table 7.

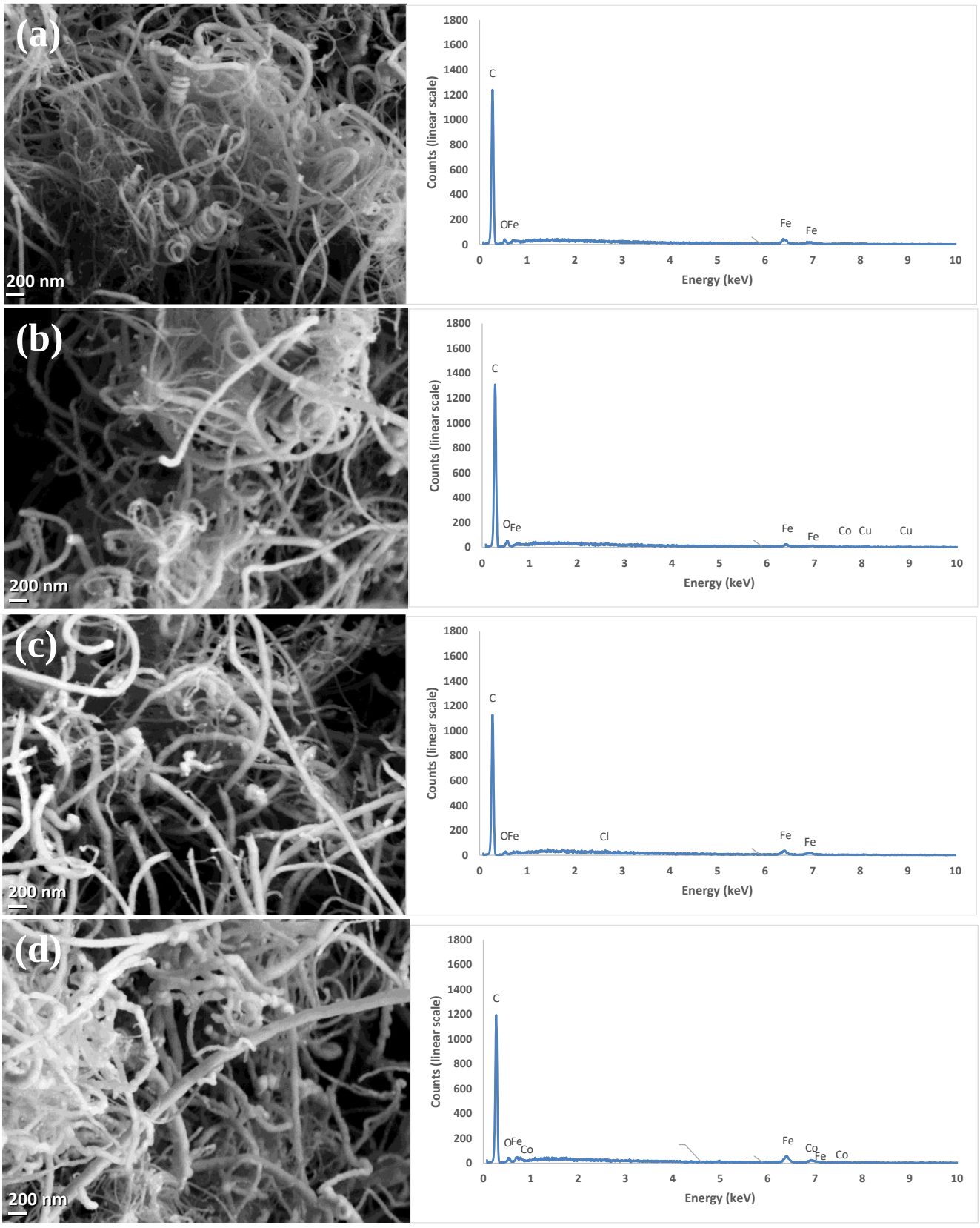

Figure 38: FESEM images and corresponding EDS spectra of a) 650°C-E90, (b) 700°C-E90, (c) 750°C-E90 and (d) 800°C-E90

Table 7: Semi-quantitative composition of samples synthesised using ethylene (90 mL/min) determined by EDS microanalysis (wt. %)

Sample	C*	O	Cl	Ca	Fe	Co	Total
650°C-E90	96.6	1.4	-	-	1.4	0.6	100.0
700°C-E90	96.0	3.0	-	-	0.7	0.4	100.0
750°C-E90	97.2	0.9	0.1	-	1.1	0.7	100.0
800°C-E90	95.8	1.4	-	-	1.9	0.9	100.0

*carbon composition determined by difference

The effect of acetylene flowrate (120 mL/min) at various synthesis temperatures

The effect of acetylene's increased flowrate on the morphology of the CNTs was further studied using FESEM. Figure 39 shows the FESEM micrographs and the corresponding EDS spectra at the various synthesis temperatures. The formation of a highly disordered mixture of CNTs and carbon nanofibers structures was observed on the samples as the synthesis temperature increased from 650°C to 800°C. From the FESEM micrographs, the diameter sizes of the carbon nanomaterials were larger (59 nm, 70 nm, 84 nm and 119 nm for 650°C-A120, 700°C-A120, 750°C-A120 and 800°C-A120 respectively) when compared to those of lower acetylene flowrate (refer to Figure 37).

The carbon peak was prominent for all the EDS spectra as shown in Figure 39. Minor peaks of Ca, Fe, and O were also observed. Details of the EDS spectra values measured in weight % for the four samples are presented in Table 8.

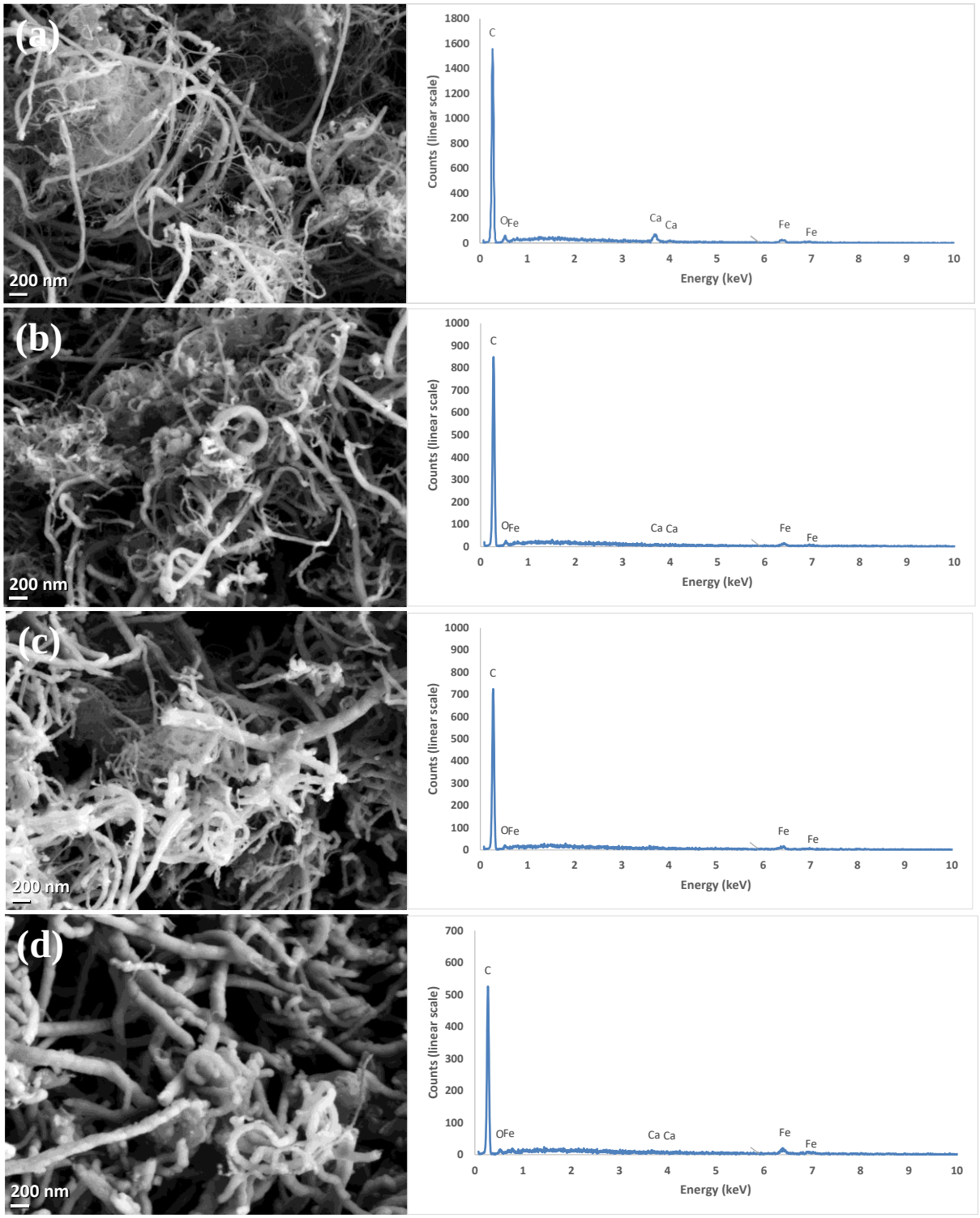

Figure 39: FESEM images and corresponding EDS spectra of (a) 650°C-A120, (b) 700°C-A120, (c) 750°C-A120 and (d) 800°C-A120

Table 8: Semi-quantitative composition of samples synthesised using acetylene (120 mL/min) determined by EDS microanalysis (wt. %)

Sample	C*	O	Cl	Ca	Fe	Co	Total
650°C-A120	96.2	2.4	-	0.7	0.8	-	100.0
700°C-A120	98.7	0.9	-	-	0.4	-	100.0
750°C-A120	98.7	0.8	-	0.02	0.4	-	100.0
800°C-A120	98.6	0.9	-	-	0.5	-	100.0

*carbon composition determined by difference

The effect of ethylene flowrate (120 mL/min) at various synthesis temperatures

Figure 40 shows the FESEM micrographs and the corresponding EDS spectra at the various synthesis temperatures. Narrow highly tangled CNTs were observed in 650°C-E120. As the synthesis temperature was increased from 650°C to 800°C, it was observed that a mixture of CNTs and what appears to be structures of carbon nanofibers were formed. The carbon nanomaterial at these temperatures was of a tangled network structure. A slight variation in the diameter size (53 nm, 67 nm, 81 nm, and 95 nm for 650°C-E120, 700°C-E120, 750°C-E120 and 800°C-E120 respectively) was noted for tests conducted at this higher ethylene flowrate when compared to the lower ethylene flowrate (90 ml/min) tests. Overall, it was observed that the quality of the carbon material deteriorated as the growth temperature increased.

From the EDS spectra, it can be seen that the carbon material contained impurities such as Fe, Co, and O. Details of the EDS analysis spectra values measured in weight % of the four samples are presented in Table 9.

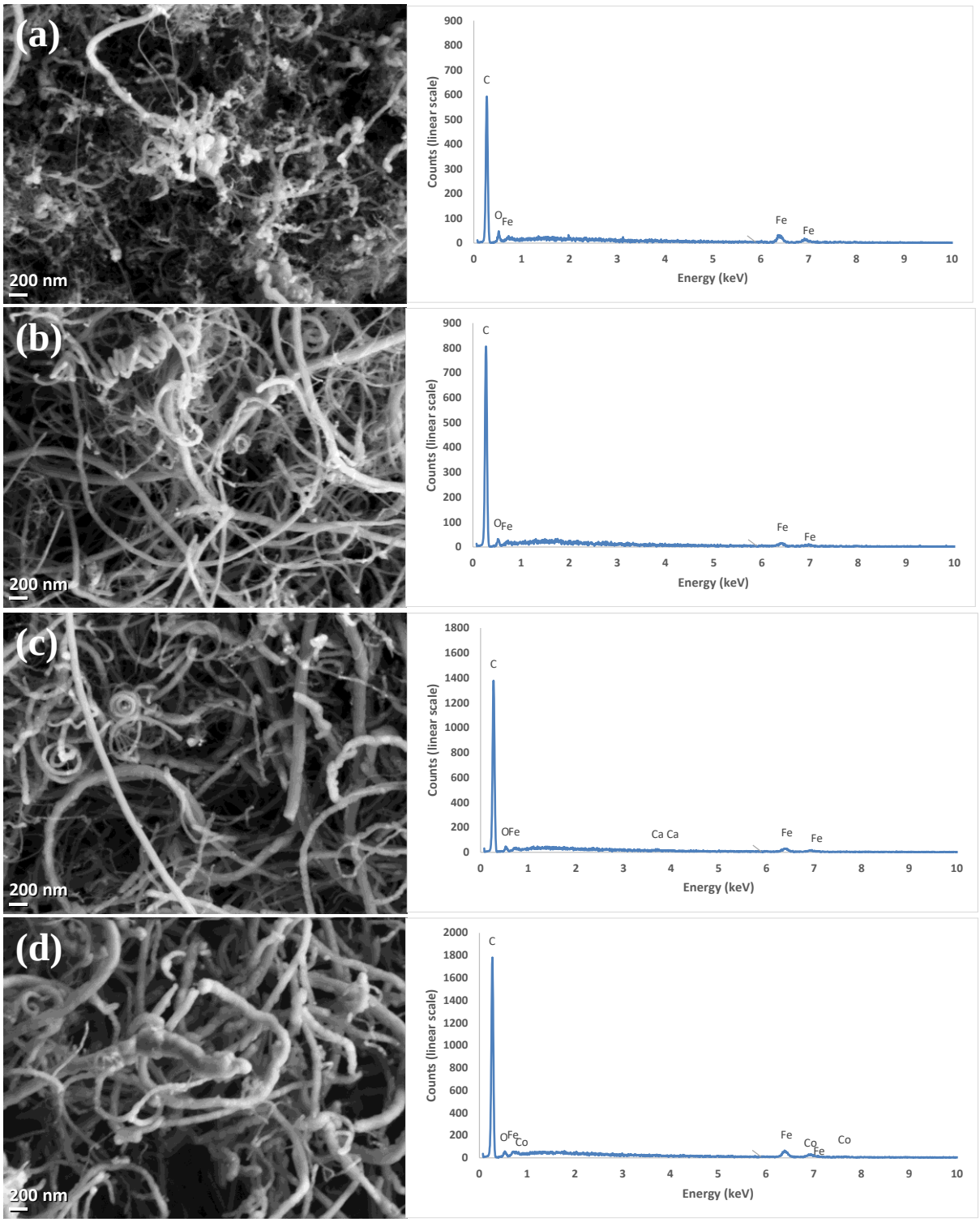

Figure 40: FESEM images and corresponding EDS spectra of (a) 650°C-E120, (b) 700°C-E120, (c) 750°C-E120 and (d) 800°C-E120

Table 9: Semi-quantitative composition of samples synthesised using ethylene (120 mL/min) determined by EDS microanalysis (wt. %)

Sample	C*	O	Cl	Ca	Fe	Co	Total
650°C-E120	96.3	2.3	-	-	0.9	0.5	100.0
700°C-E120	97.9	1.7	-	-	0.4	-	100.0
750°C-E120	97.5	1.3	-	-	0.8	0.4	100.0
800°C-E120	96.3	1.1	-	-	1.7	0.9	100.0

*Carbon composition determined by difference

4.2.3. X-ray diffraction study

The effect of acetylene flowrate (90 mL/min) at various synthesis temperatures

To further investigate the crystal structure and phase identification of the synthesised nanomaterial, XRD analysis was performed. Figure 41 shows a similar XRD pattern for all the samples with the most intense peak being that of carbon marked by an asterisk ($^{+}$). For 650°C-A90, diffraction peaks at 2θ values of 30.18°, 50.59°, and 62.45° were attributed to the (002), (100), and (004) planes of carbon respectively according to JCPDS-00-058-1638 (Keller *et al.*, 2004). Other low-intensity peaks at 52.45° and 77.46° marked with an asterisk (*) were identified and could be indexed to the (110) and (200) planes of Fe (JCPDS-00-006-0696) (Swanson *et al.*, 1968) respectively. For 700°C-A90, 2θ values of 30.22°, 50.51°, and 62.70° were attributed to the (002), (100), and (004) planes of carbon (JCPDS-00-058-1638) respectively. Other diffraction peaks that were attributed to Fe (JCPDS-00-006-0696) were identified at 52.40° and 76.07°. CNTs peaks for 750°C-A90 were located at 2θ values of 30.05°, 50.66° and 62.52° (JCPDS-00-058-1638). Fe (JCPDS-00-006-0696) peaks were further located at 52.49° and 78.81°C. For 800°C-A90, diffraction peaks ascribed to carbon were located at 2θ values of 30.18°, 50.44° and 62.89°(JCPDS-00-058-1638). Low-intensity peaks of ascribed to Fe were located at 52.16° and 77.37° (JCPDS-00-006-0696).

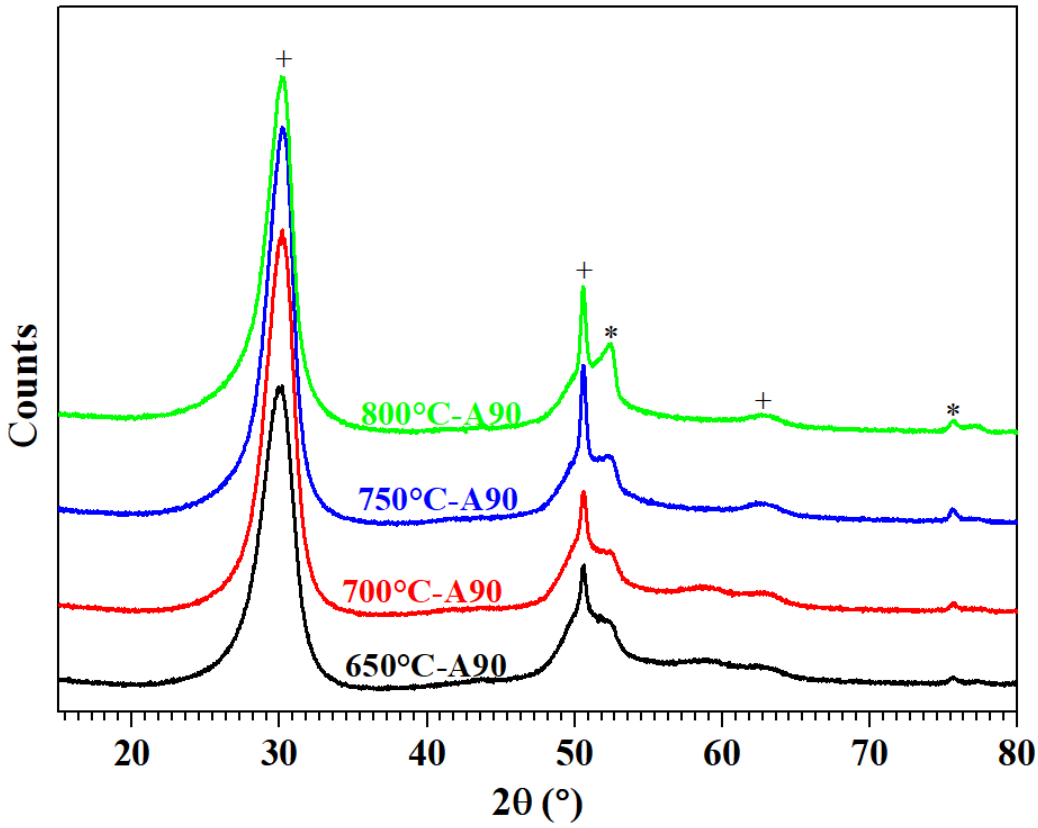

Figure 41: XRD spectra of carbon nanomaterial synthesised using acetylene at flowrate 90 mL/min

As shown in Figure 41, the less intense peaks of the XRD spectra were slightly broad and hence suggested that the carbon nanomaterial contained impurities and/or amorphous carbon (LibreTexts, 2022). This was further confirmed by the calculated crystallinity index according to Equation 4.1.

$$Crystallinity\ index\ (\%) = \frac{Area\ of\ all\ crystaline\ peaks}{Area\ of\ all\ crystalline\ and\ amorphous\ peaks} \quad (4.1)$$

The range of crystallinity is 0 percent (totally amorphous) to 100 percent (totally crystalline) (Mallard Creek Polymers, 2021). The crystallinity index at these tested parameters was in the range of 53 to 62% which is typically classified under the low crystallinity category (40% - 60%). The crystallite sizes of the carbon materials were estimated using the XRD patterns and were calculated according to the Scherrer equation expressed in Equation 4.2.

$$D = \frac{k\lambda}{\beta cos\theta} \quad (4.2)$$

Where:

- D is the crystallite size
- k is the Scherrer constant
- λ is the wavelength of the X-ray source
- β is the full width at half maxima (FWHM) of a peak in radians
- Θ peak position in radians

The average crystallite size on the tested synthesis temperatures was found to be in the range of 3.4 to 6.4 nm. This small crystallite size range was even made clear by the broadened peaks that were observed at these growth temperatures. Furthermore, literature studies have shown that as the crystallite size gets reduced, the tested material tends to lose its crystallinity and becomes more amorphous (Widjonarko, 2016).

The effect of ethylene flowrate (90 mL/min) at various synthesis temperatures

XRD diffractograms at the various growth temperatures using ethylene (90 ml/min) as a carbon source are presented in Figure 42. A similar XRD pattern for all the samples was observed with the most intense peak being that of carbon marked by an asterisk ($^{+}$). For 650°C-E90, diffraction peaks at 2θ values of 30.20°, 50.31°, and 63.35° were attributed to the (002), (100), and (004) planes of carbon respectively (JCPDS-00-058-1638) (Keller *et al.*, 2004). A low-intensity peak at 52.53° marked with an asterisk (*) was identified and could be indexed to the (110) plane of Fe (JCPDS-00-006-0696) (Swanson *et al.*, 1968). For 700°C-E90, peaks at 2θ values of 30.40°, 50.51°, and 62.85° were attributed to the (002), (100), and (004) planes of carbon respectively (JCPDS-00-058-1638). Another diffraction peak which was attributed to Fe was identified at 52.16°. Sample 750°C-E90 showed peaks at 2θ values of 30.24°, 50.51° and 62.69° corresponding to carbon (JCPDS-00-058-1638). A weak Fe peak was further located at 52.51° (JCPDS-00-006-0696). For 800°C-E90, diffraction peaks ascribed to carbon were located at 2θ values of 30.22°, 50.53°, and 62.83° (JCPDS-00-058-1638). Low-intensity peaks corresponding to Fe were located at 52.33° and 77.30° (JCPDS-00-006-0696).

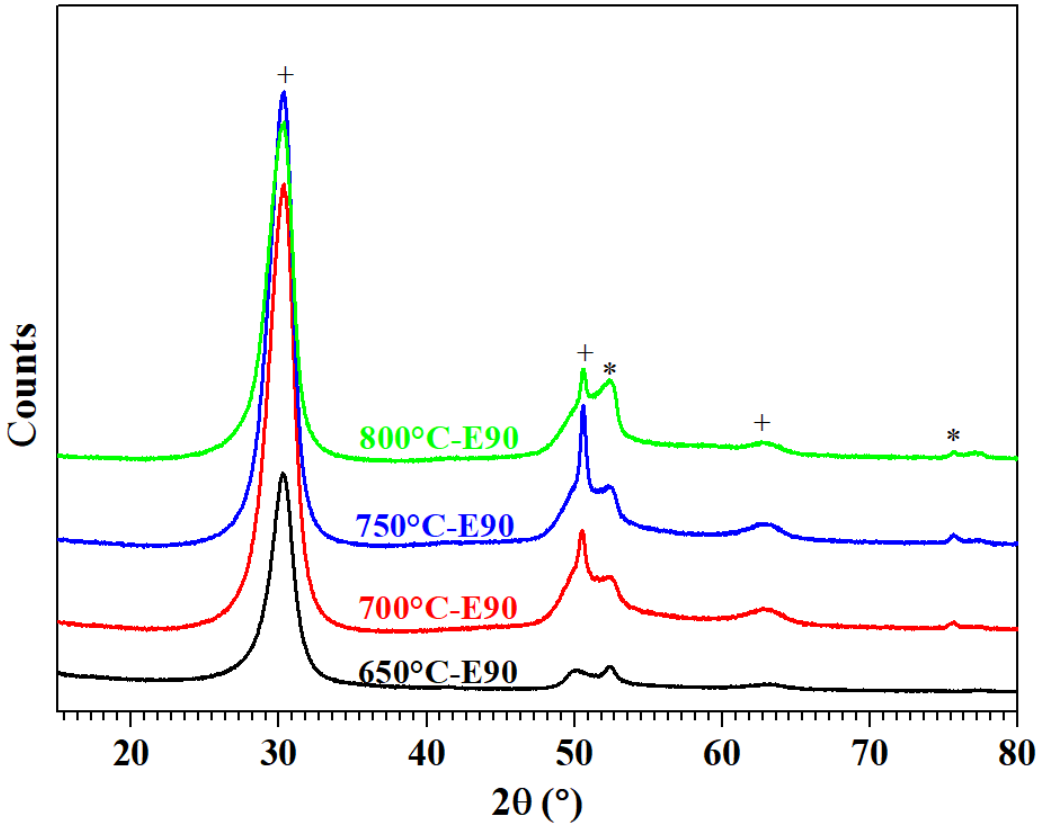

Figure 42: XRD spectra of carbon nanomaterial synthesised using ethylene at flowrate 90 mL/min

As shown in Figure 42, the less intense peaks of the XRD spectra were broad suggesting the presence of highly imperfect carbon structures (LibreTexts, 2022). This was further confirmed by the calculated crystallinity index according to Equation 4.1 which fell under the low crystallinity category and was in the range of 38 to 61%.

The crystallite sizes of the carbon materials calculated according to the Scherrer Equation 4.2 were estimated to be in the range of 3.7 to 5.7 nm. These small crystallite sizes supported the observed broadened peaks at all the tested synthesis temperatures.

<u>The effect of acetylene flowrate (120 mL/min) at various synthesis temperatures</u>

XRD diffractograms of the different samples using acetylene (120 ml/min) as a carbon source are presented in Figure 43.

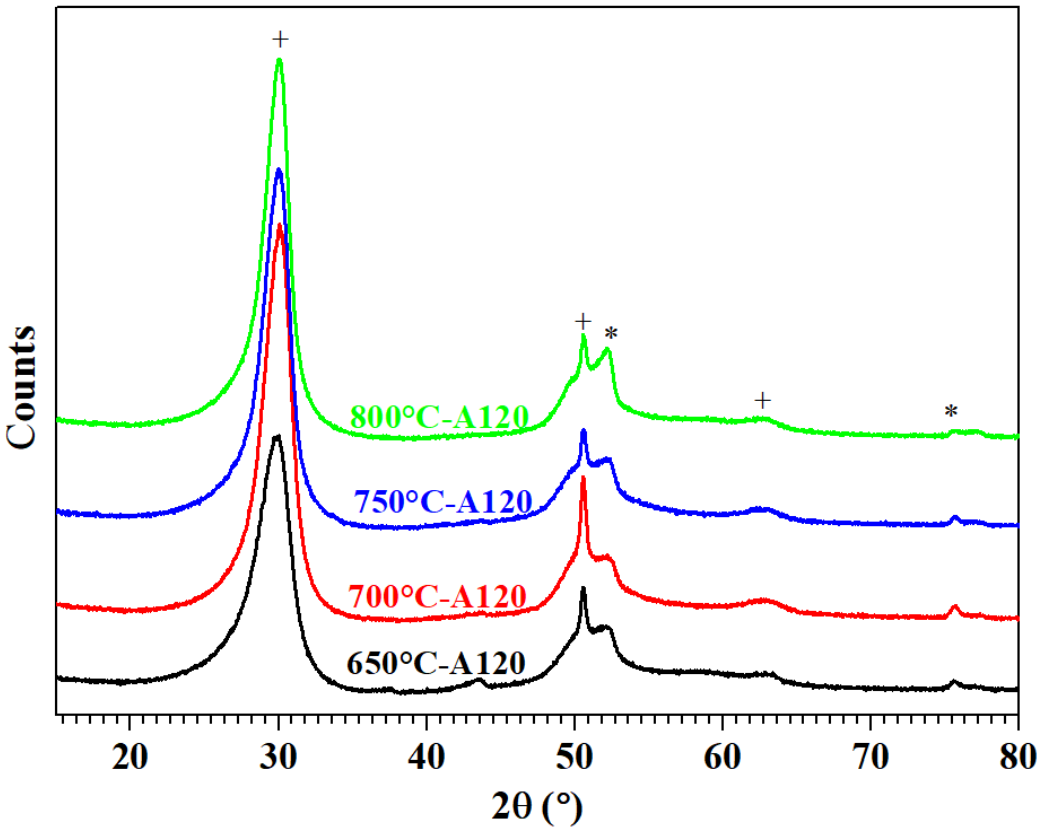

Figure 43: XRD spectra of carbon nanomaterial synthesised using acetylene at flowrate 120 mL/min

A consistent XRD pattern on all the samples was observed, with the carbon peak being the most intense and denoted by an asterisk. ($^{+}$). Diffraction peaks at 2θ values of 30.00°, 50.48°, and 62.94° shown in 650°C-A120 corresponded to the (002), (100), and (004) planes of carbon respectively (JCPDS-00-058-1638) (Keller *et al.*, 2004). Low-intensity peaks at 52.16° and 75.65° marked with an asterisk (*) were identified and could be indexed to the (110) and (200) planes of Fe respectively (JCPDS-00-006-0696) (Swanson *et al.*, 1968). For 700°C-A120, 2θ values of 30.13°, 50.66°, and 62.56° were attributed to the (002), (100), and (004) planes of carbon respectively (JCPDS-00-058-1638). Other diffraction peaks that were attributed to Fe were identified at 52.11° and 75.81° (JCPDS-00-006-0696). Peaks for 750°C-A120 located at 2θ values of 30.09°, 50.68° and 62.52° corresponded to carbon according to JCPDS-00-058-1638. Fe peaks were further located at 52.18° and 75.54° (JCPDS-00-006-0696). Diffraction peaks attributed to carbon (800°C-A120) were located at 2θ values of 30.07°, 50.70° and 62.65° (JCPDS-00-006-0696). Low-intensity peaks of Fe were located at 52.16° and 77.08° (JCPDS-00-006-0696).

The broadening of the peaks in all the tested synthesis temperatures suggested the presence of defects in the carbon crystal structure (LibreTexts, 2022). This was further confirmed by the calculated crystallinity index which was in the range of 44 to 55% suggesting an even highly amorphous carbon structure compared to the tests conducted at a lower (90 mL/min) acetylene flowrate.

The crystallite sizes of the carbon nanomaterials calculated according to the Scherrer Equation (4.2) were estimated to be in the range of 3.1 to 4.4 nm. These small crystallite sizes supported the observed broadened peaks at all the tested synthesis temperatures. A marginal variation in the crystallite size range was observed when comparing both the sets of tests conducted at the lower and higher acetylene flowrates.

The effect of ethylene flowrate (120 mL/min) at various synthesis temperatures

The effect of ethylene flowrate (120 mL/min) in the various synthesis temperatures was studied by XRD. Figure 44 shows diffractograms of various samples. A similar XRD pattern was observed for all the samples with the most intense peak being that of carbon marked by an asterisk ($^{+}$) at an average of ~30.21°. For 650°C-E120, diffraction peaks at 2θ values of 30.33°, 50.13°, and 62.91° were attributed to the (002), (100), and (004) planes of carbon respectively as according to JCPDS-00-058-1638 (Keller *et al.*, 2004). Low-intensity peaks at 52.49° and 77.19° marked with an asterisk (*) were identified and could be indexed to the (110) and (200) planes of Fe (JCPDS-00-006-0696) (Swanson *et al.*, 1968) respectively.

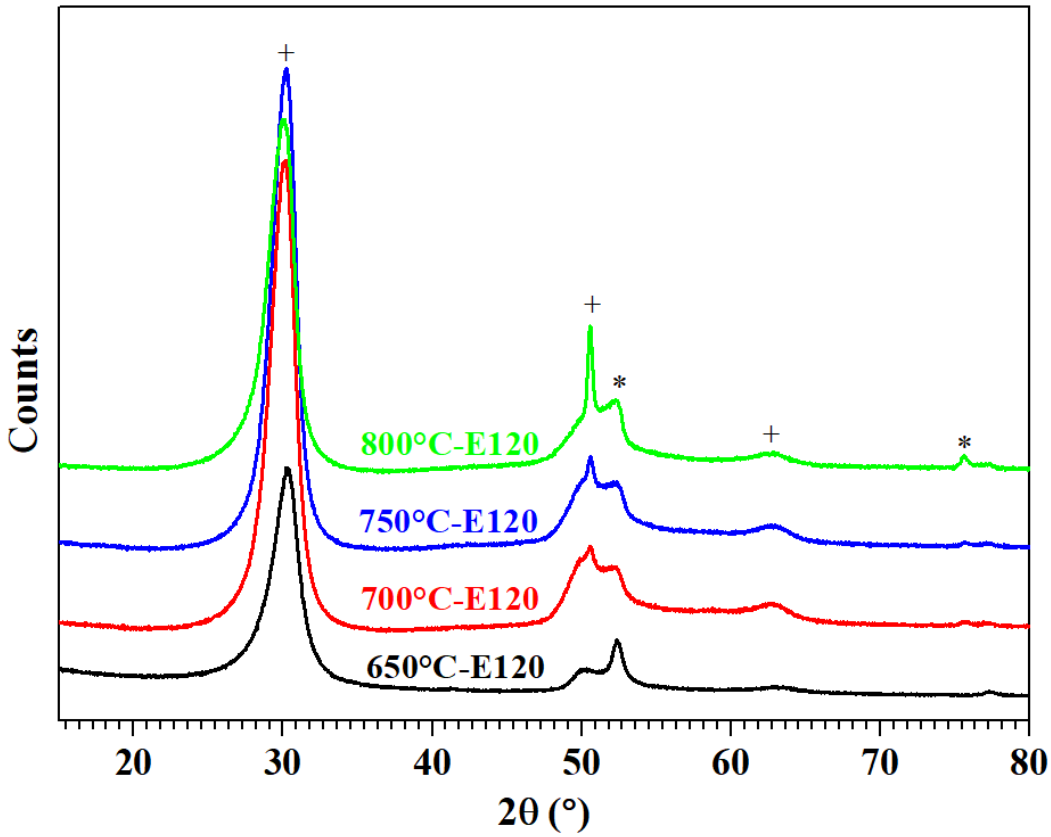

Figure 44: XRD spectra of carbon material synthesised using ethylene at flowrate 120 mL/min

Peaks observed in 700°C-E120 at 2θ values of 30.16°, 50.62°, and 62.34° were according to JCPDS-00-058-1638 attributed to the (002), (100), and (004) planes of carbon respectively. Other diffraction peaks that were attributed to Fe were identified at 52.20° and 77.39° (JCPDS-00-006-0696). Carbon peaks for 750°C-E120 were located at 2θ values of 30.29°, 50.51° and 62.61°C (JCPDS-00-058-1638). Fe peaks were further located at 52.20° and 75.54° (JCPDS-00-006-0696). Diffraction peaks ascribed to carbon were located at 2θ values of 30.07°C, 50.66°C and 62.41°C (JCPDS-00-058-1638) for 800°C-E120. Low-intensity peaks of Fe were located at 52.44° and 77.02° (JCPDS-00-006-0696).

The crystallinity index was in the range of 47 to 73% which was slightly higher than that of the set of tests that were conducted using a lower (90 mL/min) ethylene flowrate. Using the Scherrer Equation (2), the crystallite size was found to vary between 3.6 and 6.5 nm.

4.2.4. Raman Spectroscopy

Raman is one of the powerful tools used in the analysis of carbon-based materials. In this study, it was used in the characterisation of CNTs quality as well as in the determination of the type (SWCNT or MWCNT) of CNTs in terms of layers that were formed. The main features in Raman spectra of CNTs are the G band and the D band (Dresselhaus *et al.*, 2005). The G band relates to well-ordered graphitic structures. The D band which is also known as the disorder band is normally related to the presence of defects, and structural imperfections in the carbon materials. The 2D band which is the overtone of the D band corresponds to the two-phonon scattering (Kuznetsov *et al.*, 2014). For graphenes and nanotubes, particularly MWCNT, the typical positions of the D, G, and 2D bands in a Raman spectrum are ~1300-1400 cm^{-1}, ~1580 cm^{-1}, and ~2500-2800 cm^{-1} respectively (Dresselhaus *et al.*, 2010) (Bradley *et al.*, 2012). The ratio of the intensity of D and G is used as a semi-quantitative parameter to characterise the quality of nanomaterial. Equal intensities of D and G (i.e. where I_D/I_G =1) indicate high-quality structural defects or the presence of amorphous carbon (Costa *et al.*, 2008). In simplest terms when I_D/I_G >1 it means that the material is highly defective and conversely when I_D/I_G < 1 the material is less defective. Therefore, ideally the I_D/I_G ratio should be as low as possible for a highly crystalline material.

<u>The effect of acetylene flowrate (90 mL/min) at various synthesis temperatures</u>

The Raman spectra of the CNTs produced with acetylene (90 mL/min) pyrolysis at different temperatures are presented in Figure 45. Three major peaks that could be ascribed to MWCNTs were observed in the Raman spectra: the D band, G band, and their overtones termed the 2D band. The Raman spectra in all four samples were almost identical and there were bands at about 1349 cm^{-1}, 1584 cm^{-1}, and 2691 cm^{-1} for D, G, and 2D respectively (see Table 10). The intensity ratio I_D/I_G (graphically represented by the inset in Figure 45) reported 0.85, 0.83, 0.63, and 0.78 for 650°C-A90, 700°C-A90, 750°C-A90 and 800°C-A90 respectively. These high intensity ratios were supported by the broadened peaks observed in the XRD spectra of these samples in Figure 41 of Section 4.2.3. There was however no clear trend in the intensity ratio as the synthesis temperature was increased. The intensity ratio of sample 700°C-A90 was found to be slightly higher when compared to that obtained by (Mhlanga *et al.*, 2009) who reported ~0.7 at the similar test conditions used in this study. The Raman spectra of these tests confirmed the presence of only MWCNTs since no radial breathing modes (RBMs) were observed at between 150 cm^{-1} and 300 cm^{-1} and no split in the G band which are characteristics of SWCNTs (Dresselhaus *et al.*, 2007).

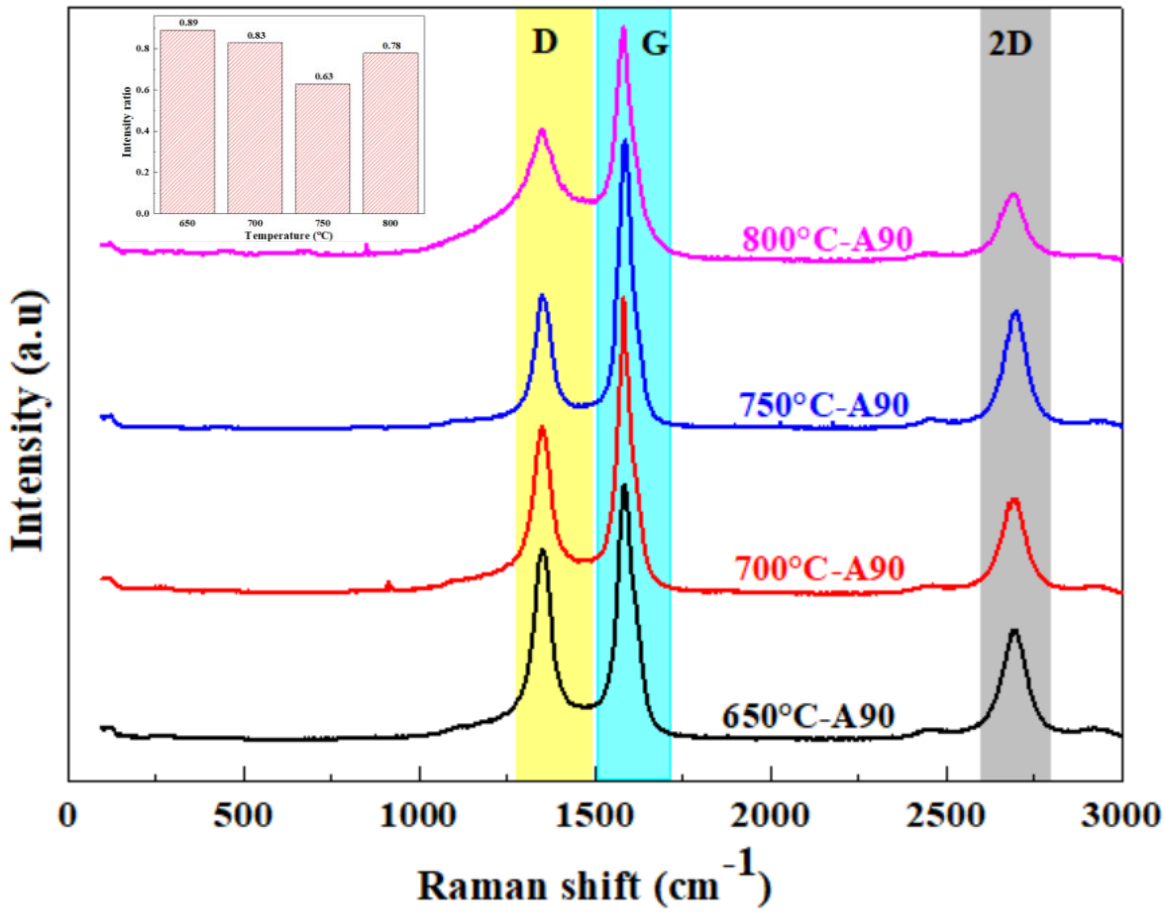

Figure 45: Raman spectra of carbon nanomaterial synthesised using acetylene at flowrate 90 mL/min (Inset: I_D/I_G ratio of carbon nanomaterial)

Table 10: Characteristic parameters of Raman spectra for samples synthesised using acetylene at flowrate 90 mL/min

Sample	D band position (cm^{-1})	G band position (cm^{-1})	2D band position (cm^{-1})	I_D/I_G Ratio
650°C-A90	1349	1586	2686	0.89
700°C-A90	1349	1582	2686	0.83
750°C-A90	1349	1586	2700	0.63
800°C-A90	1349	1582	2693	0.78

The effect of ethylene flowrate (90 mL/min) at various synthesis temperatures

The Raman spectra of the CNTs produced using ethylene (90:240 C_2H_4:N_2 flow) at different synthesis temperatures are presented in Figure 46. Similar to the tests conducted using acetylene (90 mL/min) as a hydrocarbon, three prominent peaks with intensity maxima were displayed. The Raman spectra of the different samples were almost identical, with the D, G, and 2D bands positioned at averages of 1348 cm^{-1}, 1580 $cm^{-1,}$ and 2688 cm^{-1} respectively. The characteristic parameters of the Raman spectra of the four samples are presented in Table 11. The intensity ratio I_D/I_G varied from 0.62 to 0.81 for the tested samples. These high-intensity ratios indicated the presence of amorphous carbon and/or defective nanotubes which was also confirmed by the broadened XRD peaks in Figure 42 of Section 4.2.3. The variation in the intensity ratio between the different synthesis temperatures was marginal, however, 750°C-E90 reported the smallest (0.62) I_D/I_G. The Raman spectra of these tests also confirmed the presence of only MWCNTs since no RBMs and G split were observed (Dresselhaus *et al.*, 2007).

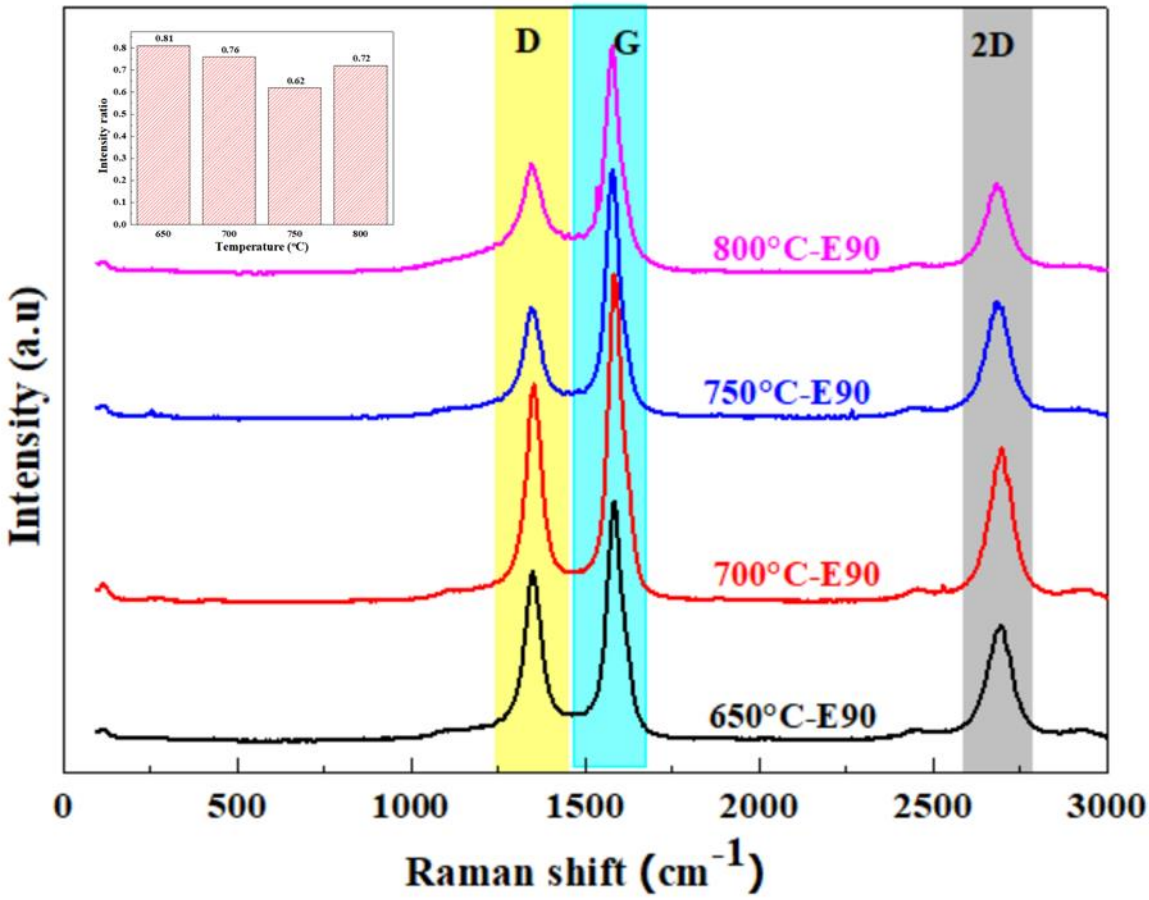

Figure 46: Raman spectra of carbon nanomaterial synthesised using ethylene at flowrate 90 mL/min (Inset: I_D/I_G ratio of carbon nanomaterial)

Table 11: Characteristic parameters of Raman spectra for samples synthesised using ethylene at flowrate 90 mL/min

Sample	D band position (cm^{-1})	G band position (cm^{-1})	2D band position (cm^{-1})	I_D/I_G Ratio
650°C-E90	1349	1582	2693	0.81
700°C-E90	1353	1582	2697	0.76
750°C-E90	1345	1578	2683	0.62
800°C-E90	1345	1578	2679	0.72

The effect of acetylene flowrate (120 mL/min) at various synthesis temperatures

Raman analysis on tests conducted to evaluate the effect of hydrocarbon flowrate was also conducted. The Raman spectra of the CNTs produced using acetylene (120:240 C_2H_2:N_2 flow) as a carbon precursor at different temperatures are presented in Figure 47. As can be seen from the Raman spectra, a higher acetylene flowrate did not have a major effect on the positioning of the three prominent peaks, however, a slight variation in the intensity of the 2D bands was observed when compared with the lower acetylene flowrate samples (650°C-A90, 700°C-A90, 750°C-A90 and 800°C-A90). The D, G, and 2D peaks are at approximately the same positions namely, 1347 cm^{-1}, 1582 $cm^{-1,}$ and 2686 cm^{-1} respectively. The characteristic parameters of the Raman spectra of samples are presented in Table 12. The intensity ratio I_D/I_G reported 1.14, 0.89, 0.86, and 0.95 for 650°C-A120, 700°C-A120, 750°C-A120 and 800°C-A120 respectively. These intensity ratios were found to be slightly higher than those of the tests where a lower acetylene flowrate was used. The high intensity ratios at this flowrate meant that the disorders in the carbon nanomaterial was excessive when compared to those of the lower acetylene flowrate. This was supported by the low calculated crystallinity index reported under the XRD study (Section 4.2.3) which ranged between 42 to 55% as compared to 53 to 62% reported for the lower flowrate samples. The Raman spectra of these tests also confirmed the presence of only MWCNTs since no RBMs and G split were observed (Dresselhaus *et al.*, 2007).

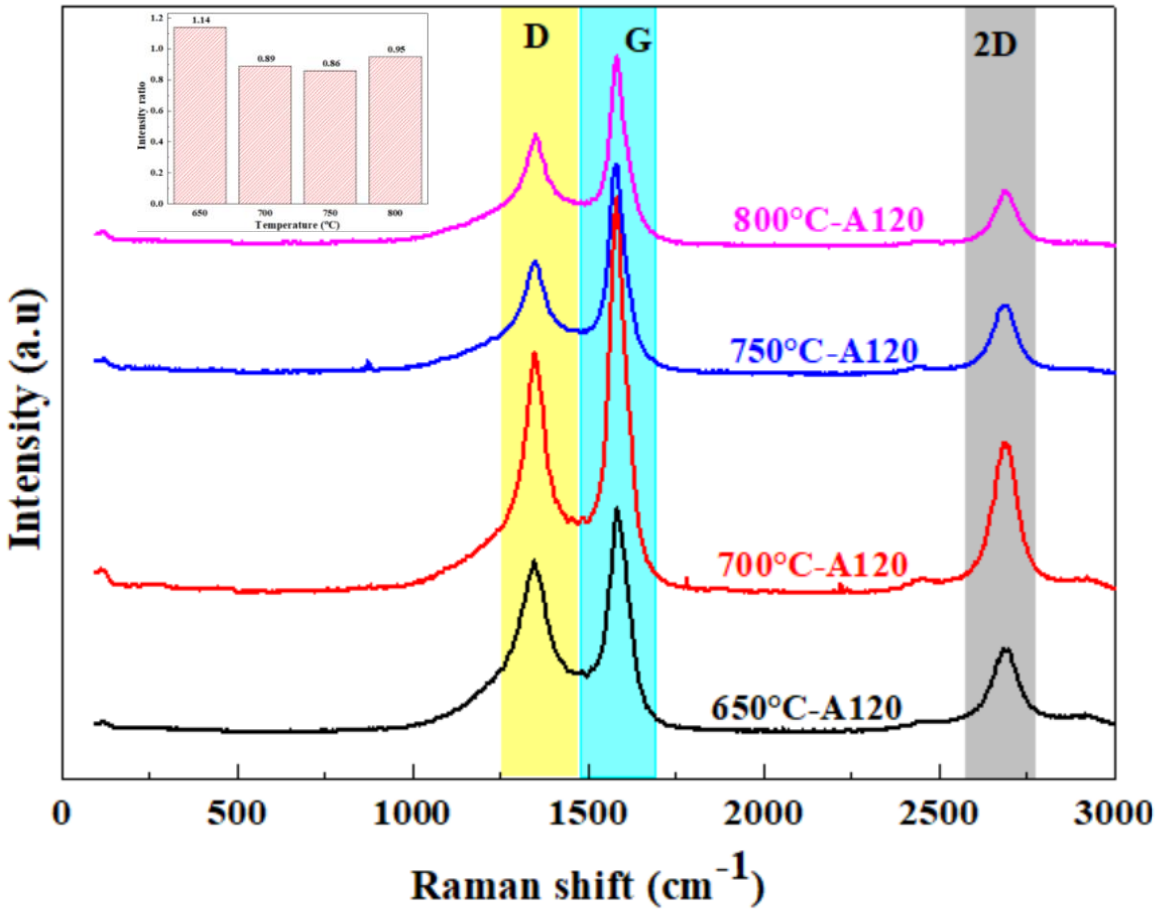

Figure 47: Raman spectra of carbon nanomaterial synthesised using acetylene at flowrate 120 mL/min (Inset: I_D/I_G ratio of carbon nanomaterial)

Table 12: Characteristic parameters of Raman spectra for samples synthesised using acetylene at flowrate 120 mL/min

Sample	D band position (cm^{-1})	G band position (cm^{-1})	2D band position (cm^{-1})	I_D/I_G Ratio
650°C-A120	1345	1582	2683	1.14
700°C-A120	1345	1582	2686	0.89
750°C-A120	1349	1582	2693	0.86
800°C-A120	1349	1582	2683	0.95

The effect of ethylene flowrate (120 mL/min) at various synthesis temperatures

The Raman spectra of the CNTs produced using ethylene (120:240 C_2H_4-N_2 flow) as a carbon precursor at different temperatures are presented in Figure 48. The position of the major peaks was almost identical in all the various temperatures. The D, G, and 2D peaks which could be attributed to the bands of MWCNTs were positioned at averages of about 1350 cm^{-1}, 1582 $cm^{-1,}$ and 2688 cm^{-1} respectively.

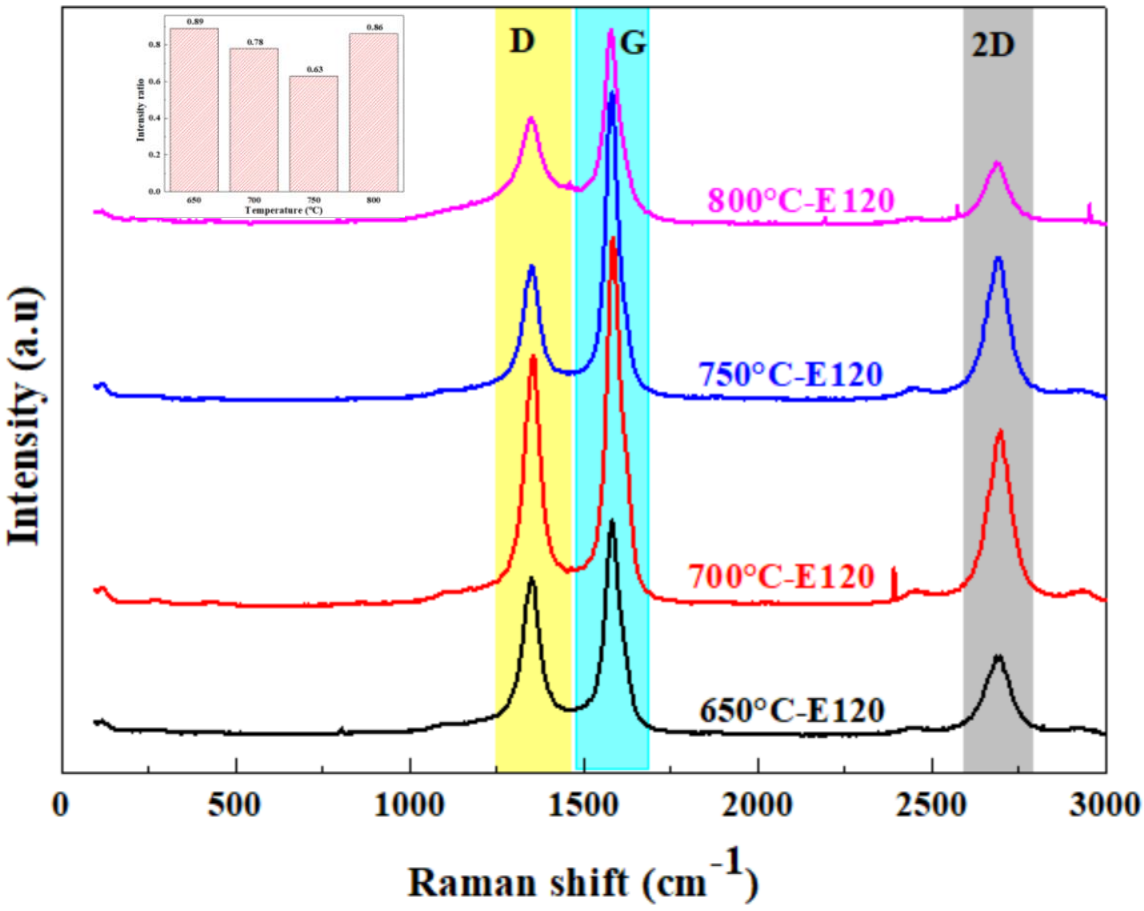

Figure 48: Raman spectra of carbon nanomaterial synthesised using ethylene at flowrate 120 mL/min (Inset: I_D/I_G ratio of carbon nanomaterial)

The characteristic parameters of the Raman spectra of the four samples are presented in Table 13. For 650°C-E120, 700°C-E120, 750°C-E120 and 800°C-E120, the intensity ratio I_D/I_G reported values of 0.89, 0.78, 0.63, and 0.86, respectively. These intensity ratios were found to be slightly higher compared to those of the tests carried out with a lower ethylene flowrate. The high intensity ratios at this flowrate meant that the disorders in the carbon nanomaterial was higher when

compared to those of the lower ethylene flowrate. The disorderliness in the carbon nanomaterial was supported by the broadened peaks reported on the XRD results (Section 4.2.3) in this study. The Raman spectra of these tests also confirmed the presence of only MWCNTs since no RBMs and G split were observed.

Table 13: Characteristic parameters of Raman spectra for samples synthesised using ethylene at flowrate 120 mL/min

Sample	**D band position (cm^{-1})**	**G band position (cm^{-1})**	**2D band position (cm^{-1})**	**I_D/I_G Ratio**
650°C-E120	1349	1582	2686	0.89
700°C-E120	1353	1586	2697	0.78
750°C-E120	1349	1582	2686	0.63
800°C-E120	1349	1578	2683	0.86

4.2.5. BET Surface area analysis

The specific surface area (SSA), pore size, and volume distribution of the samples from the various synthesis temperatures were studied using the BET gas adsorption/desorption method. Studies (Peigney *et al.*, 2001), (Chakraborty *et al.*, 2006),(Birch *et al.*, 2013) have shown that the surface area of CNTs could be affected by the following properties:

- Number of walls
- Tube diameter
- Material defects
- Tube bundling
- Surface functionalisation and
- Metal and amorphous carbon impurities

<u>The effect of acetylene flowrate (90 mL/min) at various synthesis temperatures</u>

The surface area measurements for samples where 90 mL/min acetylene was used as a hydrocarbon gas are presented in Table 14. The SSA was ~77, ~65, ~41, and ~33 m^2/g respectively for 650°C-A90, 700°C-A90, 750°C-A90, and 800°C-A90. The decrease in the SSA could be

attributed to the increase in outer diameter (Chen *et al.*, 2007) of the MWCNTs as the synthesis temperature was increased as seen in the HRTEM results in Figure 30 of Section 4.2.1. A study by Chen *et al.* (2007) has shown that metal and amorphous carbon impurities decrease the SSA partly as a result of the lack of surface accessibility of nitrogen adsorption. Therefore, another reason for the decrease in the SSA may be the the amorphous carbon impurities that was observed via the broadening of the XRD peaks as seen in Figure 41 of Section 4.2.3. The decrease in the SSA observed, was similar to studies by Peigney *et al.* (2001) and Chen *et al.* (2007) where they found that the SSA was inversely proportional to the outer diameter of the CNTs. The pore size for all the samples was ~2 nm. A decrease in the pore volume was observed as the synthesis temperature increased. The possible reason for the decrease in the pore volume could be pore blockage from impurities (eg amorphous carbon) as the synthesis temperature was increased which was evidenced by the non-tubular images in the HRTEM results (Birch *et al.*, 2013).

Table 14: BET surface area data for samples synthesised using acetylene at flowrate 90 mL/min

Sample	**Surface area (m^2/g)**	**Pore size (nm)**	**Pore volume (cm^3/g)**
650°C-A90	76.98	2.00	0.52
700°C-A90	64.93	2.01	0.44
750°C-A90	41.13	2.00	0.28
800°C-A90	32.98	1.97	0.22

The effect of ethylene flowrate (90 mL/min) at various synthesis temperatures

Surface area analysis where 90 mL/min ethylene was used as a hydrocarbon gas is presented in Table 15. The SSA for 650°C-E90, 700°C-E90, 750°C-90, and 800°C-E90 was ~63, ~66, ~49, and ~40 m^2/g. A relationship was observed between the SSA of the samples and the synthesis temperature, the SSA of the carbon nanomaterial decreased with an increase in the synthesis temperature except for 700°C-E90 which might be due to an experimental error. The average pore size was ~2 nm. The pore volume ranged between 0.27 and 0.43 cm^3/g.

Table 15: BET surface area data for samples synthesised using ethylene at flowrate 90 mL/min

Sample	Surface area (m^2/g)	Pore size (nm)	Pore volume (cm^3/g)
650°C-E90	63.29	2.00	0.43
700°C-E90	65.92	2.03	0.45
750°C-E90	48.76	2.02	0.33
800°C-E90	40.34	2.01	0.27

The effect of acetylene flowrate (120 mL/min) at various synthesis temperatures

Further BET analysis on samples where 120 mL/min acetylene was used as a hydrocarbon gas is presented in Table 16. The increased hydrocarbon flowrate had an impact on the SSA as an increment in the SSA was observed when compared to the lower (90 mL/min) flowrate samples. The SSA reported ~97, ~67, ~62, and ~36 m^2/g for 650°C-A120, 700°C-A120, 750°C-A120 and 800°C-A120 respectively. Once again, this lowering of the SSA may be attributed to the presence of amorphous carbon impurities and the increase in outer diameter as a result of the increase in synthesis temperature (Peigney *et al.*, 2001)(Chen *et al.*, 2007). The presence of amorphous carbon material at these conditions was further confirmed by the high I_D/I_G ratio (Table 12 of Section 4.2.4) of these samples when compared to those of a low acetylene flowrate. The pore size varied between 6 to 15 nm. In energy storage, porous materials are widely used mostly for electrodes and therefore pore size plays a major role in the electrolyte access to the electrode surface (Vu *et al.*, 2012). The high SSA will further play a role in facilitating charge transfer across the electrode/electrolyte interface during electrochemical testing (Vu *et al.*, 2012).

Table 16: BET surface area data for samples synthesised using acetylene at flowrate 120 mL/min

Sample	Surface area (m^2/g)	Pore size (nm)	Pore volume (cm^3/g)
650°C-A120	96.70	6.72	0.60
700°C-A120	67.12	6.65	1.51
750°C-A120	62.37	15.24	3.22
800°C-A120	35.88	8.38	1.02

The effect of ethylene flowrate (120 mL/min) at various synthesis temperatures

Surface area measurements on samples where 120 mL/min of ethylene was used as a hydrocarbon gas are presented in Table 17. The SSA of the samples follows the order 800°C-E120<750°C-E120<700°C-E120<650°C-E120. Samples of 650°C-E120 and 700°C-E120 reported the highest SSA when compared to the low flowrate samples (650°C-E90 and 700°C-E90) which reported 63 and 66 m^2/g respectively. The pore size was high and ranged between 3 and 12 nm.

Table 17: BET surface area data for samples synthesised using ethylene at flowrate 120 mL/min

Sample	Surface area (m^2/g)	Pore size (nm)	Pore volume (cm^3/g)
650°C-E120	143.93	9.56	1.27
700°C-E120	80.15	12.06	3.27
750°C-E120	35.93	7.70	0.94
800°C-E120	30.88	3.31	1.27

According to the literature, the commonly reported SSA values for MWCNTs range from ~15 to 300 m^2/g (Birch *et al.*, 2013). The SSA reported in this study (31 to 144 m^2/g) also falls within the same range.

4.2.6. A brief overview of CNTs' characterisation

A summary of the characterisation results of the carbon nanomaterial synthesised in this study is provided in Table 18.

Table 18: Summary of characterization results of carbon nanomaterial

Sample	**HRTEM**	**XRD**		**Raman**	**BET**	
	d_{HRTEM} (nm)	**Cristanillity index (%)**	**Crytallite size (nm)**	**I_D/I_G**	**SSA (m^2/g)**	**Pore volume (cm^3/g)**
650°C-A90	20	56	3.4	0.89	77	0.52
700°C-A90	25	62	3.5	0.83	65	0.44
750°C-A90	60	55	3.7	0.63	41	0.28
800°C-A90	89	53	6.4	0.78	33	0.22
650°C-E90	21	38	5.7	0.81	63	0.43
700°C-E90	24	47	3.7	0.76	66	0.45
750°C-E90	55	57	4.0	0.62	49	0.33
800°C-E90	84	61	4.5	0.72	40	0.27
650°C-A120	22	51	4.4	1.14	97	0.60
700°C-A120	41	44	3.7	0.89	67	1.51
750°C-A120	81	42	3.4	0.86	62	3.22
800°C-A120	76	55	3.1	0.95	36	1.02
650°C-E120	11	41	6.5	0.89	144	1.27
700°C-E120	20	47	3.6	0.78	80	3.27
750°C-E120	45	49	3.7	0.63	36	0.94
800°C-E120	79	73	3.7	0.86	31	1.27

HRTEM results on samples synthesised using either acetylene or ethylene at both low and high flowrates revealed the successful preparation of MWCNTs. However, these MWCNTs contained black spots in the tube cavities that were presumed to be residual particles of the Fe-Co/$CaCO_3$ catalyst. The positioning of residual particles suggested that the tubes were formed via the base-growth mechanism (Chen and Zhu, 2015). It was further observed that the quality of the MWCNTs seemed to detoriarate at synthesis temperatures above 700°C as non-tubular carbon and carbon nanofibers were observed. HRTEM results further revealed the existence of a directly proportional relationship between the synthesis temperature and the average outer diameter of the carbon nanomaterial as can be seen in Table 18. The HRTEM results were also supported by the FESEM results which revealed bundled curled nanotubes which were heterogeneously distributed with non-uniform sizes at synthesis temperatures of below 700°C. At synthesis temperatures of above 700°C, highly disordered carbon nanomaterial was observed. The FESEM micrographs further confirmed the increase in diameter sizes of the carbon nanomaterials as the synthesis temperature increased. EDS further revealed the presence of impurities in the carbon nanomaterials.

Furthermore, the XRD spectra at the tested conditions, showed slightly broadened peaks for all the samples, which was in agreement with the high I_D/I_G ratio reported on Raman spectra. The I_D/I_G for the majority of the samples was above 0.7. Raman spectra further confirmed the successful preparation of MWCNTs since no RBMs and a split in the G was observed. The SSA for a majority of the samples was found to be inversely proportional to the CNTs synthesis temperature.

4.3. Electrochemical testing

4.3.1. CV measurements

Electrode fabricated with commercial graphite

The electrode fabricated with commercial graphite (EFCG) CV was measured in a potential window ranging from 0.02 to 0.8 V at 5 and 10 mV/s scan rates for four cycles each. Figure 49 shows the cyclic voltammograms and the specific capacity graph of the EFCG. In both the CV graphs of Figure 49(a) and Figure 49 (b) where the scan rates were 5 mV/s and 10 mV/s respectively, no peaks were observed. In addition, the shape of the voltammograms showed to be relatively stable and maintained nearly the same positions throughout the cycles. However, the area under the CV seemed to increase with an increase in the scan rate as seen from the increase in current from the anodic side of the voltammograms. This increase in current may be ascribed to

the contact between the electrode and the Li^+ in the electrolyte which generates current because of the redox potential (Navashree and Parthasarathy, 2023). A comparison of the 4th cycle at both scan rates is shown in Figure 49(c) where the distinct effect of scan rate to the current is evident.

In the CV graph, the internal area, mass of the anode materials, and scan rate can be used to determine the specific capacity of the LIB (Lee *et al.*, 2021). The equation used for calculating the specific capacity of the EFCG was as follows (Lee *et al.*, 2021) :

$$C_p = \frac{1}{2\ km} \int i(v)dv \qquad (4.3)$$

Where:

- Cp is the specific capacity in mAh/g
- $(\int i(v)dv)$ is the internal surface area of the CV graph in VA
- m is the mass of the anode material
- k is the scan rate in mV/s

The specific capacity of the EFCG at the different scan rates was calculated using Equation 4.3 and is shown in Figure 49 (d). The average specific capacity in four cycles is 197 mAh/g and 170 mAh/g for the commercial graphite tested at scan rates of 5 mV/s and 10 mV/s respectively. Using a lower scan rate seemed to have an advantage as indicated probably because more lithium ions could be stored due to the electrolyte ions having the opportunity to access the graphite's micropores, which provide the maximum surface area for the charge to build, at slow charge-discharge rates. It was further observed that the degree of capacity loss in the early stages of cycling was high. The reason for the high capacity loss in the early stages may be attributed to the faster degradation of the electrolyte (Tocoglu *et al.*, 2015).

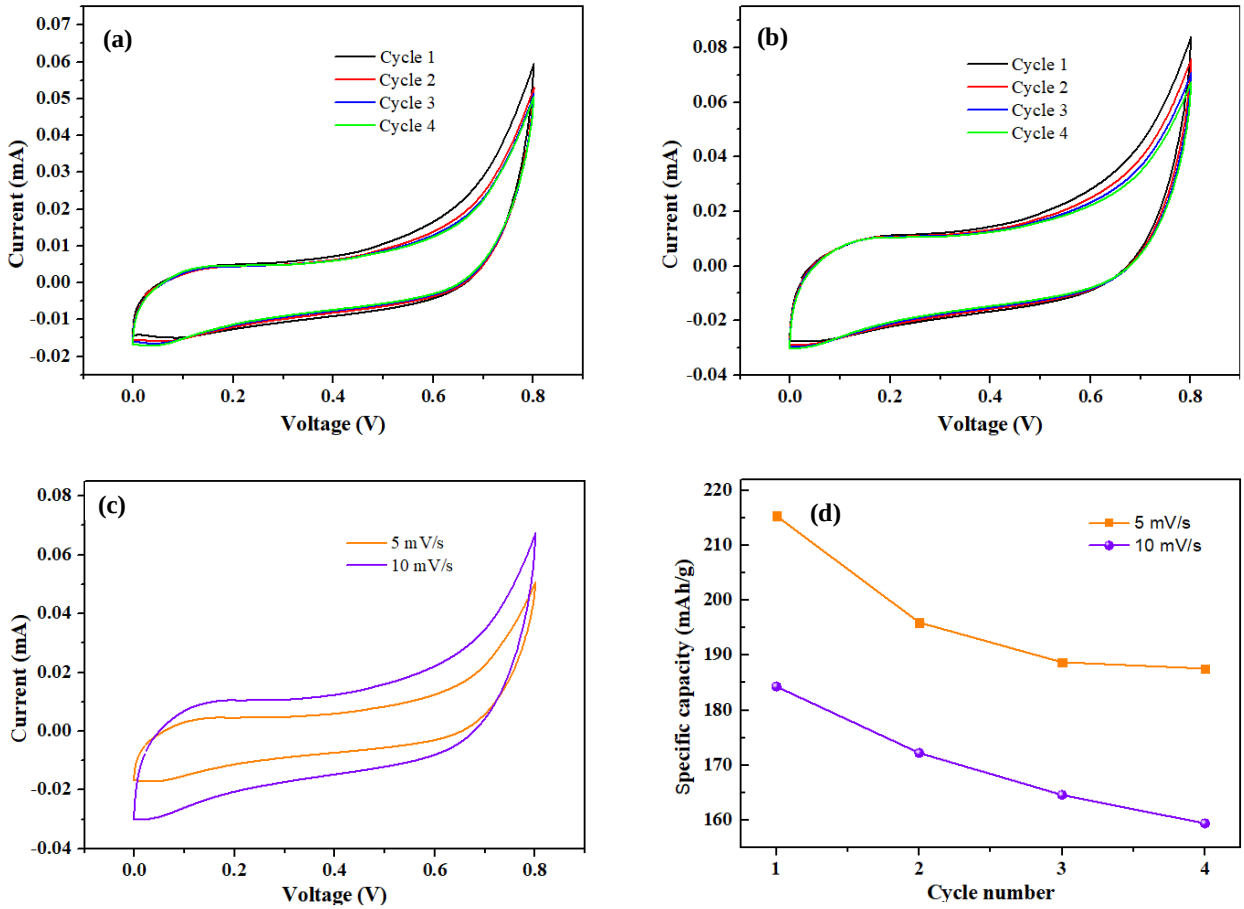

Figure 49: EFCG graphs (a)-(b) cyclic voltammograms at scan rates 5 mV/s, 10 mV/s respectively, (c) cyclic voltammograms of the 4th cycle at scan rates 5 mV/s and 10 mV/s and (d) the specific capacity at scan rate 5 mV/s and 10 mV/s for 4 cycles

<u>CV measurements for electrodes fabricated with CNTs synthesised using 90 mL/min hydrocarbon flowrate</u>

CV measurements conducted on electrodes fabricated with CNTs (EFCNTs) 650°C-A90 and 700°C-A90 at scan rates of 5 mV/s and 10 mV/s are shown in Figure 50. The shape of the cyclic voltammograms looked almost identical for both samples regardless of the scan rate. As seen with the EFCG, the CVs seemed relatively stable as no significant variations in the position of the cycles were observed with the increase in the cycles. However, the area under the CV loops seemed to increase with an increase in the scan rate. One potential explanation could be the high current that flows through the circuit at a high scan rate, which eventually increases the loop area. Insets in Figure 50 (b) and (d) clearly show the difference in areas of the 4^{th} cycle at the different scan rates. An inversely proportional relationship between the synthesis temperature and the internal area of the CV graph was also observed. The internal area of 650°C-A90 showed higher area values

compared to that of 700°C-A90. This was due to the different morphology of the deposited material on the electrodes from the separate CNTs suspensions. Another explanation could be derived from BET results in which the SSA of 650°C-A90 was higher (77 m^2/g) compared to that of 700°C-A90 (65 m^2/g). The high SSA and pore volume of 650°C-A90 meant less resistance to charge transfer between the electrode and electrolyte.

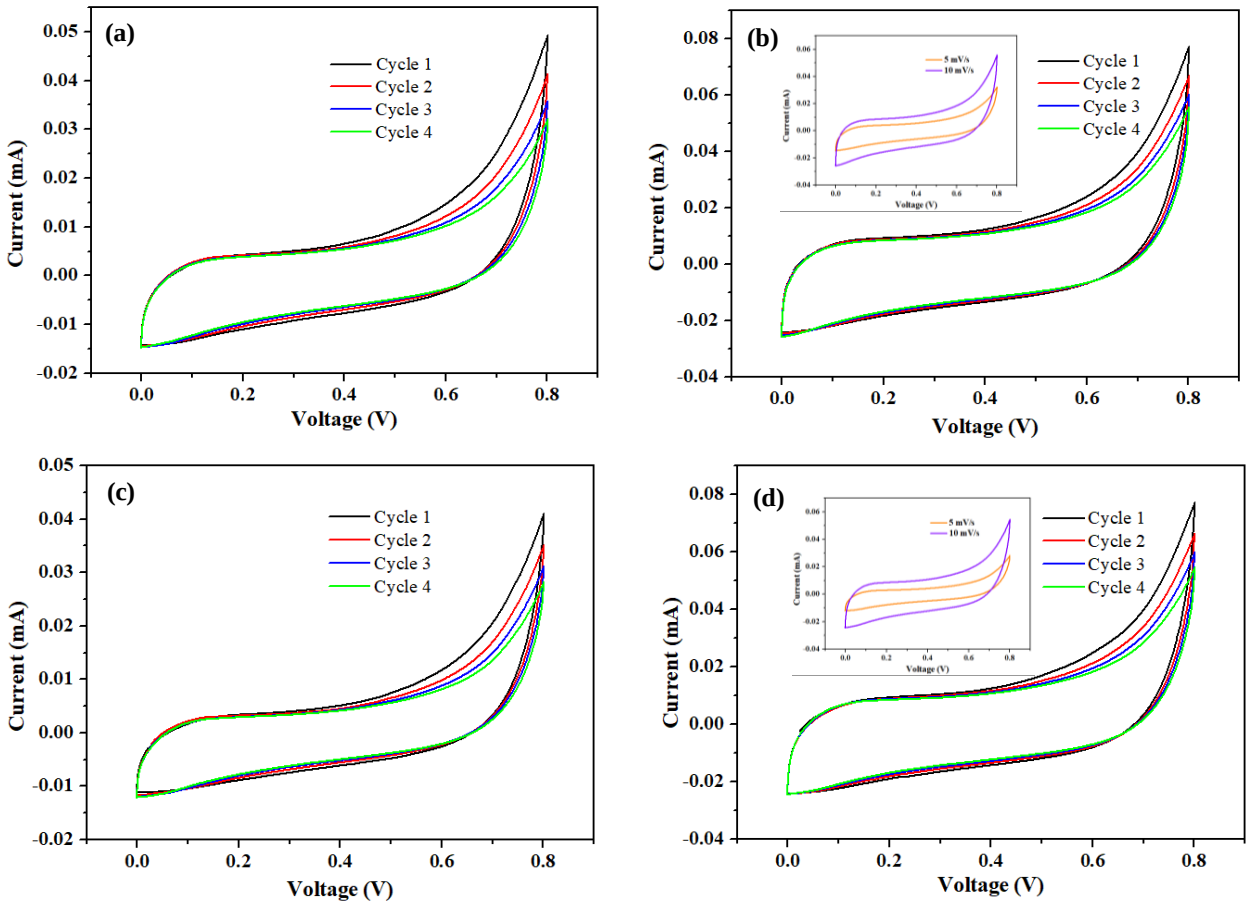

Figure 50: The CV graphs of EFCNTs (a) 650°C-A90 at 5 mV/s scan rate, (b) 650°C-A90 at 10 mV/s scan rate (Inset: CV graphs of the 4th cycle at 5 and 10 mV/s of EFCNTs 650°C-A90), (c) 700°C-A90 at 5 mV/s scan rate and (d)) 700°C-A90 at 10 mV/s scan rate (Inset: CV graphs of the 4th cycle at 5 and 10 mV/s of EFCNTs 700°C-A90)

Figure 51 shows the cyclic voltammograms of the EFCNTs samples prepared using ethylene as a hydrocarbon precursor. As observed with the tests conducted using acetylene at the same test conditions, the shape of the voltammograms looked similar regardless of the scan rate employed. No peaks were observed, however, EFCNTs 650°C-E90 samples (Figure 51 (a) and (b)) presented the largest area enclosed by the CV curve compared to the corresponding EFCNTs 700°C-E90 samples ((Figure 51 (c) and (d)). Similar to the above CV tests, the increase in the scan rate caused

an increase in the current from the anodic side of the voltammograms. This increase in current may be ascribed to the contact time between the electrode and the Li^+ in the electrolyte which generates current because of the redox potential (Navashree and Parthasarathy, 2023).

A variation in the internal area enclosed by the CV curves in both the acetylene and ethylene tests was observed. The tests using acetylene at a scan rate of 5 mV/s showed a larger CV curve area compared to ethylene, while the 10 mV/s tests for both hydrocarbons showed almost equal results.

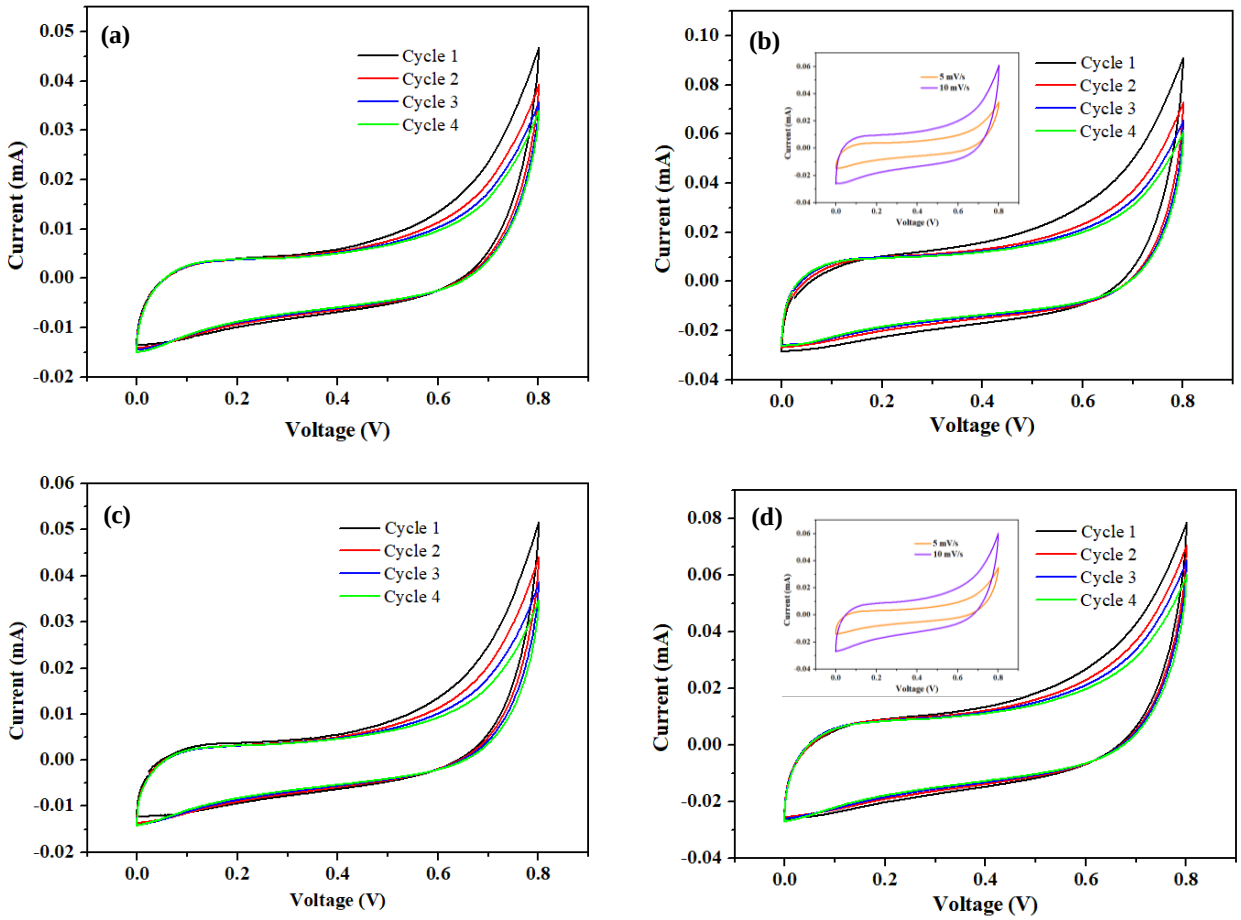

Figure 51: The CV graphs of EFCNTs (a) 650°C-E90 at 5 mV/s scan rate, (b) 650°C-E90 at 10 mV/s scan rate (Inset: CV graphs of the 4th cycle at 5 and 10 mV/s of EFCNTs 650°C-E90), (c) 700°C-E90 at 5 mV/s scan rate and (d)) 700°C-E90 at 10 mV/s scan rate (Inset: CV graphs of the 4th cycle at 5 and 10 mV/s of EFCNTs 700°C-E90)

The specific capacity of EFCNTs 650°C-A90, 700°C-A90, 650°C-E90 and 700°C-E90 at scan rates of 5 mV/s and 10 mV/s is shown in Figure 52 (a) and (b) respectively. The specific capacity was calculated using Equation 4.3. A decline in the capacity was observed as the cycling loops

increased. For the tests conducted at a scan rate of 5 mV/s, the average specific capacity in four cycles was 161 mAh/g, 131 mAh/g, 155 mAh/g and 151 mAh/g for EFCNTs 650°C-A90, 700°C-A90, 650°C-E90 and 700°C-E90 respectively. Contrary, the specific capacity of the tests conducted at a scan rate of 10 mV/s, the specific capacity in four cycles for EFCNTs 650°C-A90, 700°C-A90, 650°C-E90 and 700°C-E90 reported 141 mAh/g, 143 mAh/g, 162 mAh/g and 152 mAh/g. From these specific capacity results an inversely proportional relationship between the synthesis temperature and the specific capacity was observed. This relationship can further be supported by the HRTEM micrographs which revealed the deterioration of the quality of the carbon nanomaterial as the synthesis temperature was increased. In addition, this relationship can also be confirmed by the decrease in the SSA results determined using BET which showed a decrease in the SSA as the synthesis temperature increased. Thus supporting what was reported by Yang et al.,(2008) about the difference in electrochemical performance as a result of different morphology and structure of a material.

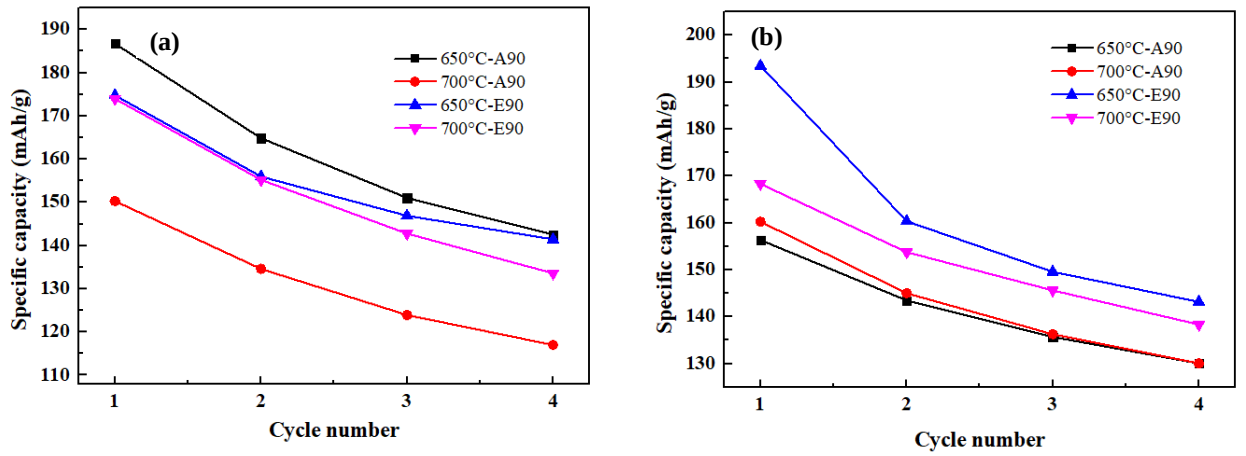

Figure 52: The specific capacity of low hydrocarbon flowrate samples for 4 cycles at scan rates (a) 5 mV/s and (b) 10 mV/s

CV measurements for electrodes fabricated with CNTs synthesised using 120 mL/min hydrocarbon flowrate

CV measurements were further conducted on EFCNTs which were synthesised using acetylene at a flowrate of 120 mL/min. The cyclic voltammograms of EFCNTs 650°C-A120 and 700°C-A120 at scan rates of 5 mV/s and 10 mV/s are shown in Figure 53. The cyclic voltammograms were similar for both samples. The minimal changes in the cycles indicated good stability of the samples at the tested potential window. Similar to the other samples already discussed, an increase in the

scan rate caused an increase in the current from the anodic side of the voltammograms. This increase in current may be attributed to the contact between the electrode and the Li^+ in the electrolyte which generates current because of the redox potential (Navashree and Parthasarathy, 2023).

The effect of the synthesis temperature which also resulted in the difference in morphology of the samples was supported by the difference in the internal area of the CV graphs.

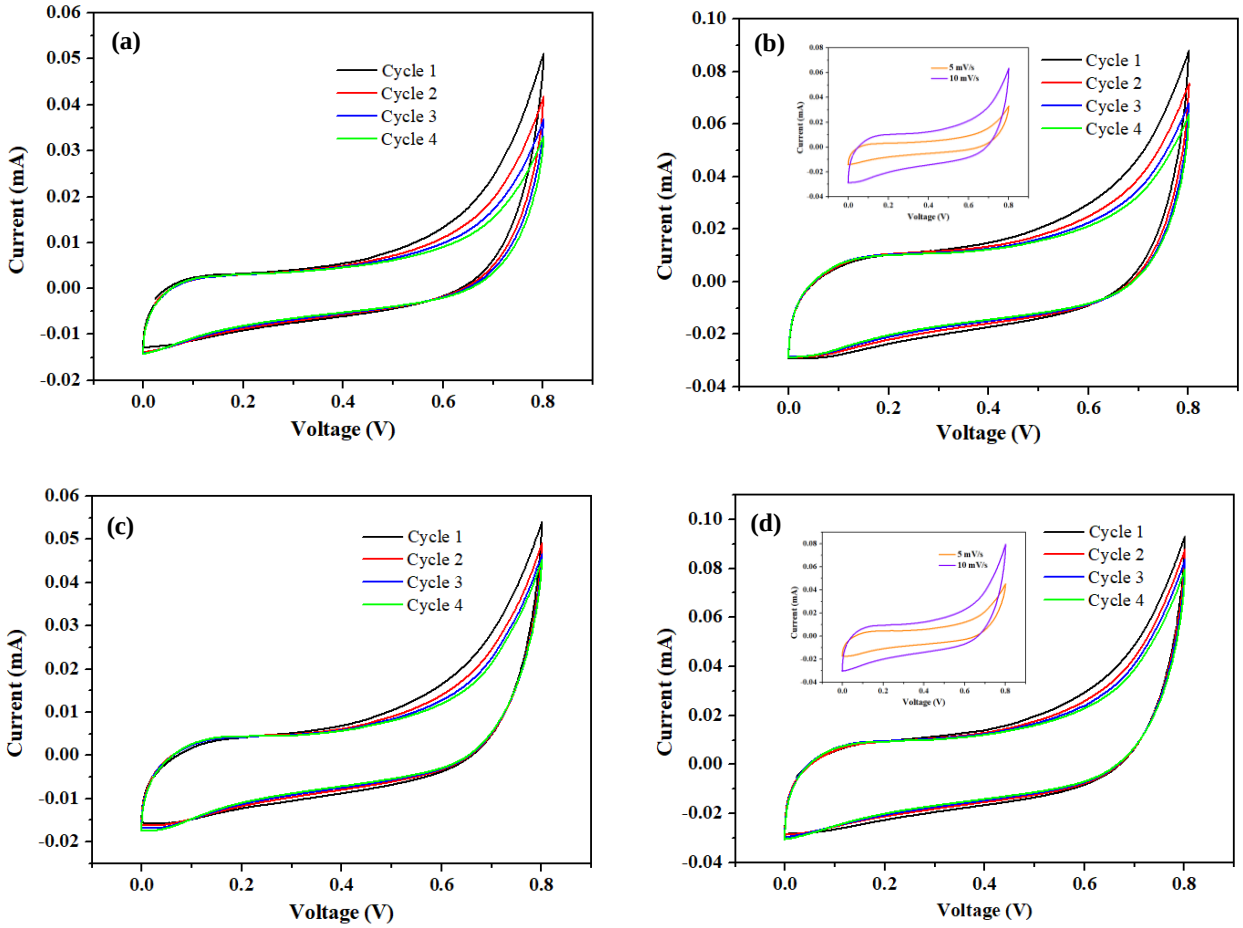

Figure 53: The CV graphs of EFCNTs (a) 650°C-A120 at 5 mV/s scan rate, (b) 650°C-A120 at 10 mV/s scan rate (Inset: CV graphs of the 4th cycle at 5 and 10 mV/s of EFCNTs 650°C-A120), (c) 700°C-A120 at 5 mV/s scan rate and (d)) 700°C-A120 at 10 mV/s scan rate (Inset: CV graphs of the 4th cycle at 5 and 10 mV/s of EFCNTs 700°C-A120)

Figure 54 shows the cyclic voltammograms of the EFCNTs prepared using ethylene as a hydrocarbon precursor at a flowrate of 120 mL/min. As observed with the tests conducted using acetylene at the same test conditions, the shape of the voltammograms was similar regardless of the scan rate employed. Samples of EFCNTs 650°C-A120 (Figure 53 (a) and (b)) presented the

largest area enclosed by the CV curve compared to the corresponding EFCNTs 700°C-E120 samples ((Figure 54 (c) and (d)) possibly because of the higher SSA (97 m^2/g). Another possible reason which is supported by micrographs of HRTEM may be the difficult charge transfer between the electrode and electrolyte as a result of the deterioration of the carbon material at high synthesis temperatures. Similar to the 90 mL/min CV tests, the increase in the scan rate caused an increase in the current from the anodic side of the voltammograms. This increase in current may be ascribed to the contact between the electrode and the Li^+ in the electrolyte which generates current because of the redox potential (Navashree and Parthasarathy, 2023).

It was observed that tests conducted at scan rates 5 mV/s and 10 mV/s using acetylene presented a larger area enclosed by the CV curve as compared to that of ethylene at the same conditions as can be seen in Figure 53 and Figure 54

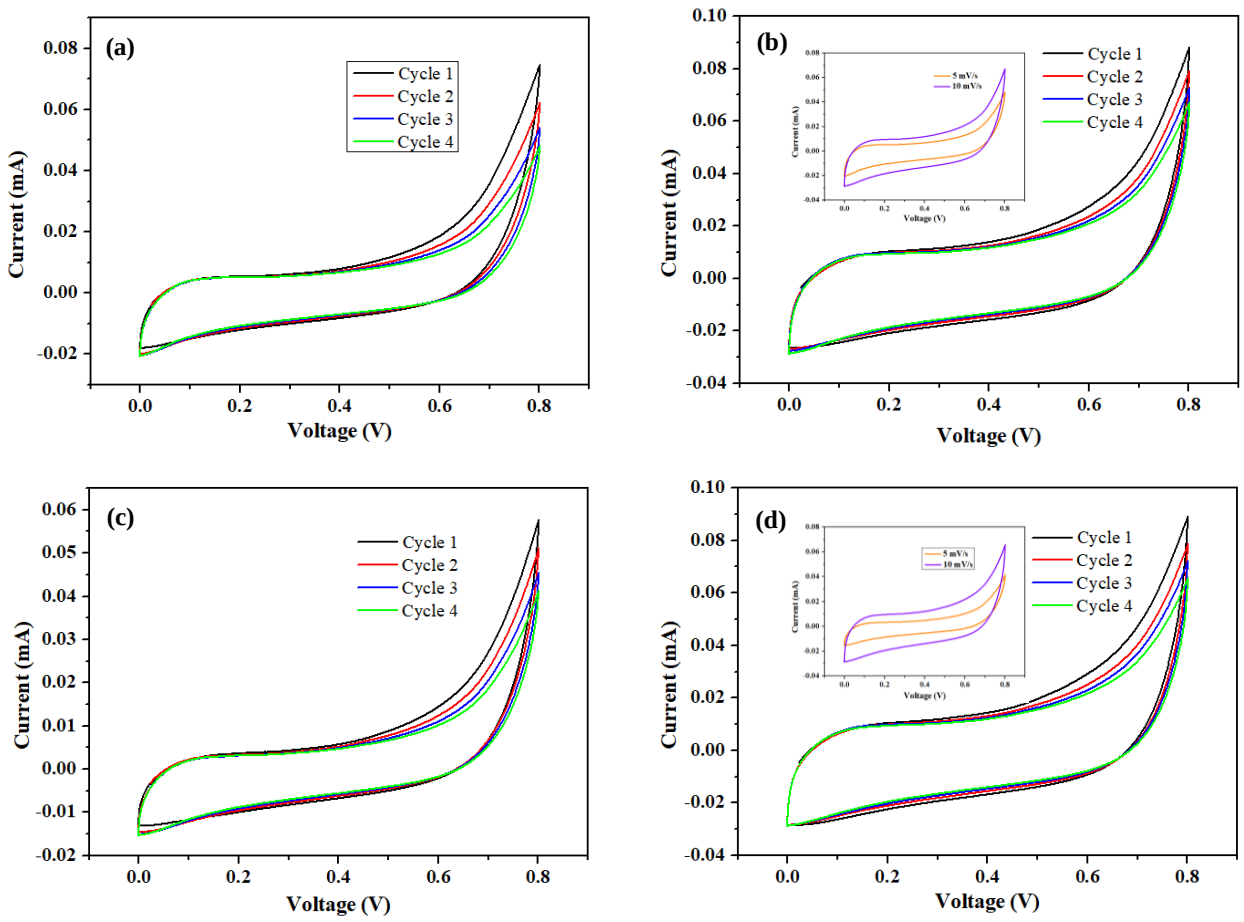

Figure 54: The CV graphs of EFCNTs (a) 650°C-E120 at 5 mV/s scan rate, (b) 650°C-E120 at 10 mV/s scan rate (Inset: CV graphs of the 4th cycle at 5 and 10 mV/s of EFCNTs 650°C-E120),

(c) 700°C-E120 at 5 mV/s scan rate and (d)) 700°C-E120 at 10 mV/s scan rate (Inset: CV graphs of the 4th cycle at 5 and 10 mV/s of 700°C E120)

The specific capacity of EFCNTs 650°C-A120, 700°C-A120, 650°C-E120 and 700°C-E120 at scan rates of 5 mV/s and 10 mV/s is shown in Figure 55 (a) and (b) respectively. The specific capacity was calculated using Equation 4.3. A decrease in the capacity was observed as the cycling loops increased. For the tests conducted at a scan rate of 5 mV/s, the average specific capacity in four cycles was 148 mAh/g, 189 mAh/g, 214 mAh/g and 167 mAh/g for 650°C-A120, 700°C-A120, 650°C-E120 and 700°C-E120 respectively. Contrary, the specific capacity of the tests conducted at a scan rate of 10 mV/s, the average specific capacity in four cycles for 650°C-A120, 700°C-A120, 650°C-E120 and 700°C-E120 reported 168 mAh/g, 174 mAh/g, 162 mAh/g and 167 mAh/g. These differences in the electrochemical performance of the various samples were expected since the morphologies and structures of the samples differed (Yang *et al.*, 2008) as seen from the characterisation results in Section 4.2. The relatively high I_D/I_G ratio reported on Raman, the broadened peaks on XRD and the presence of impurities as seen on the EDS results, had a major impact on the electrochemical performance of the electrodes. Studies have suggested the aligned CNTs may enhance bulk electron transport characteristics by facilitating improved contact with the current collector and increasing ion diffusivity (Welna *et al.*, 2011). Therefore, the results of these specific capacities may be low because of the quality of the CNTs that were produced in this study.

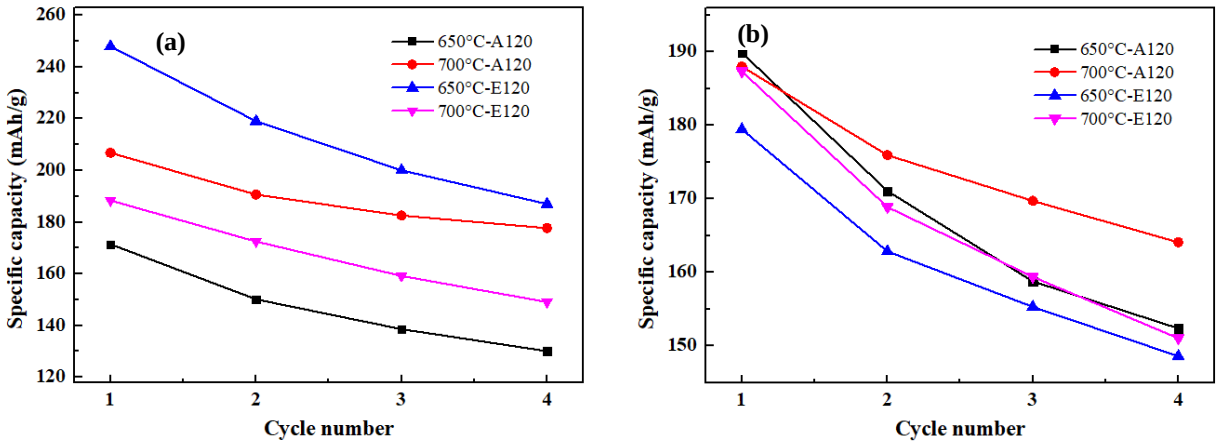

Figure 55: The specific capacity of high hydrocarbon flowrate EFCNTs for 4 cycles at scan rates (a) 5 mV/s and (b) 10 mV/s

4.3.2. EIS measurements

To further understand the electrochemical performance EFCNTs, EIS was performed. Nyquist plots of EFCNTs synthesised using hydrocarbon flowrate of 90 mL/min and 120 mL/min and that of EFCG are shown in Figure 56 and Figure 57. The equivalent circuit that was used for the EIS fitting is shown in Figure 58. The R_s is ascribed to the electrolyte resistance which is the intercept at the Z' axis in the high frequency region. R_{ct} is the charge resistance impedance which takes place at the interface of the electrode and the electrolyte. The CPE (constant phase element) corresponds to the surface charge build-up. The Warburg open circuit T represent the diffusion of the Li^+ species into the bulk of the CNTs electrodes, which is represented by a straight line almost vertical to the Z" axis in the low-frequency region. This straight line showed excellent Li^+ diffusion behaviour in the electrolyte (Jiao *et al.*, 2019).

All the plots contained a depressed semicircle in the high-frequency region as well as a straight line in the low-frequency region. This shape was similar to other CNTs material from other researchers (Zhang *et al.*, 2015) and (Markoulidis, 2019). The thermodynamic parameters obtained from the EIS results of the electrodes are summarised in Table 19. For a majority of the samples excluding EFCG, it was noted that the Rs was directly proportional to the synthesis temperature. It was further noted that the R_s was a bit on the high side and the reason for that may possibly be linked to the operation temperature and/or the concentration of the electrolyte. EFCNTs 650°C-E90 and 700°C-E90 exhibited the lowest R_{ct} value averaging 28Ω which is closer to that of graphite (32Ω). These low Rct results were further supported by Raman results of these two electrodes which revealed that their I_D/I_G were the lowest (0.81 and 0.76) when compared to the rest of the tested ones and thus it suggested that their electronic conductivity was higher (Su *et al.*, 2014) The rest of the electrodes had almost similar Rct values with the slight differences possibly being a fitting error.

Overall, there were no significant variations in the EIS results for the EFCNTs when compared to EFCG. These results were supported by the CV results which also showed minor variations in the specific capacity values of the considered electrodes when compared to the EFCG. The noted variations in the electrochemical performance may be due to the difference in the morphology, structure, surface area and crystallinity of the samples as confirmed by the FESEM, HRTEM, XRD, BET and Raman results. Moreover, studies have shown that the degree of graphitisation,

structural defects, and impurities present in CNTs determine their electrochemical performance, and these factors are governed by the procedures used in their synthesis and treatment (Roselin *et al.*, 2019).

The results indicated that the EFCNTs have a good application potential with doping they may offer superior electrochemical performance than graphite when used as anode material for LIBs (Roselin *et al.*, 2019).

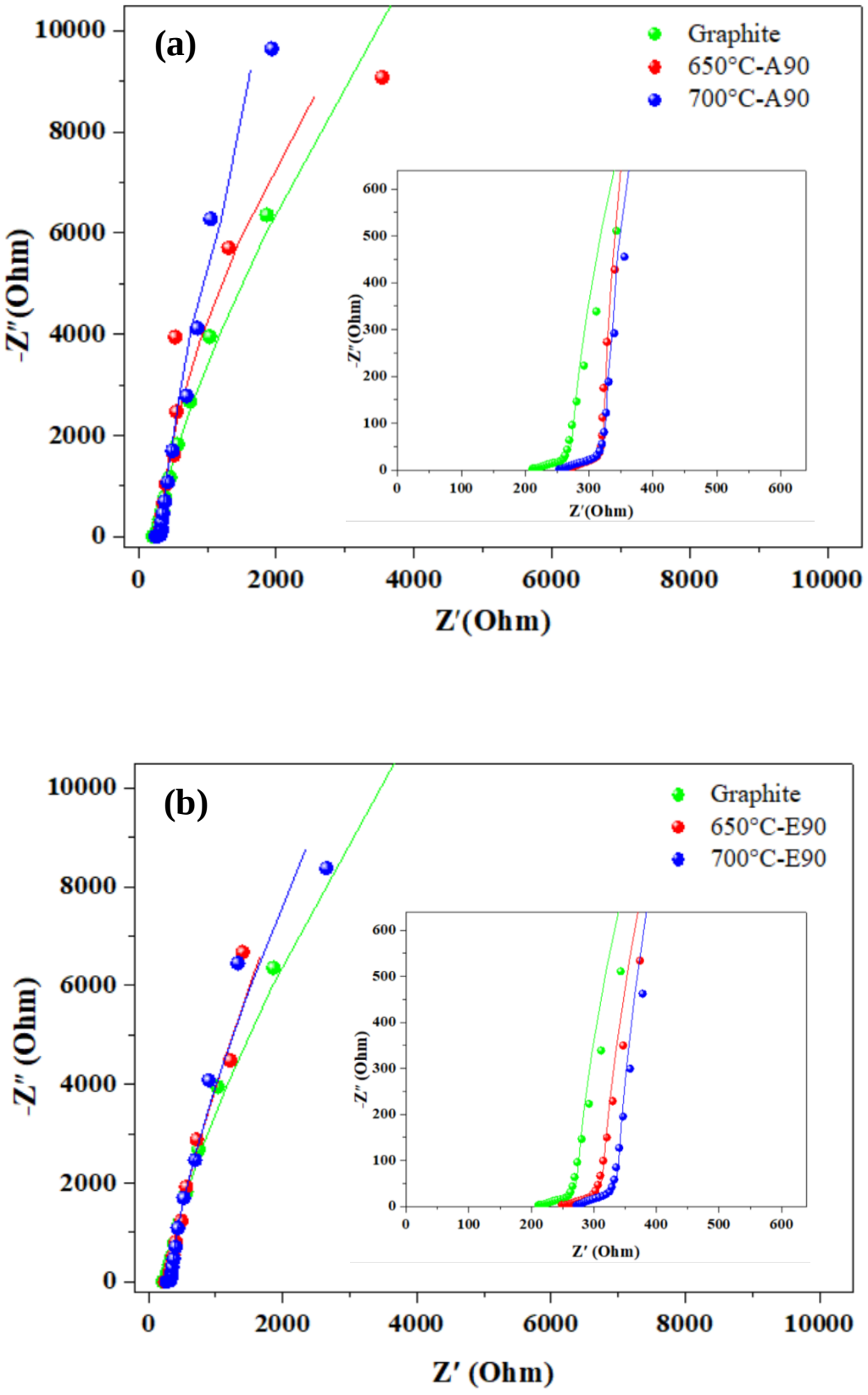

Figure 56: Nyquist plots of (a) EFCG, EFCNTs 650°C-A90 and 700°C-A90 and (b) EFCG, EFCNTs 650°C-E90 and 700°C-E90 where the solid lines are fittings to the data points. The inset is the enlarged view from 0 to 640Ω

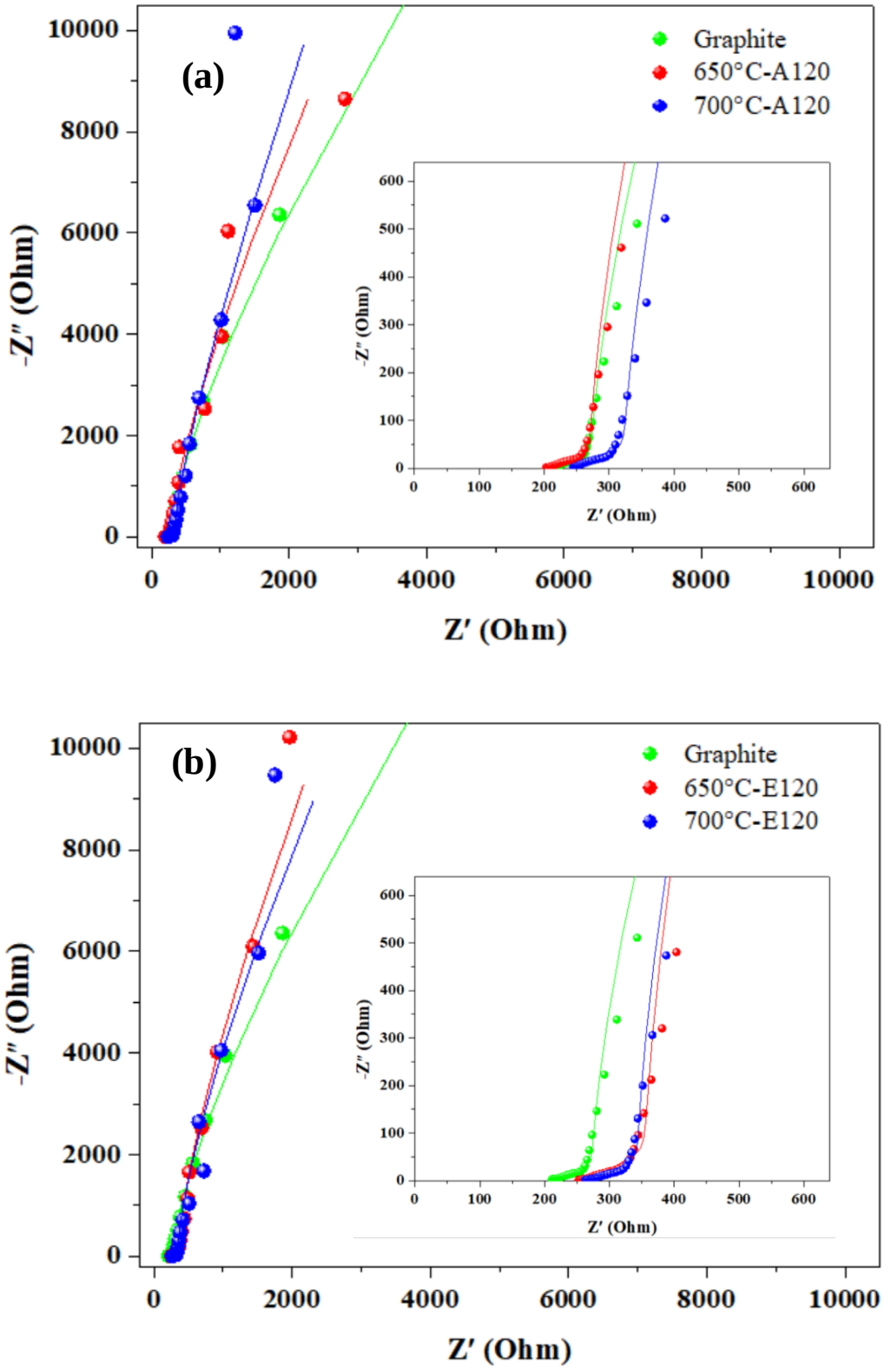

Figure 57: Nyquist plots of (a) EFCG, EFCNTs 650°C-A120 and 700°C-A120 and (b) EFCG, EFCNTs 650°C-E120 and 700°C-E120 where the solid lines are fittings to the data points. The inset is the enlarged view from 0 to 640Ω

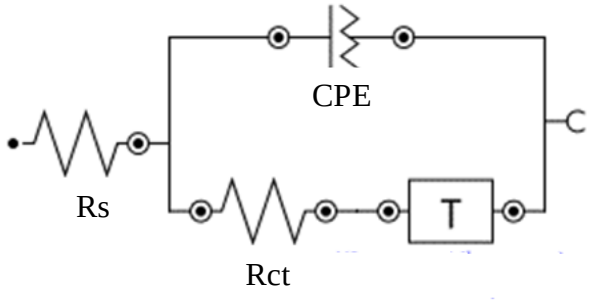

Figure 58: The Randles equivalent circuit used to fit the EIS data

Table 19: EIS fitted parameters of the synthesised carbon nanomaterial electrodes

Working electrode	**R_s (Ω)**	**R_{ct} (Ω)**	**Yo (CPE) (μΩ.s^n)**	**n**	**Yo (T) (μΩ.$s^{0.5}$)**	**b ($s^{0.5}$)**
650°C-A90	265	40	200	0.7	3.5	0.2
700°C-A90	255	34	143	0.7	2.4	0.3
650°C-E90	250	27	142	0.6	3.3	0.2
700°C-E90	265	28	148	0.6	2.2	0.4
650°C-A120	204	33	185	0.6	2.3	0.3
700°C-A120	250	45	207	0.7	2.1	0.3
650°C-E120	252	42	138	0.6	1.8	0.4
700°C-E120	260	40	145	0.6	2.2	0.3
Graphite	210	32	202	0.1	2.3	0.3

4.3.3. A brief overview of the electrochemical performance of the carbon nanomaterial

A summary of the electrochemical performance of the carbon nanomaterial electrodes is provided in Figure 59. Electrochemical results did not show a clear relationship between the specific capacity and the R_{ct}, hence there exists a trade-off between capacity and charge transfer. Ideally a low R_{ct} is required for the ease of electron movement and a higher capacity for the storage of energy.

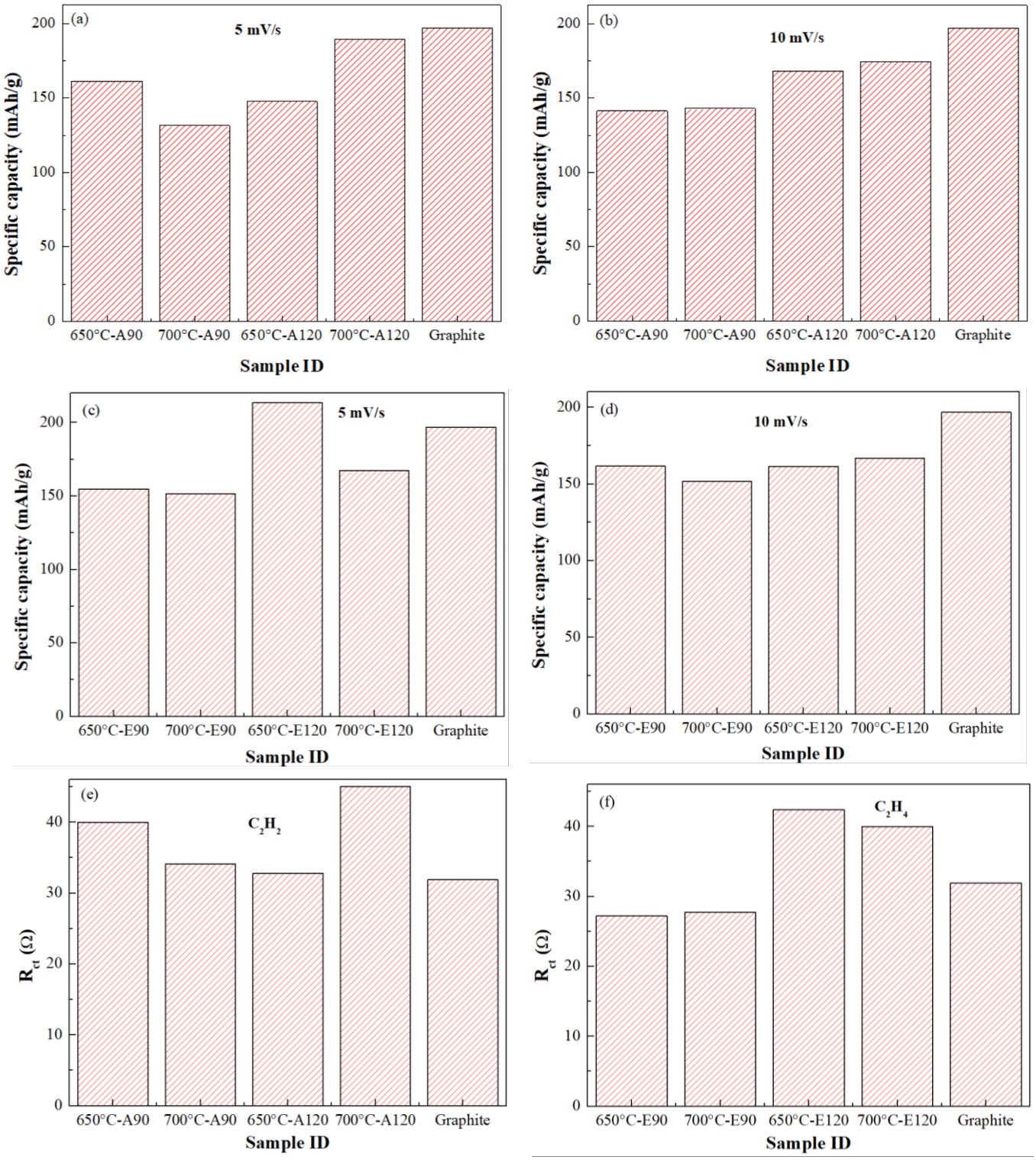

Figure 59: Graphical summary of the electrochemical performance of carbon nanomarterial electrodes

CHAPTER 5

5. CONCLUSIONS AND RECOMMENDATIONS

This study investigated the application of CNTs as anode material for LIBs. Therefore, the objectives of this study which included the synthesis of CNTs at different parameters, fabrication of CNT-Li electrodes and electrochemical testing of the CNT-Li electrodes were met and the following conclusions could be drawn from the results:

- A Fe-Co/$CaCO_3$ catalyst was successfully prepared using the wet impregnation method. BET specific area results of this catalyst were comparable to a commercial grade catalyst reported by Mhlanga *et al.* (2009) where similar preparation conditions were used. XRD results of this catalyst further showed that it was highly crystalline. Overall, the characteristics of the catalysts showed suitability of it being used for the synthesis of CNTs.
- MWCNTs were successfully prepared using the CVD method. Temperature was found to have a great impact on the morphology and structure of the MWCNTs. The quality of the MWCNTs seemed to deteriorate at synthesis temperatures of above 700°C.The hydrocarbon to carrier gas ratio also had a major effect on the quality of the MWCNTs. For tests where 90 mL/min acetylene was used, the synthesis temperatures which gave better CNTs were 650°C and 700°C, however, at tests where 120 mL/min was used, the optimum temperature was found to be 650°C. Contrary, for tests where ethylene was used at both flowrates (90 and 120 mL/min), the synthesis temperatures which gave better quality CNTs were 650°C and 700°C. These MWCNTs however contained some impurities of the residual catalyst as well as some amorphous carbon. The presence of these impurities meant that the mild-acid purification method applied in this study was not sufficient for the removal of the unwanted impurities. Therefore, for future studies it would be beneficial to explore other methods of purification. The SSA of the MWCNTs produced in this study was in the range of ~31 to 144 m^2/g which was within the same range as the commonly reported (~15 to 300 m^2/g) SSA for MWCNTs.
- Electrochemical measurements conducted on selected carbon nanomaterial produced in this study together with electrode fabricated using commercial graphite for comparison purposes, agreed with the hypothesis of this study as the electrochemical performance varied as per the morphology and structure of the materials. The optimum specific capacity

for the electrode fabricated with commercial graphite was found to have fallen short of the theoretical capacity of the electrode fabricated with commercial graphite which is 372 mAh/g compared to 197 mAh/g reported in this study. The optimum specific capacity obtained in this study (214 mAh/g) also fell short to the theoretical capacity of the electrode fabricated with commercial graphite however this result indicated that MWCNTs electrodes have a good application potential and with doping they may offer superior electrochemical performance than graphite when used as anode material for LIBs.

The recommendations for further research include:

- Optimisation of the electrolyte used in electrochemical testing. This study used a mixture of 1:1 EC:DMC in 1M $LiPF_6$. It is therefore recommended that other Li salts be tested to evaluate the movement of ions in such mediums.
- Use of a different solvent in the dispersion of CNTs for electrode fabrication.
- Doping of CNTs using different dopants to examine the electrochemical performance of the doped CNTs.
- Evaluate the use of gold screen-printed electrodes for electrochemical testing.
- Increase the number of cycles for both CV and EIS tests to evaluate the stability of the synthesised material.

6. REFERENCES

Bachilo, S.M., Balzano, L., Herrera, J.E., Pompeo, F., Resasco, D.E. and Weisman, R.B. (2003) 'Narrow (n,m)-distribution of single-walled carbon nanotubes grown using a solid supported catalyst', Journal of the American Chemical Society, 125(37), pp. 11186–11187. Available at: https://doi.org/10.1021/ja036622c.

Baranski, A.S. (1991) 'Optimization of ac voltammetric measurements at ultramicroelectrodes', *Journal of Electroanalytical Chemistry*, 300(1–2), pp. 309–324. Available at: https://doi.org/https://doi.org/10.1016/0022-0728(91)85402-B.

Birch, M.E., Ruda-Eberenz, T.A., Chai, M., Andrews, R. and Hatfield, R.L. (2013) 'Properties that influence the specific surface areas of carbon nanotubes and nanofibers', *Annals of Occupational Hygiene*, 57(9), pp. 1148–1166. Available at: https://doi.org/10.1093/annhyg/met042.

Bradley, R.H., Cassity, K., Andrews, R., Meier, M., Osbeck, S., Andreu, A., Johnston, C. and Crossley, A. (2012) 'Applied Surface Science Surface studies of hydroxylated multi-wall carbon nanotubes', *Applied Surface Science*, 258(11), pp. 4835–4843. Available at: https://doi.org/10.1016/j.apsusc.2012.01.008.

Brett, C.M.A., Maria, A.N.A. and Brett, O. (1994) *Electrochemistry: Principles , Methods , and Applications*. New York: Oxford University Press Inc.

Carrara, S. (2010) 'Nano-bio-technology and sensing chips: New systems for detection in personalized therapies and cell biology', *Sensors*, 10(1), pp. 526–543. Available at: https://doi.org/10.3390/s100100526.

Chakraborty, S., Chattopadhyay, J., Peng, H., Chen, Z., Mukherjee, A., Arvidson, R.S., Hauge, R.H. and Billups, W.E. (2006) 'Surface area measurement of functionalized single-walled carbon nanotubes', *Journal of Physical Chemistry B*, 110(49), pp. 24812–24815. Available at: https://doi.org/10.1021/jp065044u.

Chen, M., Yu, H., Chen, J. and Koo, H. (2007) 'Effect of purification treatment on adsorption characteristics of carbon nanotubes', *Diamond and Related Materials*, 16, pp. 1110–1115. Available at: https://doi.org/10.1016/j.diamond.2006.12.061.

Chen, Y.M. and Zhu, Y. (2015) 'CVD of carbon nanotubes in porous nickel for anodes in lithium ion battery', *Current Opinion in Chemical Engineering*, 7, pp. 32–39. Available at: https://doi.org/10.1016/j.coche.2014.11.001.

Choubey, P.K., Kim, M., Srivastava, R.R., Lee, Jae-chun and Lee, Jin-young (2016) 'Advance review on the exploitation of the prominent energy-storage element : Lithium . Part I : From mineral and brine resources', *Minerals Engineering*, 89, pp. 119–137. Available at: https://doi.org/10.1016/j.mineng.2016.01.010.

Coquay, P., De Grave, E., Peigney, A., Vandenberghe, R.E. and Laurent, C. (2002) 'Carbon nanotubes by a CVD method. Part I: Synthesis and characterization of the (Mg, Fe)O catalysts', *Journal of Physical Chemistry B*, 106(51), pp. 13186–13198. Available at: https://doi.org/10.1021/jp026631s.

Costa, S., Borowiak-Palen, E., Kruszyñska, M., Bachmatiuk, A. and Kaleńczuk, R.J. (2008) 'Characterization of carbon nanotubes by Raman spectroscopy', *Materials Science- Poland*, 26(2), pp. 433–441.

Danafar, F., Fakhru'l-Razi, A., Salleh, M.A.M. and Biak, D.R.A. (2009) 'Fluidized bed catalytic chemical vapor deposition synthesis of carbon nanotubes-A review', *Chemical Engineering*

Journal, 155(1–2), pp. 37–48. Available at: https://doi.org/10.1016/j.cej.2009.07.052.

Ding, F., Harutyunyan, A.R. and Yakobson, B.I. (2009) 'Dislocation theory of chirality-controlled nanotube growth', *Proceedings of the National Academy of Sciences of the United States of America*, 106(8), pp. 2506–2509. Available at: https://doi.org/10.1073/pnas.0811946106.

Dresselhaus, M.S., Dresselhaus, G., Saito, R. and Jorio, A. (2005) 'Raman spectroscopy of carbon nanotubes', *Physics Reports*, 409(2), pp. 47–99. Available at: https://doi.org/10.1016/j.physrep.2004.10.006.

Dresselhaus, M.S., Jorio, A., Hofmann, M., Dresselhaus, G. and Saito, R. (2010) 'Perspectives on carbon nanotubes and graphene Raman spectroscopy', *Nano Letters*, 10(3), pp. 751–758. Available at: https://doi.org/10.1021/nl904286r.

Dresselhaus, M.S., Dresselhaus, G. and Hofmann, M. (2007) 'The big picture of Raman scattering in carbon nanotubes', *Vibrational Spectroscopy*, 45(2), pp. 71–81. Available at: https://doi.org/10.1016/j.vibspec.2007.07.004.

Dupuis, A.C. (2005) 'The catalyst in the CCVD of carbon nanotubes-a review', *Progress in Materials Science*, 50(8), pp. 929–961. Available at: https://doi.org/10.1016/j.pmatsci.2005.04.003.

Elgrishi, N., Rountree, K.J., McCarthy, B.D., Rountree, E.S., Eisenhart, T.T. and Dempsey, J.L. (2018) 'A Practical Beginner's Guide to Cyclic Voltammetry', *Journal of Chemical Education*, 95(2), pp. 197–206. Available at: https://doi.org/10.1021/acs.jchemed.7b00361.

Fleischmann, J., Schaufuss, P., Linder, M., Hanicke, M., Horetsky, E., Ibrahim, D., Jautelat, S., Torscht, L. and van de Rijt, A. (2023) *Battery 2030: Resilient, sustainable, and circular*. Available at: https://www.mckinsey.com/industries/automotive-and-assembly/our-insights/battery-2030-resilient-sustainable-and-circular (Accessed: 28 June 2023).

Gamry Instruments (2017) *Cyclic Voltammetry, Gamry Instruments, Inc.* Available at: https://doi.org/10.1007/978-3-319-04388-3_7.

Gao, X., Jiang, L., Lu, X., Zhou, X., Li, C., Shi, J. and Sheng, L. (2024) 'High performance flexible lithium-ion battery anodes: Carbon nanotubes bridging bamboo-shaped carbon-coated manganese oxide nanowires via carbon welding', *Journal of Alloys and Compounds*, 971(November 2023). Available at: https://doi.org/10.1016/j.jallcom.2023.172728.

Goriparti, S., Miele, E., De Angelis, F., Di Fabrizio, E., Proietti Zaccaria, R. and Capiglia, C. (2014) 'Review on recent progress of nanostructured anode materials for Li-ion batteries', *Journal of Power Sources*, 257, pp. 421–443. Available at: https://doi.org/10.1016/j.jpowsour.2013.11.103.

Habekost, A. (2021) 'Fundamentals and Applications of Electrochemical Impedance Spectroscopy - A Didactic Perspective', *World Journal of Chemical Education*, 9(1), pp. 14–21. Available at: https://doi.org/10.12691/wjce-9-1-3.

Hamada, N., Sawada, S.I. and Oshiyama, A. (1992) 'New one-dimensional conductors: Graphitic microtubules', *Physical Review Letters*, 68(10), pp. 1579–1581. Available at: https://doi.org/10.1103/PhysRevLett.68.1579.

Hawley, W.B. and Li, J. (2019) 'Electrode manufacturing for lithium-ion batteries—Analysis of current and next generation processing', *Journal of Energy Storage*, 25(June), p. 100862. Available at: https://doi.org/10.1016/j.est.2019.100862.

Ismail, A.F., Goh, P.S., Tee, J.C., Sanip, S.M. and Aziz, M. (2008) 'A review of purification techniques for carbon nanotubes', *Nano*, 3(3), pp. 127–143. Available at: https://doi.org/10.1142/S1793292008000927.

Jagadeesan, A.K., Thangavelu, K. and Dhananjeyan, V. (2020) 'Carbon Nanotubes: Synthesis, Properties and Applications', in *21st Century Surface Science - a Handbook*. IntechOpen. Available at: https://doi.org/10.5772/intechopen.92995.

Jiao, S., Li, T., Xiong, C., Tang, C., Dang, A., Li, H. and Zhao, T. (2019) 'A facile method of preparing the asymmetric supercapacitor with two electrodes assembled on a sheet of filter paper', *Nanomaterials*, 9(9). Available at: https://doi.org/10.3390/nano9091338.

Kathyayini, H., Nagaraju, N., Fonseca, A. and Nagy, J.B. (2004) 'Catalytic activity of Fe, Co and Fe/Co supported on Ca and Mg oxides, hydroxides and carbonates in the synthesis of carbon nanotubes', *Journal of Molecular Catalysis A: Chemical*, 223(1–2), pp. 129–136. Available at: https://doi.org/10.1016/j.molcata.2004.02.029.

Keller, T.M., Qadri, S.B. and Little, C.A. (2004) 'Carbon nanotube formation in situ during carbonization in shaped bulk solid cobalt nanoparticle compositions', *Journal of Materials Chemistry*, 14(20), pp. 3063–3070. Available at: https://doi.org/10.1039/b402936d.

Kim, H.J., Krishna, T.N.V., Zeb, K., Rajangam, V., Muralee Gopi, C.V.V., Sambasivam, S., Raghavendra, K.V.G. and Obaidat, I.M. (2020) *A comprehensive review of li-ion battery materials and their recycling techniques*, *Electronics (Switzerland)*. Available at: https://doi.org/10.3390/electronics9071161.

Kim, Haegyeom, Hong, J., Park, K.Y., Kim, Hyungsub, Kim, S.W. and Kang, K. (2014) 'Aqueous rechargeable Li and Na ion batteries', *Chemical Reviews*, 114(23), pp. 11788–11827. Available at: https://doi.org/10.1021/cr500232y.

Kuznetsov, V.L., Bokova-Sirosh, S.N., Moseenkov, S.I., Ishchenko, A. V., Krasnikov, D. V., Kazakova, M.A., Romanenko, A.I., Tkachev, E.N. and Obraztsova, E.D. (2014) 'Raman spectra for characterization of defective CVD multi-walled carbon nanotubes', *Physica Status Solidi (B) Basic Research*, 251(12), pp. 2444–2450. Available at: https://doi.org/10.1002/pssb.201451195.

De Las Casas, C. and Li, W. (2012) 'A review of application of carbon nanotubes for lithium ion battery anode material', *Journal of Power Sources*, 208, pp. 74–85. Available at: https://doi.org/10.1016/j.jpowsour.2012.02.013.

Lee, S., Kwon, S., Kim, K., Kang, H., Ko, J.M. and Choi, W. (2021) 'Preparation of carbon nanowall and carbon nanotube for anode material of lithium-ion battery', *Molecules*, 26(22), pp. 1–7. Available at: https://doi.org/10.3390/molecules26226950.

Lee, S.W., Yabuuchi, N., Gallant, B.M., Chen, S., Kim, B.S., Hammond, P.T. and Shao-Horn, Y. (2010) 'High-power lithium batteries from functionalized carbon-nanotube electrodes', *Nature Nanotechnology*, 5(7), pp. 531–537. Available at: https://doi.org/10.1038/nnano.2010.116.

LibreTexts (2022) *X-ray diffraction (XRD) basics and application - Chemistry LibreTexts*. Available at: https://chem.libretexts.org/Courses/Franklin_and_Marshall_College/Introduction_to_Materials_Characterization__CHM_412_Collaborative_Text/Diffraction_Techniques/X-ray_diffraction_(XRD)_basics_and_application (Accessed: 5 January 2024).

Lightweight Materials Market Size, Share | Forecast 2030 (no date). Available at: https://www.sphericalinsights.com/reports/lithium-ion-battery-market (Accessed: 28 June 2023).

Lim, S.H. and Lin, J. (2011) 'Synthesis of carbon nanotubes', *Carbon Nanotubes and their Applications*, pp. 31–72. Available at: https://doi.org/10.4032/9789814303187.

Liu, B., Sun, X., Liao, Z., Lu, X., Zhang, L. and Hao, G.P. (2021) 'Nitrogen and boron doped carbon layer coated multiwall carbon nanotubes as high performance anode materials for lithium ion

batteries', *Scientific Reports*, 11(1), pp. 1–11. Available at: https://doi.org/10.1038/s41598-021-85187-5.

Liu, H., Cheng, X., Chong, Y., Yuan, H., Huang, J.Q. and Zhang, Q. (2021) 'Advanced electrode processing of lithium ion batteries: A review of powder technology in battery fabrication', *Particuology*, 57, pp. 56–71. Available at: https://doi.org/10.1016/j.partic.2020.12.003.

Liu, J., Wang, C., Tu, X., Liu, B., Chen, L., Zheng, M. and Zhou, C. (2012) 'Chirality-controlled synthesis of single-wall carbon nanotubes using vapour-phase epitaxy', *Nature Communications*, 3, pp. 1–7. Available at: https://doi.org/10.1038/ncomms2205.

Lu, K., Zhao, C. and Jiang, Y. (2021) 'Research progress of cathode materials for lithium-ion batteries', in *E3S Web of Conferences*. Available at: https://doi.org/10.1051/e3sconf/202123301020.

Magar, H.S., Hassan, R.Y.A. and Mulchandani, A. (2021) 'Electrochemical impedance spectroscopy (Eis): Principles, construction, and biosensing applications', *Sensors*, 21(19). Available at: https://doi.org/10.3390/s21196578.

Mallard Creek Polymers (2021) *Amorphous vs. Crystalline Polymers*, *Mallard Creek Polymers*. Available at: https://www.mcpolymers.com/library/amorphous-vs-crystalline-polymers#:~:text=Crystallinity can range from 0,role in polymer crystal formation. (Accessed: 22 May 2024).

Markoulidis, F. (2019) 'Composite Electrodes of Activated Carbon and Multiwall Carbon Nanotubes Decorated with Silver Nanoparticles for High Power Energy Storage', *Journal of Composites Science* [Preprint], (November). Available at: https://doi.org/10.3390/jcs3040097.

Meddings, N., Heinrich, M., Overney, F., Lee, J.S., Ruiz, V., Napolitano, E., Seitz, S., Hinds, G., Raccichini, R., Gaberšček, M. and Park, J. (2020) 'Application of electrochemical impedance spectroscopy to commercial Li-ion cells: A review', *Journal of Power Sources*, 480(May). Available at: https://doi.org/10.1016/j.jpowsour.2020.228742.

Metrohm (2023) *Electrochemical Impedance Spectroscopy*, *Metrohm*. Available at: https://doi.org/10.1201/9781003299295-11.

Mhlanga, S.D., Mondal, K.C., Carter, R., Witcomb, M.J. and Coville, N.. (2009) 'The effect of synthesis parameters on the catalytic synthesis of multiwalled carbon nanotubes using Fe-Co/CaCO3 catalysts', *South African Journal of Chemistry*, 62, pp. 67–76.

Navashree, N. and Parthasarathy, P. (2023) 'A comparative study on electrochemical behaviour of various electrolytes by cyclic voltammetry: GCE as electrode material', *Materials Today: Proceedings* [Preprint], (xxxx). Available at: https://doi.org/10.1016/j.matpr.2023.05.175.

Nitta, N., Wu, F., Lee, J.T. and Yushin, G. (2015) 'Li-ion battery materials: Present and future', *Materials Today*, 18(5), pp. 252–264. Available at: https://doi.org/10.1016/j.mattod.2014.10.040.

Osiak, M., Geaney, H., Armstrong, E. and O'Dwyer, C. (2014) 'Structuring materials for lithium-ion batteries: Advancements in nanomaterial structure, composition, and defined assembly on cell performance', *Journal of Materials Chemistry A*, 2(25), pp. 9433–9460. Available at: https://doi.org/10.1039/c4ta00534a.

Peigney, A., Laurent, C., Flahaut, E., Bacsa, R.R. and Rousset, A. (2001) 'Specific surface area of carbon nanotubes and bundles of carbon nanotubes', *Carbon*, 39, p. 507.

Pinkwart, K. and Tübke, J. (2011) 'Fundamentals and General Aspects of Electrochemical Energy Storage Thermodynamics and Mechanistics', *Handbook of Battery Materials*, pp. 1–26.

Rathinavel, S., Priyadharshini, K. and Panda, D. (2021) 'A review on carbon nanotube: An overview of synthesis, properties, functionalization, characterization, and the application', *Materials Science and Engineering B: Solid-State Materials for Advanced Technology*, 268(January 2020), p. 115095. Available at: https://doi.org/10.1016/j.mseb.2021.115095.

Roselin, L.S., Juang, R.S., Hsieh, C. Te, Sagadevan, S., Umar, A., Selvin, R. and Hegazy, H.H. (2019) 'Recent advances and perspectives of carbon-based nanostructures as anode materials for Li-ion batteries', *Materials*, 12(8). Available at: https://doi.org/10.3390/ma12081229.

Saifuddin, N., Raziah, A.Z. and Junizah, A.R. (2013) 'Carbon nanotubes: A review on structure and their interaction with proteins', *Journal of Chemistry*, 2013. Available at: https://doi.org/10.1155/2013/676815.

Shah, K.A. and Tali, B.A. (2016) 'Synthesis of carbon nanotubes by catalytic chemical vapour deposition: A review on carbon sources, catalysts and substrates', *Materials Science in Semiconductor Processing*, 41, pp. 67–82. Available at: https://doi.org/10.1016/j.mssp.2015.08.013.

Shudin, N.H., Mukri, M. 'Azizir R., Aziz, M., Othman, M.H.D., Tanemura, M. and Mohd Yusop, M.Z. (2021) 'The role of solid, liquid and gaseous hydrocarbon precursors on chemical vapor deposition grown carbon nanomaterials' growth temperature', *Synthetic Metals*, 274(February), p. 116735. Available at: https://doi.org/10.1016/j.synthmet.2021.116735.

Su, L., Li, X., Ming, H., Adkins, J., Liu, M., Zhou, Q. and Zheng, J. (2014) 'Effect of vanadium doping on electrochemical performance of LiMnPO 4 for lithium-ion batteries', *Journal of Solid State Electrochemistry*, 18(3), pp. 755–762. Available at: https://doi.org/10.1007/s10008-013-2315-9.

Su, M., Zheng, B. and Liu, J. (2000) 'A scalable CVD method for the synthesis of single-walled carbon nanotubes with high catalyst productivity', *Chemical Physics Letters*, 322(5), pp. 321–326. Available at: https://doi.org/10.1016/S0009-2614(00)00422-X.

Swain, B. (2017) 'Recovery and recycling of lithium: A review', *Separation and Purification Technology*, 172, pp. 388–403. Available at: https://doi.org/10.1016/j.seppur.2016.08.031.

Swanson, H.E., McMurdie, H.F., Morris, M.C. and Evans, E.H. (1968) *Standard X-ray Diffraction Powder Patterns*. Washington, D.C.: U.S. Department of Commerce.

Szabó, A., Perri, C., Csató, A., Giordano, G., Vuono, D. and Nagy, J.B. (2010) 'Synthesis methods of carbon nanotubes and related materials', *Materials*, 3(5), pp. 3092–3140. Available at: https://doi.org/10.3390/ma3053092.

Tocoglu, U., Cevher, O. and Akbulut, H. (2015) 'Cyclic performance tests of Si/MWCNT composite lithium ion battery anodes at different temperatures', *Acta Physica Polonica A*, 127(4), pp. 1059–1061. Available at: https://doi.org/10.12693/APhysPolA.127.1059.

Tran, K.Y., Heinrichs, B., Colomer, J.F., Pirard, J.P. and Lambert, S. (2007) 'Carbon nanotubes synthesis by the ethylene chemical catalytic vapour deposition (CCVD) process on Fe, Co, and Fe-Co/Al2O3 sol-gel catalysts', *Applied Catalysis A: General*, 318, pp. 63–69. Available at: https://doi.org/10.1016/j.apcata.2006.10.042.

U.S. Geological Survey (2018) *U. S. Geological Survey: Mineral Commodity Summaries*, *U.S. Geological Survey*. Available at: https://doi.org/10.3133/70194932.

UL Research Institutes (2021) *What Are Lithium-Ion Batteries? | UL Research Institutes*. Available at: https://ul.org/research/electrochemical-safety/getting-started-electrochemical-safety/what-are-lithium-ion (Accessed: 25 May 2024).

Vinayak, A.K., Xu, Z., Li, G. and Wang, X. (2023) 'Current Trends in Sourcing, Recycling, and Regeneration of Spent Lithium-Ion Batteries—A Review', *Renewables*, (February), pp. 1–22. Available at: https://doi.org/10.31635/renewables.023.202200008.

Vu, A., Qian, Y. and Stein, A. (2012) 'Porous electrode materials for lithium-ion batteries-how to prepare them and what makes them special', *Advanced Energy Materials*, 2(9), pp. 1056–1085. Available at: https://doi.org/10.1002/aenm.201200320.

Wang, X.-D., Vinodgopal, K. and Dai, G.-P. (2019) 'Synthesis of Carbon Nanotubes by Catalytic Chemical Vapor Deposition', in *Perspective of Carbon Nanotubes*. IntechOpen. Available at: https://doi.org/10.5772/intechopen.86995.

Welna, D.T., Qu, L., Taylor, B.E., Dai, L. and Durstock, M.F. (2011) 'Vertically aligned carbon nanotube electrodes for lithium-ion batteries', *Journal of Power Sources*, 196(3), pp. 1455–1460. Available at: https://doi.org/10.1016/j.jpowsour.2010.08.003.

Westerhoff, U., Kroker, T., Kurbach, K. and Kurrat, M. (2016) 'Electrochemical impedance spectroscopy based estimation of the state of charge of lithium-ion batteries', *Journal of Energy Storage*, 8, pp. 244–256. Available at: https://doi.org/10.1016/j.est.2016.09.001.

Widjonarko, N. (2016) 'Introduction to Advanced X-ray Diffraction Techniques for Polymeric Thin Films', *Coatings*, 6(4), p. 54. Available at: https://doi.org/10.3390/coatings6040054.

Wu, Y., Wang, J., Jiang, K. and Fan, S. (2014) 'Applications of carbon nanotubes in high performance lithium ion batteries', *Frontiers of Physics*, 9(3), pp. 351–369. Available at: https://doi.org/10.1007/s11467-013-0308-x.

Xiong, Z., Yun, Y.S. and Jin, H.J. (2013) 'Applications of carbon nanotubes for lithium ion battery anodes', *Materials*, 6(3), pp. 1138–1158. Available at: https://doi.org/10.3390/ma6031138.

Yang, S., Huo, J., Song, H. and Chen, X. (2008) 'A comparative study of electrochemical properties of two kinds of carbon nanotubes as anode materials for lithium ion batteries', *Electrochimica Acta*, 53(5), pp. 2238–2244. Available at: https://doi.org/10.1016/j.electacta.2007.09.040.

Zhang, W., Mu, B. and Wang, A. (2015) 'Halloysite nanotubes template-induced fabrication of carbon/manganese dioxide hybrid nanotubes for supercapacitors', *Ionics*, 21(8), pp. 2329–2336. Available at: https://doi.org/10.1007/s11581-015-1412-4.

Zheng, H., Yang, R., Liu, G., Song, X. and Battaglia, V.S. (2012) 'Cooperation between active material, polymeric binder and conductive carbon additive in lithium ion battery cathode', *Journal of Physical Chemistry C*, 116(7), pp. 4875–4882. Available at: https://doi.org/10.1021/jp208428w.

7. APPENDIX

7.1. Characterisation of purchased CNTs

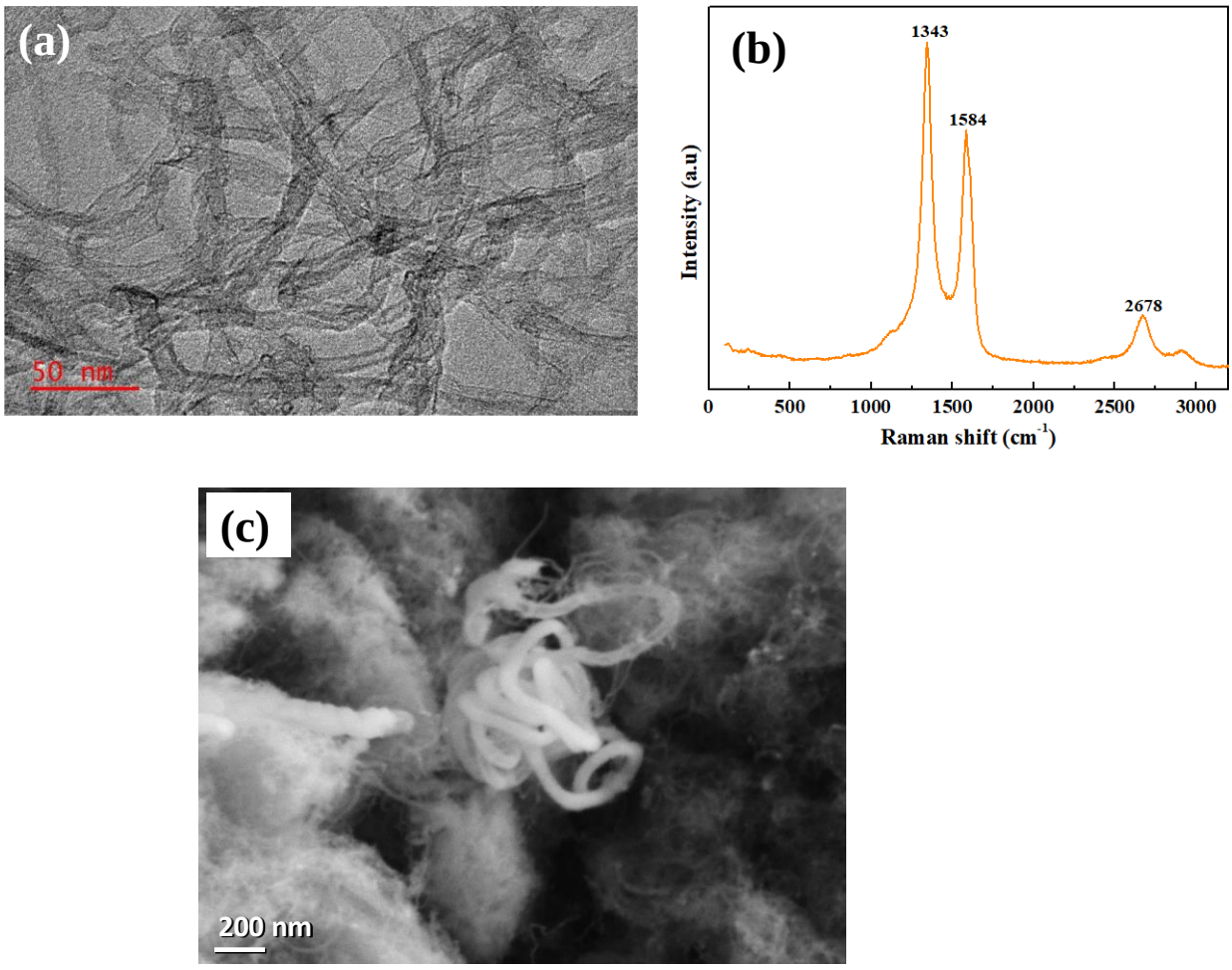

Figure 60: (a) HRTEM image, (b) Raman spectrum and (c) FESEM image of purchased CNTs

7.2. Characterisation of SWCNTs prepared in this study

7.2.1. HRTEM Study

The effect of methane flowrate (100 mL/min) at various synthesis temperatures

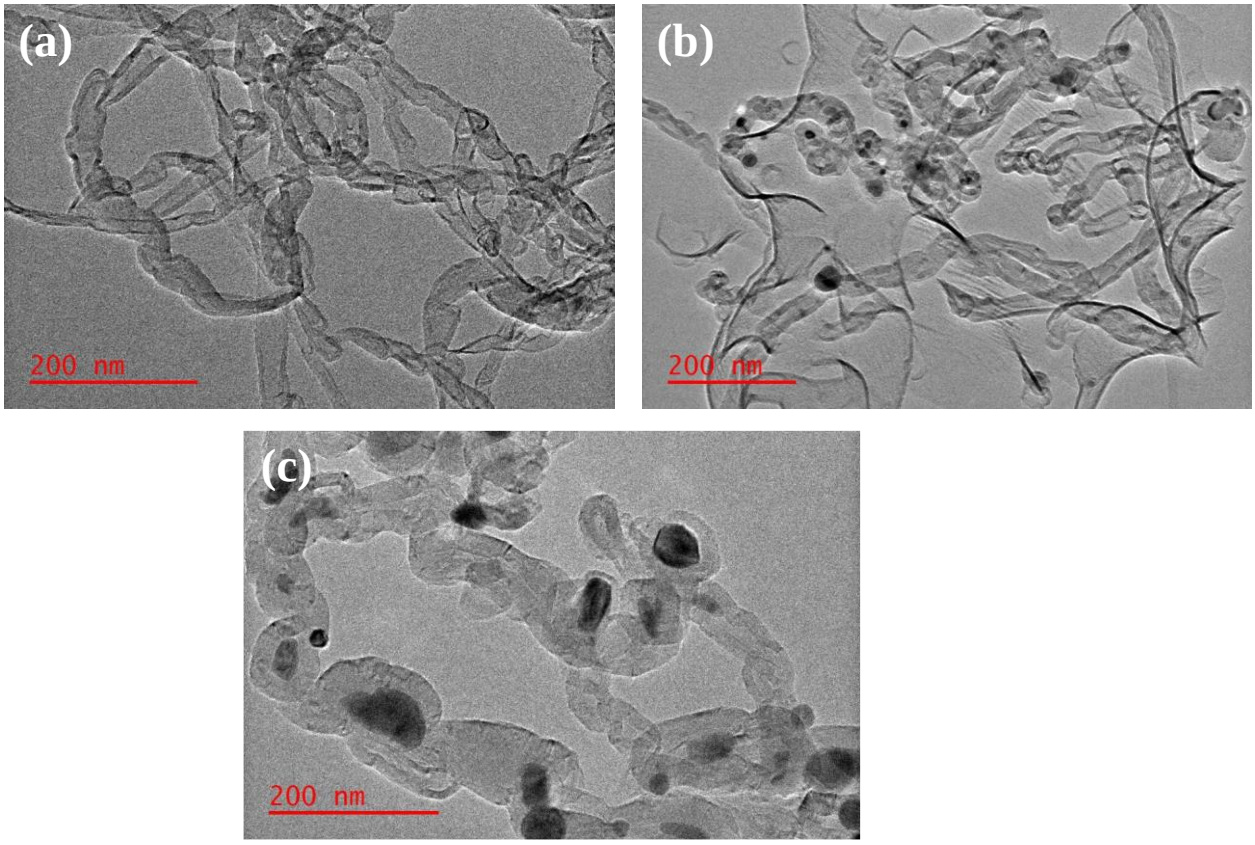

Figure 61: HRTEM images of (a) 700°C-M100, (b) 800°C-M100, and (c) 900°C-M100

The effect of methane flowrate (150 mL/min) at various synthesis temperatures

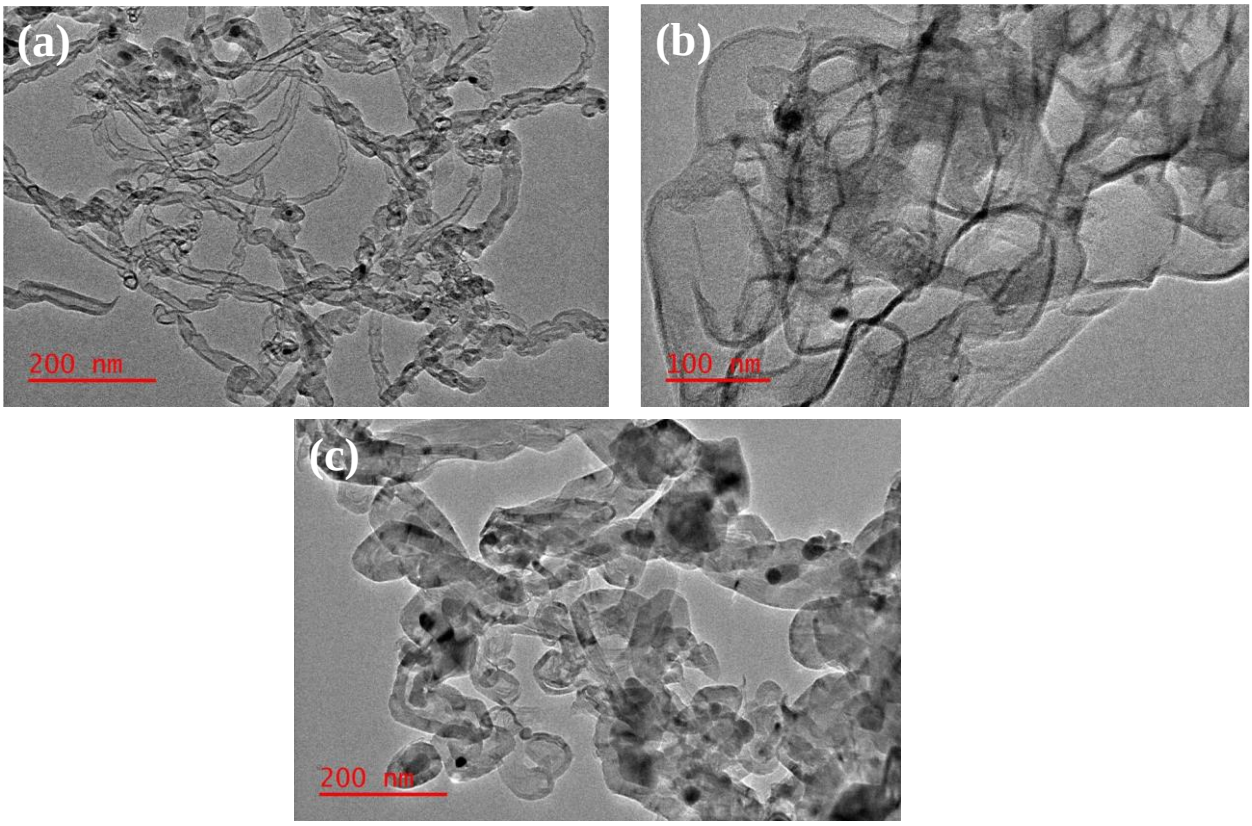

Figure 62: HRTEM images of (a) 700°C-M150, (b) 800°C-M150, and (c) 900°C-M150

7.2.2. Raman Spectroscopy

The effect of methane flowrate (100 mL/min) at various synthesis temperatures

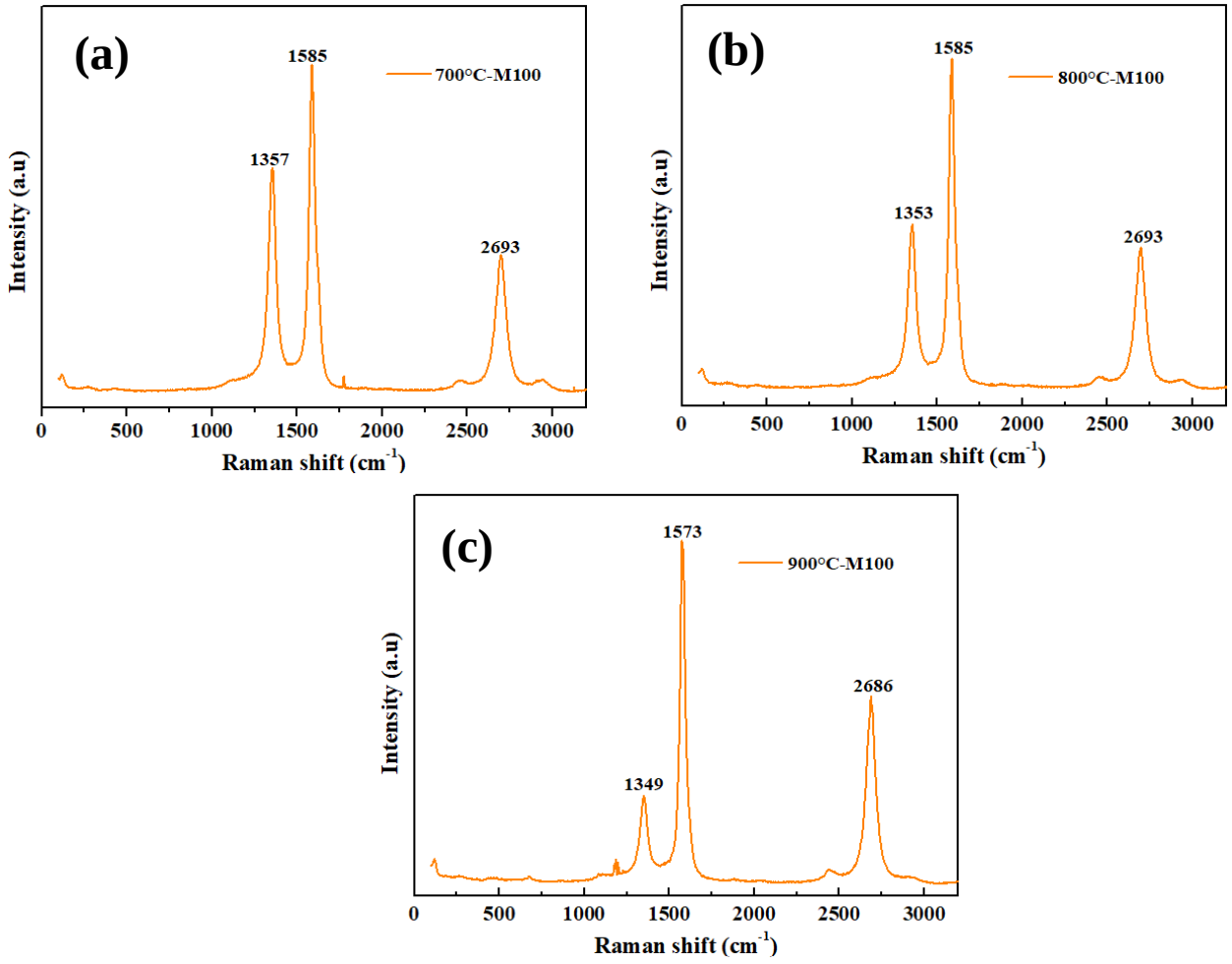

Figure 63: Raman spectra of (a) 700°C-M100, (b) 800°C-M100, and (c) 900°C-M100

The effect of methane flowrate (150 mL/min) at various synthesis temperatures

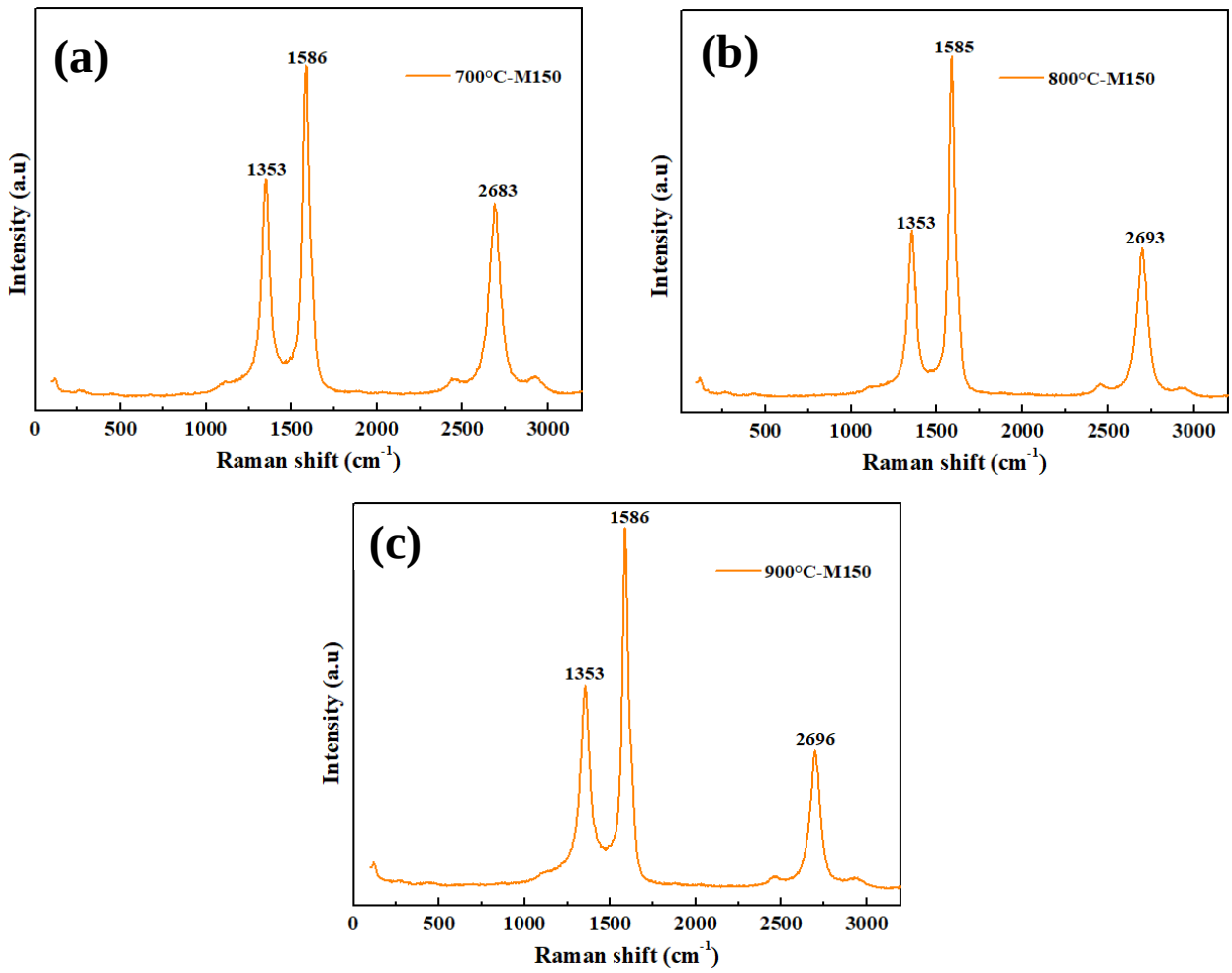

Figure 64: Raman spectra of (a) 700°C-M150, (b) 800°C-M150, and (c) 900°C-M150